

NATIONAL & INTERNATIONAL SCIENTIFIC EVENTS

14th International Conference on Molecular Epidemiology and Evolutionary Genetics of Infectious Diseases

Venue: Hotel Melia
Location: Sitges, Spain

Begins: Nov 6, 2018
Ends: Nov 9, 2018

International Conference on Hydraulics and Pneumatics
HERVEX – 24th edition

Venue: Hotel Palace, Baile Govora
Location: Valcea County, Romania

Begins: Nov 7, 2018
Ends: Nov 9, 2018

The 23rd Asian Technology Conference in Mathematics

Venue: Yogyakarta State University (YSU)
Location: Yogyakarta State University, Indonesia

Begins: Nov 20, 2018
Ends: Nov 24, 2018

International Conference on Drug Discovery and Translational Medicine 2018 (ICDDTM '18)

Venue: THE EVERLY HOTEL
Location: Putrajaya, Malaysia

Begins: Dec 3, 2018
Ends: Dec 5, 2018

21st International Conference on Discrete Geometry for Computer Imagery

Venue: ESIEE Paris, Université Paris-Est
Location: Paris, France

Begins: March 25, 2019
Ends: March 29, 2019

6th International Conference on Food Digestion (Granada 2019)

Venue: Granada Exhibition & Conference Centre
Location: Granada, Spain

Begins: April 2, 2019
Ends: April 4, 2019

4th International Congress on 3D Printing (Additive Manufacturing) Technologies and Digital Industry 2019

Venue: Porto Bello Hotel Resort & Spa
Location: Antalya, Turkey

Begins: April 11, 2019
Ends: April 14, 2019

8th International Conference on Nanotechnology & Materials Science

Venue: Hotel Casa Amsterdam
Location: Amsterdam, The Netherlands

Begins: April 24, 2019
Ends: April 26, 2019

17th International Conference on Chemistry and the Environment

Venue: Aristotle University KEDEA Building
Location: Aristotle University KEDEA Building, Thessaloniki, Greece

Begins: June 18, 2019
Ends: June 20, 2019

22nd International Conference on General Relativity and Gravitation

Venue: Valencia Conference Centre
Location: Valencia, Spain

Begins: July 7, 2019
Ends: July 12, 2019

10th International Conference on Nanotechnology: Fundamentals and Applications (ICNFA'19)

Venue: Will be announced.
Location: Lisbon, Portugal

Begins: August 18, 2019
Ends: August 20, 2019

6th Drug Discovery & Therapy World Congress 2019

Venue: Sheraton Boston Hotel, Boston, MA
Location: Boston, USA

Begins: September 3, 2019
Ends: September 5 2019

HITTITE

JOURNAL OF SCIENCE & ENGINEERING



Abstracted & Indexed in:

TR Dizin Mühendislik ve Temel Bilimler Veri Tabanı | CrossRef | Google Scholar | MIP Database | StuartxChange | ResearchBib | Scientific Indexing Services (SIS)

HITTITE

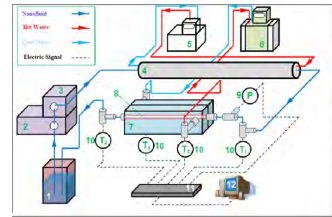
Special Issue 2018: "Selected Papers from the 21st National Thermal Sciences and Technology Congress"

www.hjse.hitit.edu.tr

Numerical and Experimental Investigation of the Effect on Heat Transfer of Nanofluid Usage in Mini/Micro Channels **01-07**

Beytullah Erdoğan, Adnan Topuz, Tahsin Engin, Ali Baş, and Alper Yeter

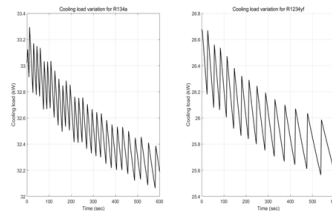
In this study, the thermal performance of Al₂O₃, TiO₂ and ZnO nanofluid in horizontal microchannels was investigated experimentally and numerically. Al₂O₃ (13nm), TiO₂ (10-25nm) and ZnO (18nm) nanoparticles in water to prepare nano-powders with 0.5%, 0.7% and 1.0% volumetric concentration.



Dynamic Performance Comparison of R134a and R1234yf Refrigerants for a Vapor Compression Refrigeration Cycle **9-14**

Mert Sinan Turgut and Mustafa Turhan Çoban

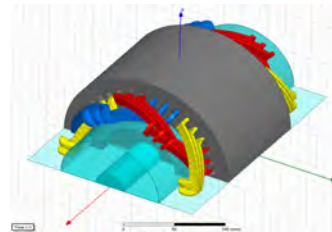
In this study, thermodynamic modelling and dynamic simulation of a vapor compression refrigeration cycle is handled. R134a and R1234yf are used as the primary fluid and water is used as the secondary fluid in the refrigeration cycle.



Design Manufacture and Performance Test of A Reciprocating Refrigeration Compressor **15-24**

Yusuf Ali Kara, Deniz Uzunsoy, Hüseyin Lekesiz, and Mustafa Gürkan Aydeniz

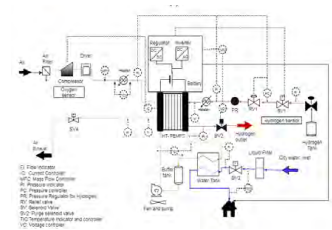
The performance and the manufacturing processes of semi-hermetic refrigeration compressor that was designed and manufactured with a hundred percent of domestic opportunities were investigated in this present study.



Investigation of Working Temperature Effect on Micro-Cogeneration Application of Proton Exchange Membrane Fuel Cells **25-32**

Yağmur Budak, Ekin Özgirgin Yapıcı, and Yülser Devrim

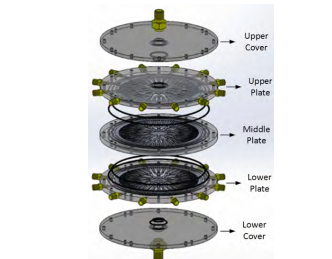
In this study, micro-cogeneration application was used to increase the efficiency of Proton Exchange Membrane Fuel Cell (PEMFC) systems and effect of different operation temperatures on system performance was observed.



Tree Shaped in Channels Parallel and Counter Flow Through Heat Exchanger Heat Transfer and Flow Investigation of Characteristic **33-49**

A. Bugra Colak, Isak Kotcioglu, and Mansour Nasiri Khalaji

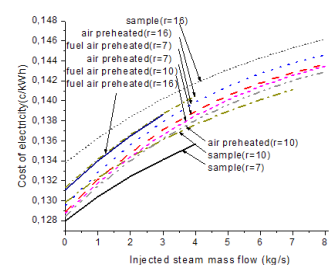
In this study, a heat exchanger system capable of working on tree-shaped three-level parallel and counter flow basis was designed and manufactured based on the branched Fractal like flow channel structure.



Analysis of Steam Injection into Combustion Chamber of Gas Turbine Cogeneration Cycles **51-58**

Rabi Karaali and İlhan Tekin Öztürk

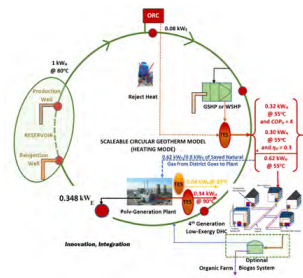
In this study, the analysis of steam injection into cogeneration systems according to performance and evaluation criteria was done using energy, exergy and economic methods.



Rational Exergy Management Model for Effective Utilization of Low-Enthalpy Geothermal Energy Resources 59-73

Biröl Kılkaş and Şiir Kılkaş

This study developed an analysis model, which reveals with case studies and examples that a broad hybridization of combining ORC technology, heat pumps, absorption units, thermal storage, and other renewable energy resources, like solar and wind provides sustainable and exergetically rational design solutions.



Owner

Prof. Dr. Reha Metin ALKAN
on behalf of Hitit University

Editor-in-chief

Prof. Dr. Ali Kılıçarslan

Associate Editors

Assoc. Prof. Dr. D. Ali Köse
Assist. Prof. Dr. Öncü Akyıldız

Production

Dr. Hülya Çakmak
Dr. Kazım Köse
Mustafa Reşit Haboğlu
Erhan Çetin
Harun Emre Kıran
Ömer Faruk Tozlu

Proofreading

Dr. Hülya Çakmak

Editor's Office

Tel: +90 364 227 45 33 / 12 36

Fax: +90 364 227 45 35

Email: alikilicarslan@hitit.edu.tr

Subscription Service:

Tel: +90 364 227 45 33 / 12 82

Fax: +90 364 227 45 35

Email: hjse@hitit.edu.tr

EDITORIAL BOARD

Prof. Dr. İftikhar AHMAD

Prof. Dr. Mike BECKETT

Prof. Dr. İbrahim DİNÇER

Prof. Dr. Ali ELKAMEL

Prof. Dr. Mohamad S QATU

Prof. Dr. Saffa RIFFAT

Prof. Dr. Thanos SALIFOGLU

Assoc. Prof. Dr. Yuehong SU

Dr. Wojciech NOGALA

Prof. Dr. Yusuf AYVAZ

Prof. Dr. Adil DENİZLİ

Prof. Dr. Ali GENÇER

Prof. Dr. Metin GÜRÜ

Prof. Dr. Murat HOŞÖZ

Prof. Dr. Sadık KAKAÇ

Prof. Dr. Tarık Ömer OĞURTANI

Prof. Dr. Ender SUVACI

Assoc. Prof. Dr. Ali TOPÇU

Prof. Dr. Satılmış BASAN

Prof. Dr. Vedat DENİZ

Prof. Dr. Ali KILIÇARSLAN

Prof. Dr. Aydın ÖZLÜK

Prof. Dr. Menderes SUIÇMEZ

Prof. Dr. Seçil SATIR

Prof. Dr. Faruk GÖKMEŞE

Prof. Dr. Uğur Adnan SEVİL

Prof. Dr. İbrahim SÖNMEZ

Assoc. Prof. Dr. Abdurrahman ASAN

Assoc. Prof. Dr. Kazım Savaş BAHÇECİ

Assoc. Prof. Dr. Elif DALYAN

Assoc. Prof. Dr. Naki ÇOLAK

Assoc. Prof. Dr. Hakan GÜNGÜNEŞ

Assoc. Prof. Dr. Bülent KABAK

Assoc. Prof. Dr. Dursun Ali KÖSE

Assoc. Prof. Dr. İrfan KURTBAŞ

Assoc. Prof. Dr. Fatma Muazzez ŞİMŞİR

Assoc. Prof. Dr. Dilber Esra YILDIZ

University of Malakand, Chakdara, Pakistan

Bangor University, Bangor, United Kingdom

Uoit Ontario University, Ontario, Canada

University of Waterloo, Ontario, Canada

Central Michigan University, Michigan, United States

The University of Nottingham, United Kingdom

Aristotle University of Thessaloniki, Thessaloniki, Greece

The University of Nottingham, United Kingdom

Polish Academy of Sciences, Poland

Suleyman Demirel University, Turkey

Hacettepe University, Turkey

Ankara University, Turkey

Gazi University, Turkey

Kocaeli University, Turkey

TOBB University, Turkey

Middle East Technical University, Turkey

Anadolu University, Turkey

Hacettepe University, Turkey

Hitit University, Turkey

Hitit University, Turkey

Hitit University, Turkey

Hitit University, Turkey

Hitit University, Turkey

Hitit University, Turkey

Hitit University, Turkey

Hitit University, Turkey

Hitit University, Turkey

Hitit University, Turkey

Hitit University, Turkey

Hitit University, Turkey

Hitit University, Turkey

Hitit University, Turkey

Hitit University, Turkey

Hitit University, Turkey

Hitit University, Turkey

Hitit University, Turkey

Hitit University, Turkey

Journal Name	: HITTITE JOURNAL OF SCIENCE AND ENGINEERING
Year	: 2018
Managing Editor	: Prof. Dr. Ali KILIÇARSLAN
Managing Office	: Hitit University Faculty of Engineering
Managing Office Tel	: +90 364 227 45 33 / 12 36
Publication Language	: English
Publication Type	: Peer Reviewed, Open Access, International Journal
Delivery Format Print	: 4 times a year (quarterly)
ISSN Publisher Publisher	: 2149-2123
Address	: Hitit Üniversitesi Kuzey Kampüsü Çevre Yolu Bulvarı 19030 Çorum / TÜRKİYE
Publisher Tel	: +90 364 227 45 33 / 12 36



The 2nd National Conference on Thermal Science and Technology, which was organized between 13-16 September 2017 in cooperation with the Turkish Thermal Science Technique Association and the Hitit University, was completed successfully. Within the scope of the 2nd National Heat Science and Technology Congress, where academicians engaged in scientific research in universities in our country, engineers and industrialists working in industry come together.

Scientific discussions under the areas of thermal science such as Thermodynamics, Heat and Mass Transfer, Fluid Mechanics,

Heat Technique, Energy Systems, Energy Economics and Management, Fuels and Combustion, Renewable Energy Systems, Environment, Pollution and Control, New and Clean Energy Technologies were performed. At the 21st National Heat Science and Technology Congress, 53 national and 4 international universities contributed, 171 oral and 13 poster presentations were presented in 26 sessions. In addition, it was observed that both the panelists and the listeners were heavily involved in industrial and public institutions. Within the program, a panel on Heat and Fluid Applications in Industry moderated by Assoc. Dr. Prof. Dr. Barbaros Çetin took place. In the panel the engineers working in the R & D departments of ASELSAN, ROKETSAN, TAI and FORD OTOSAN took part as panelists. Another panel organized by İZODER and moderated by Prof. Dr. Dr. Prof. Dr. Atilla Bıyıkoğlu was on The Role of Thermal Insulation in Energy Efficiency. In the panel Dr. Hasan Haperkan, Kürşat Sakarya and Erdil Dinçer took part as panelists.

As an invited speaker Dr. Sadık Kakaç (TOBB University of Economics and Technology-Department of Mechanical Engineering) gave a seminar on 'Improving Convection Heat Transfer in Channels by Nanofluidics', Prof. Dr. Leonard L. Vasiliev gave a seminar on 'Innovative Heat Pipes and Thermosyphons for Renewable Sources of Energy Applications', Prof. Dr. Bakhtier Farouk (Drexel University-Mechanical Engineering Department, Philadelphia-USA) gave a seminar on 'Acoustically and Thermo-acoustically Driven Transports and Supercritical Fluids: New Advances and Challenges', Dr. Boris V. Kosoy (Institute of Refrigeration, Cryotechnology and Ecoenergetics, Odessa National Academy of Food Technologies, URAIN) gave a seminar on 'Renewable Energy Roadmaps in the XXI Century', Prof. Dr. Ali Koşar (Sabancı University Faculty of Engineering and Natural Sciences Mechatronics Engineering Department) gave a seminar on 'Small-scale Boiling Heat Transfer and Applications' and Assoc. Prof. Dr. Selin Aladağ (TOBB University of Economics and Technology-Department of Mechanical Engineering) gave a seminar on 'Plate Heat Exchangers'.

In the scope of the 21st National Thermal Science and Technique Congress, Çorum Museum, Amasya-Sabuncuoğlu Medical Museum, Boğazkale (Hattuşa) Museum, Hitit University Scientific Technical Application and Research Center (HÜBTUAM) and the Trigenation System located on the campus of the Vocational School were visited.

I would like to thank to Çorum Governor Necmeddin Kılıç, Çorum Mayor Muzaffer Külcü, Rector Prof. Dr. Reha Metin Alkan, Çorum Chamber of Commerce and Industry President Çetin Başaranhıncal, Prof. Dr. Prof. Dr. Sadık Kakaç, Prof. Yalçın Göğüş, Prof. Dr. Haşmet Türkoğlu, Assoc. Prof. Dr. Barbaros Çetin, İsmail Alapala, Mustafa Yağlı, Bülent Onur, Mehmet Çağıl, Mahmut Köksal, Orhan Cazgır, İZODER, Çorum Museum Directorate, Amasya Municipality-Cultural Affairs Directorate and the Science Committee Members and Session Presidents for their contributions. I would also like to thank to the Associate Editor of HJSE Dr. Oncu Akyıldız, as well as our Production Editors Dr. Hülya Çakmak, Mustafa Reşit Haboğlu, Erhan Çetin, Harun Emre Kıran and Ömer Faruk Tozlu for their invaluable efforts in making of this special issue.

Dr. Ali Kiliçarslan
Editor-in-Chief

Numerical and Experimental Investigation of the Effect on Heat Transfer of Nanofluid Usage in Mini/Micro Channels

Beytullah ERDOĞAN¹  Adnan TOPUZ¹  Tahsin ENGİN², Ali BAŞ¹  Alper YETER³

¹Bülent Ecevit University, Department of Mechanical Engineering, Zonguldak, TURKEY

²Sakarya University, Department of Mechanical Engineering, Sakarya, TURKEY

³Kale Oto Radyatör Sanayi ve Ticaret A.Ş., Kocaeli, TURKEY

ABSTRACT

In this study, the thermal performance of Al_2O_3 , TiO_2 and ZnO nanofluid in horizontal microchannels was investigated experimentally and numerically. Al_2O_3 (13nm), TiO_2 (10-25nm) and ZnO (18nm) nanoparticles in water to prepare nano-powders with 0.5%, 0.7% and 1.0% volumetric concentration. A set of experiments was set up for experimentation. For this purpose, micro-channels of 20 cm in length were used at different surface temperatures (15, 25, 40 ° C) from different materials (400, 750, 1000 μ m). In addition, nanofluids with different inlet temperatures, volumetric flow rates (20, 35, 50 mL/min) and concentration ratios are used using nanofluids. Temperature, flow and pressure measurements are based on heat transfer, heat transfer coefficient, Nusselt number, pressure drop and friction factor. The values required for the calculations are measured separately. The effects of parameters such as microchannel diameter, particle type, flow velocity and volumetric ratio on the friction factor, temperature distribution, pressure drop, Reynolds and Nusselt numbers with Taguchi method will be determined in the flow program and compared with the experimental study. In addition, this study will be a preliminary model for the design and analysis of new generation cooling radiators with nanofluid which are not used in diesel engines conforming to Euro 5/6 emissions norms.

Keywords:

Microchannel; Nanochannel; Reynolds Number; Nusselt Number; Numerical Analysis

INTRODUCTION

Nowadays, the cooling systems are used in various areas such as energy transfer, computer systems, electronic systems and heating. Cooling systems provide much more efficient results with recent technology. For decades, many studies include nanofluids that used as refrigerant for cooling systems.

The nanoparticle is a solution formed by the suspension of the nanoparticles in the liquid homogeneously and allowing the transport of the particles through the base liquid. Generally, metal particles and oxides are suspended and transported in pure water or ethylene glycol. We anticipated the heat transfer will be increase by the thermodynamic properties of nanoparticles.

In recent years there have been many studies on the use of nanofluids in cooling systems. Some of those;

Bhattacharya et al. [10], using Al_2O_3 -Water nano-fluid, studied numerically the heat transfer characteristics of laminar forced convection of the nano-fluid in their works. Chen et al. [9] quantitatively analyzed the heat transfer characteristics of a nanoparticle with different nanoparticle volume cross-sections. Lelea [13] determined the heat transfer performance numerically, taking into account the effect of viscous dispersion in the laminar flow regime. Heyhat [4] examined how the heat transfer coefficient and the friction factor change in a horizontal circular tube experimentally. Şahin et al. [2] examined the effects of volumetric concentration and Reynolds number on heat transfer and pressure drop performance experimentally. Karimzadehkhoei et al. [3] also studied TiO_2 -Water nanofluids, differently from Al_2O_3 -Water nanofluids. They have examined the pressure drop and heat transfer properties of neuroplates

Article History:

Received: 2018/01/19

Accepted: 2018/02/27

Online: 2018/09/07

Correspondence to: Beytullah Erdoğan,
Bülent Ecevit University, Department
of Mechanical Engineering, Zonguldak,
TURKEY

E-Mail: beytullaherdogan@hotmail.com

Tel: +90 372 291 1633

in horizontal smooth microtubes for thermally developing flows under constant heat flow conditions with using nanofluids. Ahmet et al. [11] who used the Cu-pure water in their studied examined the heat transfer gain and pressure drop characteristics of nanoparticles flowing through the isothermally heated curved canal path using numerical methods in their studies. Tsai-Chein et al. [12] also studied Carbon Nanotube-Water nano-fuel, which is different from Cu-Su nano-fuel. They examined the performance of the microchannel cooler using these two nanofluids. Azmi et al. [5], used TiO_2 -Water nanofluid in their experiments, and examined the heat transfer coefficient and friction factor in turbulent flow at different volumetric concentrations, constant heat flow condition. Azmi et al. [5] experimentally investigated the heat transfer coefficient and friction factor of a copper circular tube using a SiO_2 -water nanofluid in addition to the TiO_2 -Water nanofluid in a different study. Bhanvase et al. [6] investigated the effects of the nano-flow rate and inlet temperature on the heat transfer performance in the case of constant heat flow experimentally. Haghigi et al. [7] examined the cooling performance of a small-diameter tube using Al_2O_3 -Water and CeO_2 -Water nanofluids, unlike TiO_2 -Water nanofluids. Ho et al. [8] examined the results in different microchannels obtained for the maximum wall temperature, thermal resistance, mean heat transfer coefficient, pump power and friction factor with varying Reynolds in their work. Mohammed et al. [3] have applied three-dimensional simulations for varying Reynolds numbers at a constant volume for a triangular-shaped microchannel, a constant volume flow at the top plate, and evaluated the results.

In this study, the heat conductive coefficient, heating performance and Nusselt numbers of water based nanofluids that have different temperatures(50–60°C) flowing on three different flow rates in the horizontal circular microchannels that are at various surface temperatures (10, 25, 40°C), materials (400, 750, 1000µm) and diameters are

Table 1. Properties of nanoparticles.

Nano Particle	Avarage Diameters (nm)	Density (kg/m ³)	Specific Heat (J/kg.K)	Thermal Conductivity Coefficient (W/m.K)
Al_2O_3	13	3890	778	46
TiO_2	25	3900	710	10
ZnO	18	5606	500	54

examined by using Taguchi method experimentally. This study examined many different parameters in the same experimental setup and obtained the results that shown on the graphics unlike other studies in the literature. These results that obtained is modeling numerically(CFD) and compare with experimental results.

MATERIAL AND METHODS

Properties of Nanoparticles

In this study, Al_2O_3 , TiO_2 and ZnO, used as nanoparticles and incorporated in to water as the base fluid were. Table 1 shows the nanoparticle properties.

Preparation of Nanofluids

The nanofluids were prepared using an ultrasonic homogenizer(Characteristics of the ultrasonic homogenizer: Optics Ivymen System, CY-500, Power: 500W, Frequency: 20kHz, Probe Diameter / Length: Ø5.6 / 60mm). Al_2O_3 , TiO_2 and ZnO nanoparticles were mixed with pure water, and they were set to volumetric concentration of 0.5%, 0.7% and 1%. The mass quantities of the nanoparticles and pure water used in the nanoparticle solution were measured using a precision scale based on the required amounts for volumetric concentration of the nanoparticles. Solubility has been proven by looking at the SEM images provided with homogeneity.

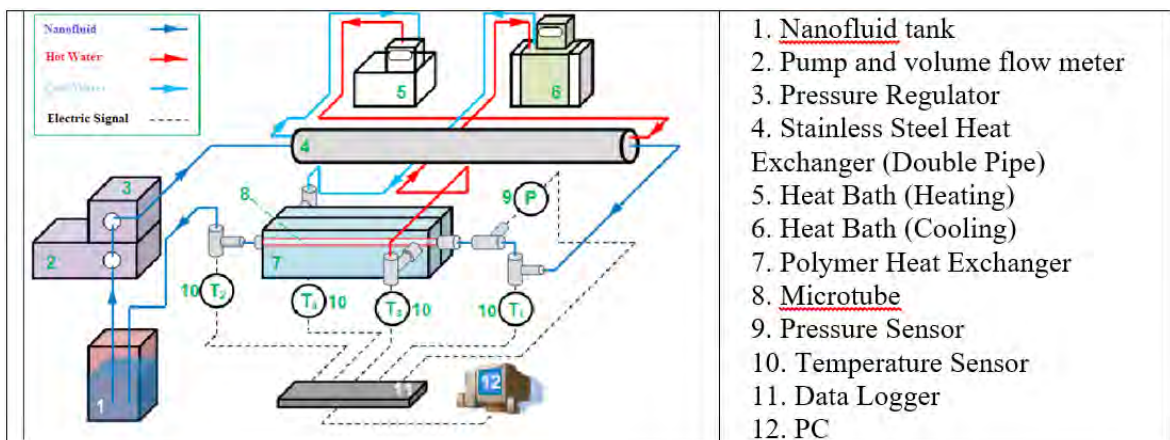


Figure 1. Schematic display of the test set.

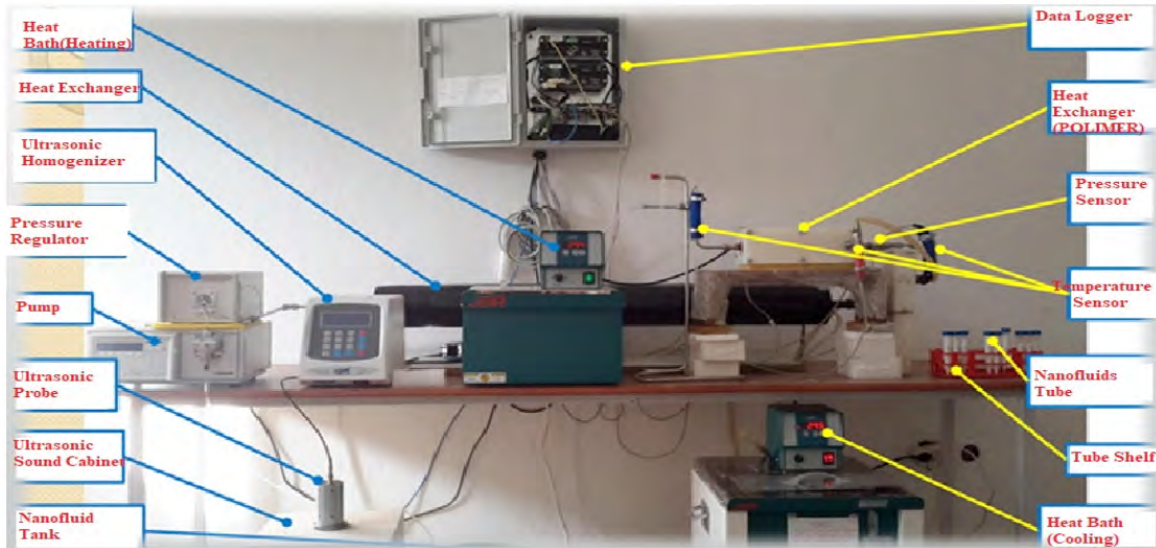


Figure 2. Test set.

Thermophysical Properties of Nanoparticles

The individual thermal conductivity coefficient for each volumetric concentration was measured with Decagon KD2-Pro (KS-1 Probe) and viscosity AND SV-10. The values obtained at the end of these measurements are transformed and plotted into a correlation which can give almost real results in the intermediate values by the curve fitting method. The specific heat and density values of the nanofluids are calculated and used from general equations.

Test Set

Experimental set include; the pump and regulator, heating bath, cooling bath, micropipes that working dimensions, heat exchanger made of polymer materials, insulating materials, heat exchanger made of stainless steel, temperature sensors, pressure sensor, data logger and PC. In Fig. 1 the test set is shown schematically, while in Fig. 2, the actual experiment set is given.

Table 2. Nusselt numbers as a result of verification experiments.

Volumetric Flow (mL/min)	10	15	17	20
T_{in} (°C)	44,8	44,0	44,4	44,8
T_{out} (°C)	16,2	19,2	19,9	21,3
$T_{surface,in}$ (°C)	10,1	10,1	10,1	10,1
$T_{surface,out}$ (°C)	9,9	9,9	10,0	10,0
Pressure Drop (bar)	1,150	1,680	1,900	2,300
Nusselt Number (Sieder-Tate)	3,342	3,809	3,964	4,171
Nusselt Number (Edwards)	4,066	4,244	4,311	4,409
Nusselt Number (Full Developed)	3,66	3,66	3,66	3,66
Nusselt Number (Experimentally)	3,081	3,496	3,785	4,011

Verification Experiments

Verification experiments have been conducted to check that the system is working properly before starting the experiments. In the verification experiments, hydrodynamic and thermally developed laminar flow condition in a circular cross-section with constant surface temperature limit were investigated. Nusselt numbers and heat transfer coefficients were found. The results of the experiments were compared with the Sieder-Tate and Edwards equations, which are valid in the literature with the selected conditions. Micropipes with a diameter of 400µm were used in verification experiments and pure water was used as a fluid. Table 2 and Table 3 show the experimental Nusselt numbers and heat transfer coefficients, respectively.

Table 3. Heat Convection Coefficient as a result of verification experiments.

Volumetric Flow (mL/min)	10	15	17	20
T_{in} (°C)	44,8	44,0	44,4	44,8
T_{out} (°C)	16,2	19,2	19,9	21,3
$T_{surface,in}$ (°C)	10,1	10,1	10,1	10,1
$T_{surface,out}$ (°C)	9,9	9,9	10,0	10,0
Pressure Drop (bar)	1,150	1,680	1,900	2,300
Heat Convection Coefficient (Sieder-Tate) (W/mK)	5404	6177	6436	6786
Heat Convection Coefficient (Edwards) (W/mK)	6574	6881	7000	7175
Heat Convection Coefficient (Full Developed) (W/mK)	5918	5934	5942	5955
Heat Convection Coefficient (Experimentally) (W/mK)	4982	5668	6146	6527

Data Analysis and Important Formulas

The values of Nusselt number, heat transfer coefficient and heat transfer calculations are obtained at the end of this research. The general formula given below of cross-flow heat exchangers was used for calculation heat transfer.

$$Q = \dot{m} * C_p * (T_{out} - T_{in}) \quad (1)$$

$$\dot{m} = \rho * \dot{V} \quad (2)$$

Here \dot{m} is flow rate, C_p is specific heat of nanofluid, T_{in} is the inlet temperature of nanofluid in the microchannel, T_{out} is the outlet temperature of the nanofluid in the microchannel, ρ is density of nanofluid and, \dot{V} indicates the multiplication of nanofluid velocity and surface area at the inlet of microchannel. The general formula of cross-flow heat exchangers is used for calculation of convective heat transfer coefficient as given below.

$$Q = h * A * \Delta T_{ln} \quad (3)$$

$$A = \pi * D * L \quad (4)$$

$$\Delta T_{inlet} = T_{in} - T_{surface,in} \quad (5)$$

$$\Delta T_{out} = T_{out} - T_{surface,out} \quad (6)$$

$$\Delta T_{ln} = (\Delta T_{in} - \Delta T_{out}) / \ln(\Delta T_{in} - \Delta T_{out}) \quad (7)$$

In these formulas, A is inner surface area of microchannel, D is the inner diameter of microchannel, L is length of microchannel, $T_{surface,in}$ is the temperature of the inner microchannel surface, $T_{surface,out}$ is the temperature of the outlet surface of the microchannel, ΔT_{ln} is the logarithmic average temperature belonging to the nanofluids, Q is the amount of heat transfer, h is conductive heat transfer coefficient. The following equations were used while calculating Nusselt number. In this formulas, h_i is conductive heat transfer-coefficient of the inner surface of the pipe, Di is the inner diameters of pipe and k is the thermal conductivity coefficient.

$$Nu = (h * D) / k \quad (8)$$

Sieder-Tate(Re<2300)

$$Nu_{the} = 1,86Gz^{1/3} (\mu_b / \mu_s)^{0,14} \quad (9)$$

Edwards(Re<2300)

$$Nu_{the} = 3,66 + 0,065Gz / (1 + 0,04Gz^{2/3}) \quad (10)$$

Heat Convection Coefficient

$$h_{the} = Nu_{the} k / D_{in} (W / m^2 K) \quad (11)$$

The Principle of the Working System

The piston pump, which draws fluid from the nanofluid tank, was set from the digital indicator. In order to bring the nanofluid to the desired temperature, hot water was supplied through a heat exchanger made of stainless steel material. In the other heat exchanger chamber made of polymer material, in which the micro-tube is located, cold water was simultaneously supplied from the cooling chamber to cool the nanofluid. The pressure regulator, which was connected to the pump, regulates the flow while the pump delivering the nano-fuel from the tank to the system. The nanofluid coming out of the regulator that entering the double tube heat exchanger made of stainless steel material. The nanofluid at the desired temperature that coming out from dual tube heat exchanger enters the micro pipe. The temperature of the nanofluid flowing through the micropipeis reduced with the cold water circulating in the cross flow heat exchanger. is the temperature of it was measured by another temperature sensor located at the outlet of the micro channel. The heat transfer state was examined in terms of the temperature. The nanofluid coming out from the micro-pipe is again poured into the nanofluid tank with the used hoses. This ensures continuity in the system.

Experimental Study

The nano-powders (Al_2O_3 -pure water, TiO_2 -pure water and ZnO -pure water) initially prepared at volumetric concentrations are also poured into the nanofluid tank at the desired amount. This amount is set with a precision scale. The metal pipes in the system are covered with insulating materials against any heat loss. The connection points on the system are connected with fasteners for preventing any leakage. In the heat chamber, the heated water is heated to a stable temperature value at the nanoparticle inlet temperature of the micro-tube. This stable temperature is monitored from the computer through the data logger located in the system. In the same way, if it is desired to circulate a few degrees of cold water in the heat exchanger reservoir surrounding the micro-pipe, the cooling bath is cooled until the stable temperature condition was obtained. This stable temperature value similarly controlled from the computer. By setting the desired flow rate from the flow rate indicator on the pump, nanofluid transfer is started in the system. From this point, the microchannel inlet temperature of the nanofluid and the temperature of the cold water circulating outside the micro tube are expected until the desired value was stabilized. When the required conditions were met, the amount of heat transfer was calculated by the obtained data.

Table 4. Taguchi Experimental Values.

Test	Factors						
	A	B	C	D	E	F	G
	Tube Material	Tube Diameter μm	Fluid Type	Fluid Volume Concentration	Fluid Temperature $^{\circ}\text{C}$	Heat Bath Temperature $^{\circ}\text{C}$	Fluid Flow mL/min
1	SS	381	Al_2O_3	0.5	52.8	11.9	20
2	SS	381	TiO_2	0.7	58.4	24.3	35
3	SS	381	ZnO	1.0	67.0	40.6	50
4	SS	762	Al_2O_3	0.5	56.8	24.2	50
5	SS	762	TiO_2	0.7	72.6	38.9	20
6	SS	762	ZnO	1.0	50.8	9.1	35
7	SS	1026	Al_2O_3	0.7	49.2	38.6	35
8	SS	1026	TiO_2	1.0	58.6	10.4	50
9	SS	1026	ZnO	0.5	73.9	20.0	20
10	PEEK	381	Al_2O_3	1.0	64.6	24.6	35
11	PEEK	381	TiO_2	0.5	47.4	39.9	50
12	PEEK	381	ZnO	0.7	63.8	9.8	20
13	PEEK	762	Al_2O_3	0.7	65.7	10.6	50
14	PEEK	762	TiO_2	1.0	51.6	24.9	20
15	PEEK	762	ZnO	0.5	59.0	40.0	35
16	PEEK	1026	Al_2O_3	1.0	60.4	39.2	20
17	PEEK	1026	TiO_2	0.5	68.0	10.6	35
18	PEEK	1026	ZnO	0.7	47.9	23.7	50

Taguchi Method

The Taguchi method is a very effective method that is used to obtain the best results in long-term and highly variable experiments, which can accommodate many different parameters. Under normal conditions, without using this method, each nanofluid can be used at different concentrations, at different micropipe diameters, different micropipe materials, different flow rates, different temperature values, etc. The excessive number of experiments must be done in order to apply each condition. The Taguchi method suggests the optimum number

of these parameters and instead of doing thousands of experiments for this study, we present the values that will give the best results in the 18 experiments shown in Table 2. This also saves cost and time.

Numerical Modeling

Numerical modeling analysis was performed with ANSYS CFD (computational fluid dynamics) program. The thermophysical properties of experimentally found nano-fluids were introduced to the program of equations belonging to the given data. The experimental data used

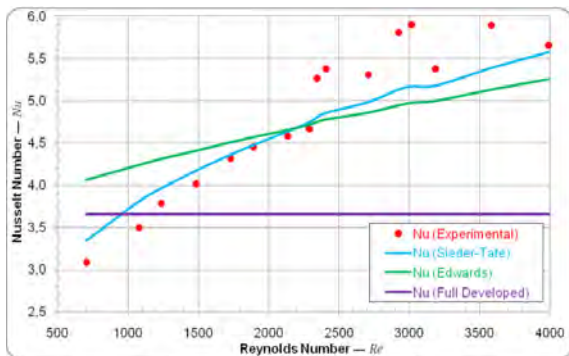


Figure 3. Verification experiments for Nusselt numbers.

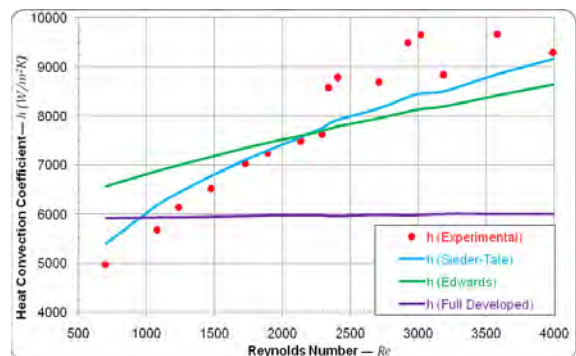


Figure 4. Verification experiments for heat convection coefficient.

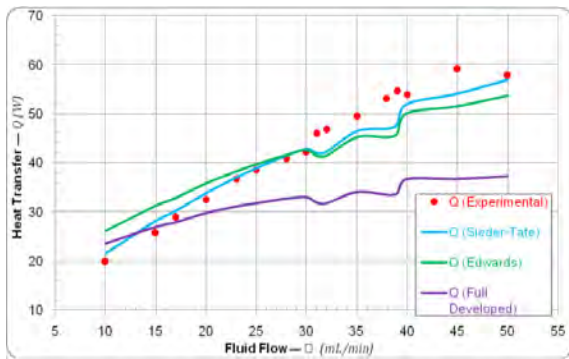


Figure 5. Verification experiments for heat transfer.

in Table 4 are compared with the numerical modeling.

RESULTS AND DISCUSSION

Verification Experiments Results

As shown in Fig. 3 and Fig. 4, Nusselt numbers and heat transfer coefficients are calculated using the Sieder-Tate and Edwards equations, and they were shown on the figure by curve fitting method. Fig. 5 shows the amount

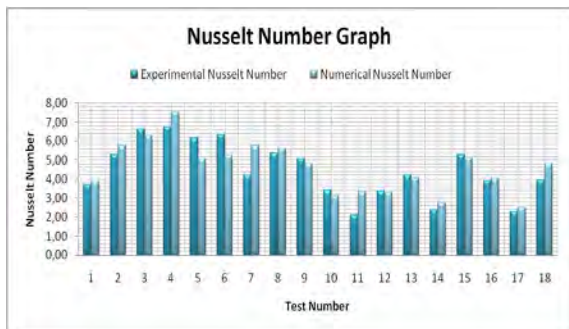


Figure 6. Nusselt number graphic.

of heat transfer obtained by using these results. Experimental Nusselt numbers and heat transfer coefficients obtained from the test results were also transferred by the curve fitting method and compared with the results calculated by formulas. Also in Figure 5, the calculated heat transfer amount from the experimental results was compared with the results found in the formulas. In these

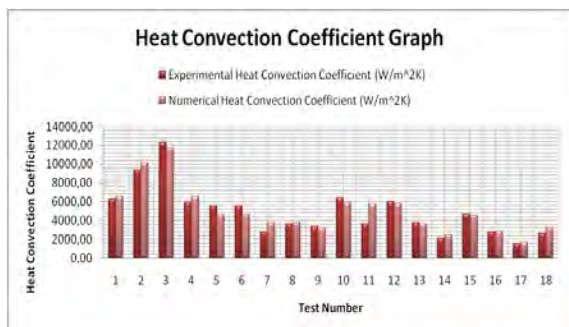


Figure 7. Heat convection coefficient graphic.

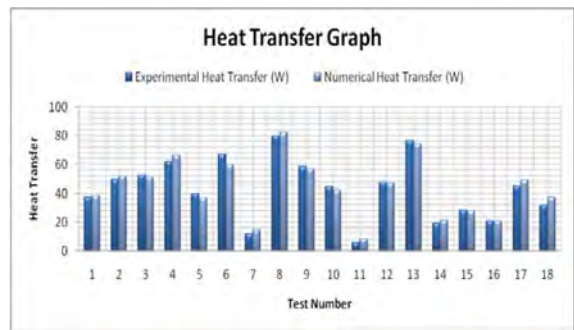


Figure 8. Heat transfer graphic.

graphs the relation between Nusselt numbers and heat transfer coefficients with Reynolds value are shown. The results that using the formulas in the literature obtained were close to the experimental results. Experiments have been carried out in a number of different ways to see the transition regime between the laminar flow and the turbulent flow. Fig. 6, 7, and 8 show the Nusselt numbers,

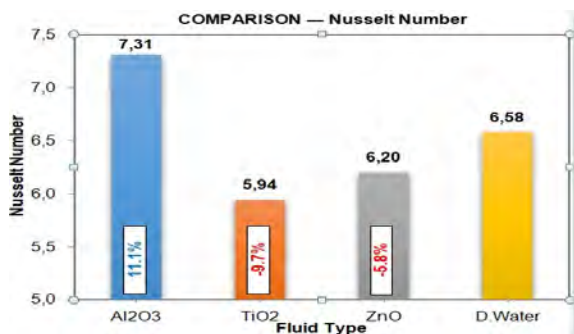


Figure 9. Comparison of Nusselt numbers compared to fluid types.

heat transfer coefficients and heat transfer quantities found in the experiments with the optimum experimental parameters presented by the Taguchi table, and the Nusselt numbers, heat transfer coefficients and heat transfer quantities found in the numerical studies in the same parameters. As can be seen in Fig. 11, the best thermal performance was achieved with the Al₂O₃-water nanofluid. Compared to pure water, 15.3% higher heat transfer was achieved. The second best performer is the nanofluid

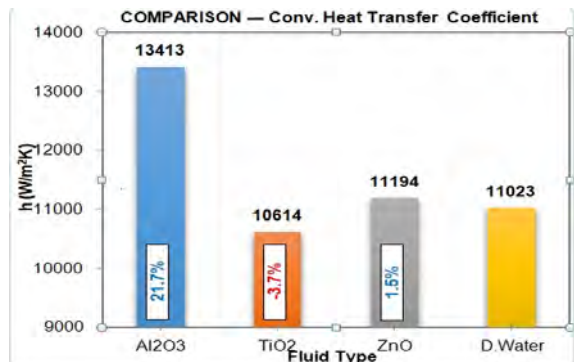


Figure 10. Comparison of heat convection coefficient compared to fluid types.

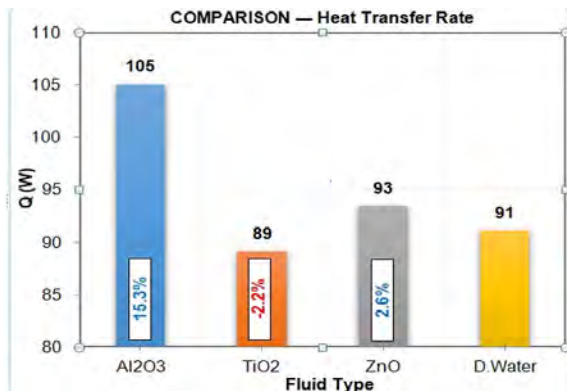


Figure 11. Comparison of heat transfer rate compared to fluid types.

ZnO-water nanofluid. 2.2% less heat transfer than water was obtained with TiO₂.

CONCLUSION

In this study, the Nusselt number, heat transfer coefficients and heat transfer amount of Al₂O₃-water, TiO₂-water and ZnO-water nanofluids flowing in a horizontal circular microchannel under constant surface temperature conditions were calculated experimentally and numerically. Pure water was used as the base liquid. The results can briefly be given as follows:

1) The concentrations and waiting times of the nanoparticles should be well adjusted. If it's not set well, there might be crashes in the nanofluid and sedimentation may occur. Nanoparticles in the melt can cause plugging of the tubes. This can adversely affect both the operation of the system and the thermal performance.

2) The equations given in the literature used in the calculations should be chosen according to the ambient conditions used in the experiments.

3) When the pipe diameter is reduced, the heat transfer rate was increasing.

4) The best thermal performance was obtained with Al₂O₃-water nanofluid.

5) Nanoparticles with the highest thermal conductivity capacity may not provide the best value for heat transfer. The thermal conductivity of the ZnO nanoparticle was higher than that of the other nanoparticles, but the Al₂O₃-water nanofluid had the highest heat transfer value as a result of the experiments.

ACKNOWLEDGEMENT



This project was supported by "The Scientific and Tech-

nological Research Council Of Turkey" (TUBITAK 1505) with Project No. 5140013, the Scientific Research Projects Unit (BAP) with Project No. 201377654622-02 and Kale Oto Radyatör Sanayi ve Ticaret A.Ş. The authors gratefully acknowledge the financial supports from TUBITAK, BAP and Kale Oto Radyatör.

References

- Heyhat MM, Kowsary F, Rashidi AM, Momenpour MH, Amrollahi A. Exp. investigation of laminar convective heat transfer and pressure drop of water-based Al₂O₃ nanofluids in fully developed flow regime. *Exp. Thermal and Fluid Science*, 44 (2013) 483–489.
- Şahin B (2006), Çomaklı K, Çomaklı Ö, Yılmaz M. Nanoakışkanlar ile ısı transferinin iyileştirilmesi (Heat transfer rate improvement with nanofluids). *Mühendis ve Makina*, 47 (2006), 559, 29-34.
- Karimzadehkhoei M, Yalçın SE, Şendur K, Mengüç MP, Koşar A. Pressure drop and heat transfer characteristics of nanofluids in horizontal microtubes under thermally developing flow conditions. *Experimental Thermal and Fluid Science* 67 (2015) 37–47.
- Choi S. Nanofluids for improved efficiency in cooling systems. Argonne National Laboratory, April 18-20 (2006).
- Azmi WH, Sharma KV, Sarma PK, Mamat R, Najafi G. Heat transfer and friction factor of water based TiO₂ and SiO₂ nanofluids under turbulent flow in a tube. *International Communications in Heat and Mass Transfer*, 59 (2014) 30–38.
- Bhanvase BA, Sarode MR, Putterwar LA, Abdullah KA, Deosarkar MP, Sonawane SH. Intensification of convective heat transfer in water/ethylene glycol based nanofluids containing TiO₂ nanoparticles. *Chemical Engineering and Processing*, 82 (2014) 123–131.
- Haghighi EB, Saleemi M, Nikkam N, Anwar Z, Lumberras I, Behi M, Mirmohammadi SA, Poth H, Khodabandeh R, Toprak M, Muhammed M, Palm B. Cooling performance of nanofluids in a small diameter tube. *Exp. Thermal and Fluid Science*, 49 (2013) 114–122.
- Ho CJ, Wei LC, Li ZW. An experimental investigation of forced convective cooling performance of a microchannel heat sink with Al₂O₃/Water nanofluid. *Applied Thermal Engineering*, 30 (2010) 96-103.
- Chen CH, Ding CY. Study on the thermal behavior and cooling performance of a nanofluid-cooled microchannel heat sink. *Int. J. of Thermal Sciences*, 50 (2011) 378-384.
- Bhattacharya P, Samanta AN, Chakraborty S. Numerical study of conjugate heat transfer in rectangular microchannel heat sink with Al₂O₃/H₂O nanofluid. *Heat and Mass Transfer*, 45 (2009) 1323–1333.
- Raisi A, Ghasemi B, Aminossadati SM. A numerical study on the forced convection of laminar nanofluid in a microchannel with both slip and no-slip conditions. *An International Journal of Computation and Methodology*, 59/2 (2011) 114-129.
- Tsai TH, Chein R. Performance analysis of nanofluid-cooled microchannel heat sinks, *Thermal Conductivity of Nanoparticle - Fluid Mixture. Journal of Thermophysics and Heat Transfer*, 13 (2007) 474-480.
- Lelea D. The performance evaluation of Al₂O₃/water nanofluid flow and heat transfer in microchannel heat sink. *International Journal of Heat and Mass Transfer*, 69 (2011) 264-275.

Dynamic Performance Comparison Of R134a and R1234yf Refrigerants for a Vapor Compression Refrigeration Cycle

Mert Sinan Turgut  Mustafa Turhan Çoban 
Ege University, Department of Mechanical Engineering, İzmir, TURKEY

ABSTRACT

Machines like air conditioners and refrigerators, which cause significant energy consumption in countries around the world, are widely used in industry and residences. Analyzing and studying the behavior of these machines with computer simulations can optimize performance of them. In this study, thermodynamic modelling and dynamic simulation of a vapor compression refrigeration cycle is handled. R134a and R1234yf are used as the primary fluid and water is used as the secondary fluid in the refrigeration cycle. R1234yf is a refrigerant, which has low Global Warming Potential (GWP) and Ozone Depletion Potential (ODP) and is recently has been begun to use as a substitute of R134a. In this study, dynamic behaviors of these two refrigerants are examined in a vapor compression refrigerant cycle with fixed operating conditions. Finite Difference Method is utilized for the modelling of the evaporator and condenser and Gunggr-Winterton and Travis et al. correlations are used for the modelling of the evaporation and condensation processes respectively. Orifice equation is utilized for the modelling of the expansion valve and modelling of the compressor is carried out by first dynamically simulating the heat transfer between the gas and surroundings until the gas reaches to compression chamber and after that the polytropic compression process in the chamber. For the realization of the dynamical simulation, refrigerant fluid mass flow rate is applied to the system as step input. Response of the system to the input is observed with transient p-h and coefficient of performance (COP) diagrams. The results showed that COP is started off with the values of 2.079 for R134a and 1.711 for R1234yf, reached the maximum points of 2.577 for R134a and 2.02 for R1234yf, then slowly declined with fluctuations. In the p-h diagram, due to temperature rise of inner walls of the evaporator and condenser, condenser outlet and compressor inlet enthalpy values started off with 395,945 kJ/kg and 231,714 kJ/kg for R134a, 361,557 kJ/kg and 230,750 kJ/kg for R1234yf, then approached to the saturation curve with time and reached the values of 393,957 kJ/kg and 233,808 kJ/kg for R134a, 359,547 kJ/kg and 231,917 kJ/kg for R1234 yf.

Keywords:

Refrigeration cycles; Dynamic Simulation; System Modelling; Thermodynamics; Global Warming Potential

INTRODUCTION

Nowadays, refrigeration machines have various domestic and industrial applications and they play a huge role in energy consumption. By doing research studies, it is desired to make these machines more effective with less energy consumption [1]. Inspecting the dynamical behavior of the refrigeration machines is an important factor in design and control of these machines.

An important factor that affects the performance of the refrigeration machines is refrigerant selection [2]. Nowadays, refrigerants that have lower Global Warming Potential (GWP) and Ozone Depletion Potential (ODP) values are begun to take the place of those that have higher GWP and ODP values. In refrigeration machines, usage of R1234yf as an alternative to R134a, which is a refrigerant that is widely used in refrigeration machines, is gaining momentum due to its lower GWP and ODP values.

Article History:

Received: 2018/01/19

Accepted: 2018/02/27

Online: 2018/09/07

Correspondence to: Mert Sinan Turgut,
Ege University, Department of Mechanical
Engineering
E-mail: sinanturgut@me.com

One of the first studies in dynamical modelling of the refrigeration cycles is conducted by the American National Standards Bureau which investigated the steady-state behavior of the chiller [3] and boiler [4]. Moreover, the first studies that aim to optimize the system design and increase the energy saving have taken their place in the literature [5-7]. Chi and Didion [8] developed a software that can achieve the dynamical analysis of their heat pump called TRPUMP and includes the models of the all components in lumped parametric form and they compared the results that they acquired from the software with the results reported by the American National Standards Bureau. Bonne et al. [9] studied the dynamical simulation of a heat pump with a compressor driven by an electrical motor and its on-off control. MacArthur [1] modelled a vapor compression cycle to accomplish the closed-loop control of the system, achieved the dynamic simulation, investigated the stability and response of the system and then compared these results with the experimental results. Chen and Lin [10] studied the optimal component combination to decrease the energy consumption of a small-scaled refrigeration system. In this study, the authors aimed to find the most favorable design combination of the compressor, the evaporator, the condenser and the capillary tube in order to reduce the energy consumption. Fu et al. [11] achieved the dynamical modelling of a dual-mode air-to-water heat transfer based heat pump. The studies in this field are published over time and still continuing with developing control strategies [12] and dynamical modelling of various system variations [13].

The effect of R1234yf and R1234ze refrigerants, which are recommended as a substitute of the R134a, to the performance of the system are still studied. Yatağanbaba et al. [2] studied the exergetic analysis of two-compressor refrigeration cycle with R1234yf and R1234ze refrigerants and compared the exergetic behavior of these two refrigerants. Mo-ta-Babiloni [14] studied the effects of R134a, R1234yf and R1234ze refrigerants both experimentally and theoretically to the system performance, condenser outlet temperature and evaporator outlet temperature. Belman-Flores et al. [15] experimentally studied the effects of R1234yf and R134a to the performance and evaporator and condenser outlet temperatures of a domestic refrigerator.

In this study, a vapor compression refrigeration cycle is considered. Thermodynamic and dynamical modelling of the system is achieved. R134a and R1234yf refrigerants are considered as the primary fluids and water is considered as the secondary fluid. Evaporator and condenser is modelled with the finite difference method and evaporation and condensation processes is modelled with Gungor and Winterton [16] and Travis et al. [17] correlations respectively. Modelling of the compressor is accomplished with two separate processes. First, until the refrigerant arrives to the compres-

sion room, the heat transfer between the refrigerant and the environment is considered. Then the polytropic compression process equation is utilized after the refrigerant arrives to the compression room. For the expansion valve, orifice equation is utilized [1]. Mass flow rate of the refrigerant is applied to the system as the step input. Afterwards, the dynamic effect of R1234yf and R134a refrigerants to the system's coefficient of performance, required compressor work, cooling load, pressure-enthalpy and temperature-entropy characteristics are investigated.

The rest of the paper is considered as follows. In the second chapter, dynamical modelling of the refrigeration cycle is described. In the third chapter, the results are discussed in detail and the fourth chapter concludes the paper.

MODELLING OF THE SYSTEM

A basic refrigeration cycle consists of four components, namely, the evaporator, the condenser, the compressor and the expansion valve. The refrigerant absorbs the heat from the evaporator and evaporates, then the gas is compressed in the compressor and directly its pressure and indirectly its temperature increases. Afterwards, the excess temperature is emitted in the condenser and the pressure of the refrigerant is decreased to the condenser inlet pressure level in the expansion valve. A diagram of a basic refrigeration cycle is given in Fig. 1.

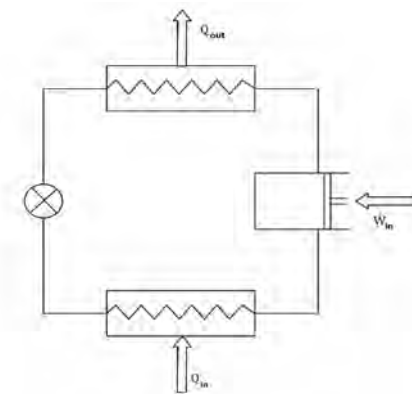


Figure 1. A basic refrigeration cycle

In the following subsections, the dynamical modelling of the each component is given.

Evaporator

The finite difference method is utilized for the modelling of the evaporator. A cross-flow evaporator with one dimensional fluid flow is considered. Gungor and Winterton [16] correlation is utilized for the modelling of the evaporation process. The heat convection coefficient can be calculated with Gungor and Winterton correlation shown in equations through 1-7.

$$Bo = \frac{q}{\rho V h_{fg}} \quad (1)$$

$$X_{tt} = \left(\frac{1-x}{x} \right)^{0.9} \left(\frac{\rho_v}{\rho_l} \right)^{0.5} \left(\frac{\mu_l}{\mu_v} \right)^{0.1} \quad (2)$$

$$E = 1 + 24000 Bo^{1.16} + 1.37 (1/X_{tt})^{0.86} \quad (3)$$

$$S = \frac{1}{1 + 1.15 \times 10^{-6} E^2 Re^{1.17}} \quad (4)$$

$$h_l = 0.023 Re^{0.8} Pr^{0.4} k / d \quad (5)$$

$$h_{pool} = 55 Pr_r^{0.12} (\log_{10} Pr_r)^{-0.55} M^{-0.5} q^{0.67} \quad (6)$$

$$h_{tp} = Eh_l + Sh_{pool} \quad (7)$$

where Bo represents the boiling number, q shows the heat transfer rate, X_{tt} shows the Martinelli coefficient, x represents the quality of the vapor, k shows the heat conduction coefficient, M shows the molar mass and v and l subscripts represents the gas and liquid phases, respectively. Gnielinski [18] correlation is utilized for the single phase turbulent flows. Nusselt number can be calculated with the use of Gnielinski correlation as in Eq. 8.

$$Nu = \frac{(f/2)(Re-1000)Pr}{1 + 12.7 \sqrt{f/2} + Pr^{2/3}} \quad (8)$$

where Nu represents the Nusselt number, Pr shows the Prandtl number, Re shows the Reynolds number and f represents the friction factor. The friction factor and the Reynolds number can be calculated by using Eq. 9-11.

$$Re = \frac{\rho V D}{\mu} \quad (9)$$

$$f = \frac{64}{Re} \quad \text{Laminar} \quad (10)$$

$$f = (0.79 \ln Re - 1.64)^{-2} \quad \text{Turbulence}$$

where ρ shows the fluid density, V represents the fluid velocity, D shows the pipe diameter and μ represents the fluid viscosity. The equations for the calculation of the behavior of the primary fluid are given in Eq. 11-12.

$$\frac{\partial \dot{m}_g h_g}{\partial t} = \dot{m}_c h_{fg} - \frac{\partial \dot{m}_g h_g}{\partial x} dx \quad (11)$$

$$\frac{\partial \dot{m}_f h_f}{\partial t} = h_i p_i dx (T_{hx} - T_r) - \frac{\partial \dot{m}_f h_f}{\partial x} dx - \dot{m}_c h_{fg} \quad (12)$$

where \dot{m}_f , \dot{m}_g ve \dot{m}_c shows the mass flow rate of the liquid, gas and liquid-gas phases, respectively, h_f , h_g ve h_{fg} represents the enthalpy of the liquid, gas and liquid-gas phases, respectively, h_i represents the convection coefficient of the fluid, p_i shows the inner tube diameter and T_{hx} and T_r represents the wall and primary fluid temperatures, respectively. The behavior of the secondary fluid can be calculated by utilizing the Eq. 13.

$$\rho \frac{\partial h}{\partial t} - \rho Va \frac{\partial h}{\partial x} - \frac{h_o p_o}{A} (T_{hx} - T_f) = 0 \quad (13)$$

where ρ shows the fluid density, Va shows the fluid velocity, h_o shows the convection coefficient, p_o represents the outer tube diameter and T_f represents the secondary fluid temperature. The wall temperature of the evaporator can be calculated as Eq. 14

$$C \rho V \frac{\partial T_{hx}}{\partial t} - h_i p_i (T_r - T_{hx}) + h_o p_o (T_{hx} - T_f) = 0 \quad (14)$$

where C shows the specific heat of the wall and V shows the volume of the wall.

Condenser

Modelling of the condenser follows the same procedure of the evaporator except the condensation process is modelled with the Travis et al. [17] correlation. The wall and the secondary fluid behavior equations of the evaporator are valid for the condenser. Primary fluid behavior of the condenser can be calculated as the following equations.

$$\frac{\partial \dot{m}_f h_f}{\partial t} = \dot{m}_c h_{fg} + \frac{\partial \dot{m}_f h_f}{\partial x} dx \quad (15)$$

$$\frac{\partial \dot{m}_g h_g}{\partial t} = h_o p_o dx (T_r - T_{hx}) + \frac{\partial \dot{m}_g h_g}{\partial x} dx + \dot{m}_c h_{fg} \quad (16)$$

where \dot{m}_c shows the mass flow rate of the condensing fluid.

Compressor

Modelling of the compressor is achieved in two separate processes. First, the heat transfer between the fluid and the environment is considered until the fluid arrives to the compression room. Then, the polytropic compression process equation is utilized after the refrigerant arrives to the compression room. An example demonstration of the compressor is given in Fig. 2.

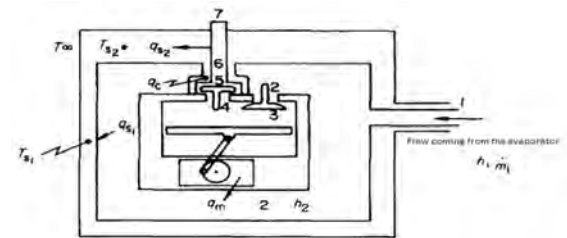


Figure 2. Inner design of the compressor [1]

The heat transfer equations that models the fluid temperature change until the fluid arrives to the compression room are given in Eqs. 17-19.

$$\rho_{\beta} V_{\beta} (T_3 - T_1) = h_{co} (T_{cyl} - T_1) - h_{s1} (T_1 - T_{s1}) \quad (17)$$

$$(C_{cyl} \rho_{cyl} V_{cyl}) \frac{dT_{cyl}}{dt} = h_{ci} (T_5 - T_{cyl}) - h_{co} (T_{cyl} - T_1) \quad (18)$$

$$(C_{sh}\rho_{sh}V_{sh})\frac{dT_{s1}}{dt} = h_{s1}(T_2 - T_{s1}) - h_{s1o}(T_{s1} - T_\infty) \quad (19)$$

where *fl*, *cyl* ve *sh* subscripts shows the primary fluid, the cylinder and the outer shell of the compressor. Meanings of the other symbols and subscripts can be inferred from Fig. 2. The fluid enters the compressor in T_1 temperature, then, it interacts with the environment and heats up to T_3 temperature and compressed in the compression room. Compression process in the compression room can be represented by the following equation.

$$\frac{T_4}{T_3} = \left(\frac{P_{cond}}{P_{evap}}\right)^{\frac{\gamma-1}{\gamma}} \quad (20)$$

where T_4 shows the compressor outlet temperature, P_{cond} and P_{evap} represents the condenser and the evaporator pressures and γ shows the isentropic compression coefficient.

Expansion valve

The modeling of the expansion valve is accomplished by utilizing the orifice equation given in James and James [19]. The fluid enthalpy is assumed to be steady between the entrance and exit of the expansion valve. The orifice equation is given in Eq. 21.

$$\dot{m} = 0.0683x\sqrt{(P_{cond} - P_{evap})} \quad (21)$$

where x shows the openness measure of the valve needle in mms.

RESULTS

Mass flow rate of the primary fluid with 0.2 kg/sec is applied to the system as step input. The input is applied to the system from the entrance of the evaporator and after each cycle completion, a time step is executed. R134a and R1234yf are utilized as the primary fluids and water is utilized as the secondary fluid. Thermodynamic and thermophysical property equations of R134a, R1234yf and water are acquired from Tillner-Roth and Baehr [20], Richter et al. [21] and Wagner and Pruß [22], respectively. Isentropic compression ratios of R134a and R1234yf are considered as 1.2 and 1.1, respectively. Walls of the evaporator and the condenser and shell of the compressor are considered as made of steel. Internal pressure of the evaporator is taken as 200 kPa and openness amount of the expansion valve needle is taken as 1.1 mm. By utilizing the orifice equation, it is calculated that the internal pressure of the condenser is 796.6 kPa. Under these circumstances, R134a boils at approximately -10°C and condenses at 31°C, while R1234yf boils at -13°C and condenses at 30.5°C. Inner and outer tube diameters of the evaporator

and the condenser are considered as 0.01m. and 0.018 m. while their lengths are taken as 14 m. Flow velocity of the both fluids are taken as 0.7 m/sec., under this circumstance, they both flow in turbulence. Initial temperatures of the environment, outer shell of the compressor and the cylinder are taken as 25°C and corresponding convective heat transfer coefficients are selected. In the evaporator, initial temperatures of the primary fluid, the secondary fluid and the wall are considered as -11°C, 0°C and 0°C, while in the condenser, the secondary fluid and the wall initial temperatures are considered as 23°C and 23°C. Finally, time steps are taken as 3 sec. and length steps in the evaporator and the condenser are taken as 0.1 m. Moreover, pressure drops in the evaporator and the condenser, kinetic and potential energy changes are neglected in the simulation and it is assumed that there are no leakings at the pipe connections and no heat loss to the environment from all equipments.

The simulation is accomplished in the Java programming language and contains 600 sec. time frame. The temperature-entropy (T-s) and the pressure-enthalphy (p-h) diagrams at the initial and the final states are given in Fig 3, Fig. 4, Fig. 5, and Fig. 6.

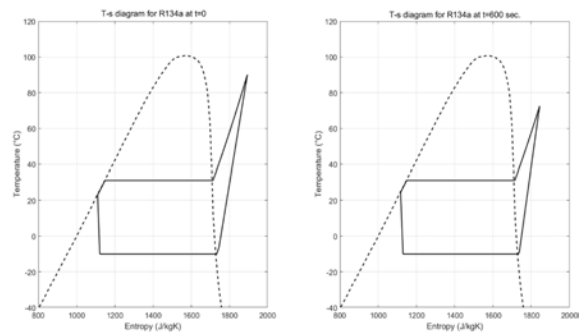


Figure 3. Temperature-entropy diagram for R134a at initial and final states

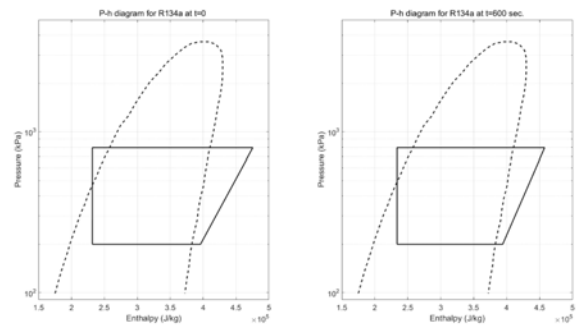


Figure 4. Pressure-enthalphy diagram for R134a at initial and final states

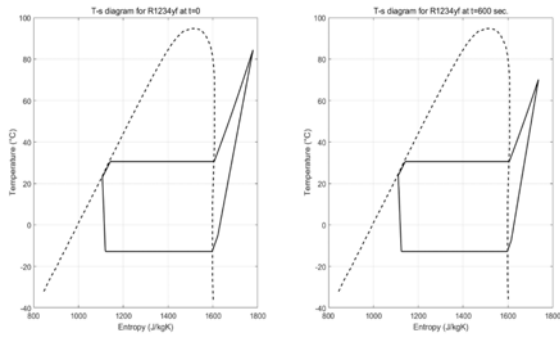


Figure 5. Temperature-entropy diagram for R1234yf at initial and final states

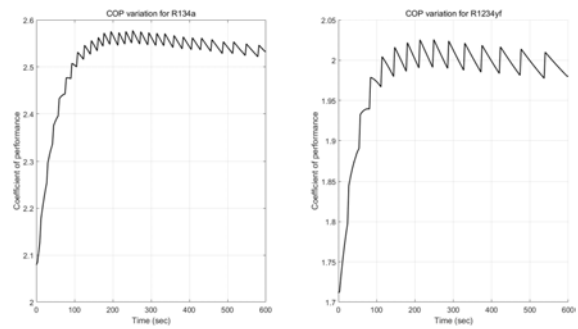


Figure 7. COP variation over time for R134a and R1234yf

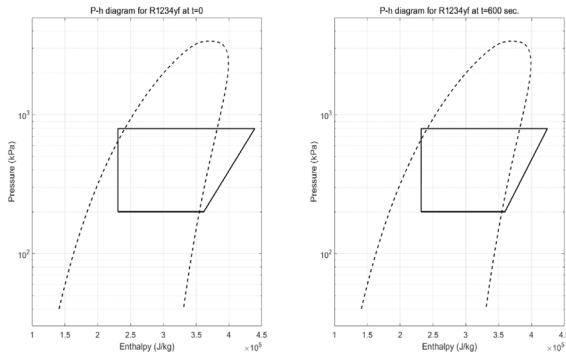


Figure 6. Pressure-enthalpy diagram for R1234yf at initial and final states

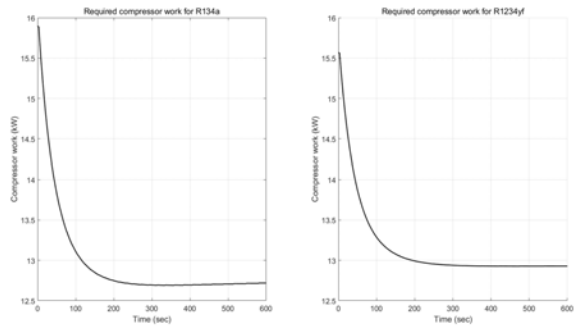


Figure 8. Required compressor work variation over time for R134a and R1234yf

By looking at the the Fig. 3, it is seen that, for R134a, the evaporator-, the compressor- and the condenser- outlet temperatures are initially -6.17°C , 90.07°C and 23°C , respectively and finally, they reach to -8.51°C , 71.85°C and 24.47°C . By looking at the the Fig. 5, it is seen that, for R1234yf, the evaporator-, the compressor- and the condenser- outlet temperatures are initially -5.15°C , 84.37°C and 23.01°C , respectively and finally, they reach to -7.45°C , 70.08°C and 23.86°C . By looking at these results, it can be seen that, the condenser and the evaporator wall temperature changes over time and thus the superheat and the subcool temperatures are decreased and increased, respectively, over time. Also, the compressor outlet temperature is decreased due to the heat transfer from the shell and the environment. The condenser and the evaporator temperatures are tend to get inside of the saturation dome. After these temperatures get inside of the dome, the system loses stability and the COP drops to zero. Variations of the COP, required compressor work and the cooling load over time for both R134a and R1234yf are given in Fig. 7, Fig. 8 and Fig. 9, respectively.

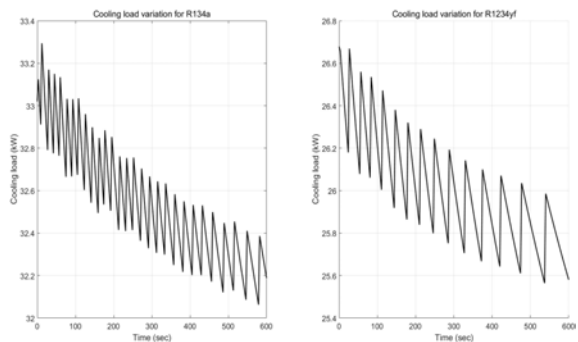


Figure 9. Cooling load variation over time for R134a and R1234yf

As can be seen in figures, since the superheat temperature decreases over time, required compressor work also decreases. Moreover, the zig-zags in the heat transfer behavior over time of the evaporator occur because of the

instabilities in the evaporation correlation. It can be seen in Fig. 9 that R134a absorbs more heat from the evaporator, however it requires similar amount of compressor work with R1234yf. Therefore, it can be concluded that performance of R134a is greater than R1234yf. The performance comparison is given in Fig. 7. This phenomena occurs because the thermodynamic and thermophysical properties of R134a is more favorable than R1234yf's. The system coefficient of performance ripples because of the zig-zags in the heat absorbtion from the evaporator and after a small overshoot, it slowly decreases. After the superheat temperature drops below zero, the COP value rapidly converges to zero.

CONCLUSION

In this study, the dynamic behavior of a vapor compression cycle with R134a and R1234yf working fluids is investigated. Modelling of the evaporator and the condenser is achieved with the finite difference method. Modelling of the compressor is accomplished with first, finite difference method, then the isentropic compression equation. Finally, modelling of the expansion valve is done with the orifice equation. The simulation results showed that the evaporator and the compressor wall temperatures decrease and increase, respectively, over time. Therefore, the superheat and the subcool temperatures decrease and increase, respectively, over time. After the the superheat and the subcool temperatures drops below zero, the system loses stability. Also, it is found that, the performance of R134a is better than R1234yf and required compressor work of the system and the heat absorption from the evaporator decreased over time. The coefficient of performance slowly decreased after a small overshoot. The authors plan to study on control algorithms that can maximize the system coefficient of performance in the future works.

References

- MacArthur JW. Transient heat pump behaviour: a theoretical investigation. *International Journal of Refrigeration* 7 (1984) 123–132.
- Yataganbaba A, Kilicarslan A, Kurtbas I. Exergy analysis of R1234yf and R1234ze as R134a replacements in a two evaporator vapour compression refrigeration system. *International Journal of Refrigeration* 60 (2015) 26–37.
- Chi J. DEPAc – a computer model for design and performance analysis of central chillers. ASME Paper No 77–HT–11, 1979.
- Chi J. Computer simulation of fossil-fuel-fired hydronic boilers, Second ASHRAE HVAC Equipment, 1976.
- Bonne, U, Patani, A. Modelling the influence of heat pump sizing, climate and test conditions on seasonal efficiency. Conference on HVAC Equipment and Systems, Purdue University, West Lafayette, Indiana, USA, 1978.
- Dhar, M, Soedel, W, Transient analysis of a vapor compression refrigeration system. XV International Congress of Refrigeration, Venice, Italy, 1979.
- Ellison RD, Creswich FA. A computer simulation of steady-state performance of air-to-air heat pumps, Oak Ridge National Laboratory Report ORNL/CON-1G, 1978.
- Chi J, Didion D. A simulation model of the transient performance of a heat pump. *International Journal of Refrigeration* 5 (1982) 176–184.
- Bonne, U, Patani, A, Jacobson, R, Muller, D. Electric-driven heat pump system: simulation and controls, ASHRAE Trans. LA-80-5 Los Angeles, California, 1980.
- Chen ZJ, Lin W. Dynamic simulation and optimal matching of a small-scale refrigeration system. *International Journal of Refrigeration* 14 (1991) 329–335.
- Fu L, Ding G, Zhang C. Dynamic simulation of air-to-water dual-mode heat pump with screw compressor. *Applied Thermal Engineering* 23 (2003) 1629–1645.
- Madani H, Claesson J, Lundqvist P. Capacity control in ground source heat pump systems part II: Comparative analysis between on/off controlled and variable capacity systems. *International Journal of Refrigeration* 34 (2011) 1934–1942.
- Zhu Y, Jin X, Du Z, Fan B, Fu S. Generic simulation model of multi-evaporator variable refrigerant flow air conditioning system for control analysis. *International Journal of Refrigeration* 36 (2013) 1602–1615.
- Mota-Babiloni A, Navarro-Esbri J, Barragán A, Moles F, Peris B. Drop-in energy performance evaluation of R1234yf and R1234ze(E) in a vapor compression system as R134a replacements. *Applied Thermal Engineering* 71 (2014) 259–265.
- Belman-Flores JM, Rodríguez-Munoz AP, Pérez-Reguera G, Mota-Babiloni A. Experimental study of R1234yf as a drop-in replacement for R134a in a domestic refrigerator. *International Journal of Refrigeration* 81 (2017) 1–11.
- Güngör KE, Winterton RHS. A general correlation for flow boiling in tubes and annuli. *International Journal of Heat and Mass Transfer* 29 (1985) 351–358.
- Travis DP, Baron AG, Rohsenow WM. Forced-convection condensation inside tubes. MIT Heat Transfer Laboratory, 74, 1971.
- Gnielinski V. New equations for heat and mass transfer in turbulent pipe and channel flow. *International Journal of Chemical Engineering* 16 (1976) 359–368.
- James KA, James RW. Transient analysis of thermostatic expansion valves for refrigeration system evaporators using mathematical models. *Transactions of the Institute of Measurement and Control* 9 (1987) 350–355.
- Tillner-Roth R, Baehr HD. A international standard formulation for the thermodynamic properties of 1,1,1,2-Tetrafluoroethane (HFC-134a) for temperatures from 170K to 455K and pressures up to 70 MPa. *Journal of Physical & Chemical Reference Data* 23 (1994) 657–729.
- Richter M, McLinden MO, Lemmon EW. Thermodynamic properties of 2,3,3,3-Tetrafluoroprop-1-ene (R1234yf): Vapor pressure and p–T measurement and equation of state. *Journal of Chemical & Engineering Data* 56 (2011) 3254–3264.
- Wagner W, Pru A. The IAPWS formulation 1995 for the thermodynamic properties of ordinary water substance for general and scientific use. *Journal of Physical & Chemical Reference Data* 31 (2002) 387–535.

Design Manufacture and Performance Test of A Reciprocating Refrigeration Compressor

Yusuf Ali Kara¹  Deniz Uzunsoy²  Hüseyin Lekesiz¹  Mustafa Gürkan Aydeniz³

¹Bursa Technical University, Department of Mechanical Engineering, Bursa, TURKEY

²Bursa Technical University, Department of Metallurgical and Materials Science, Bursa, TURKEY

³Yıldız Technical University, Department of Electrical Engineering, İstanbul, TURKEY

ABSTRACT

The first generation of refrigeration compressors is reciprocating type compressors, the second generation is scroll type, and the third generation is screw type compressors that are available on the market. Although the need of semi-hermetic refrigeration compressor in Turkey market is 15000 per year, there is no any domestic manufacturer of semi-hermetic refrigeration compressor, and consequently Turkey imports all of the refrigeration compressors from abroad market. In this study, the performance and the manufacturing processes of the semi-hermetic refrigeration compressor that is designed and manufactured with a hundred percent of domestic opportunities are investigated. The performance tests of the compressor are done, the catalogue of the compressor is prepared and it is 12 % more efficient in comparison with equivalent European one.

Keywords:

Semi-hermetic reciprocating refrigeration compressor; Calorimetric performance setup for refrigeration compressor

INTRODUCTION

The heart of the vapor-compression refrigeration machines are the compressors. The widely used refrigeration compressor types are the reciprocating, screw, centrifugal and vane. Reciprocating compressors consist of suction and discharge valves regulating pumping process and pistons moving back and forth in cylinders. The screw, centrifugal and vane compressors all use rotating elements. The workhorse of refrigeration industry is the reciprocating compressor, built in sizes ranging from fractional-kilowatt to hundreds of kilowatts of refrigeration capacity. Reciprocating compressors may be single-cylinder or multi-cylinder. In multi-cylinder compressors the cylinders can be arranged V-type, W-type, or in-line type. The working principle of reciprocating compressors as follows; low-pressure refrigerant is drawn into cylinder through a suction valve during suction stroke of the piston, then the piston compresses the refrigerant and pushes it out through a discharge valve during discharge stroke. Suction and discharge valves are usually located in the cylinder head. The reciprocating compressor may be open, hermetic, or semi-hermetic type. A compressor whose crankshaft extends through the compressor housing so that a motor can be externally coupled to the shaft is called open-type compressor. A seal must be used where the

shaft comes through the compressor housing to prevent refrigerant from leaking out. In hermetic-type compressor, motor and compressor are enclosed in the same housing to avoid the leakage at the seal. In this case, the motor is electrically insulated to operate even though it is in contact with refrigerant. The cold suction gas is drawn across the motor to keep the motor cool. Hermetic compressors are employed from 19th century and widely used in domestic refrigerators, air-conditioners because of their simplicity and flexibility of refrigeration capacity.

Many mathematical models and simulations of reciprocating compressors are available in open literature. Navarro et al. [1] proposed a new model for reciprocating compressors. The model solves out the general efficiency and volumetric efficiency by employing 10 empirical parameters that can be determined by curve fitting of experimental results. They proposed a curve fitting method based on Monte Carlo method that allows using some experimental results from the compressor's catalogue for curve fitting. Bin Yang et al. [2] proposed a comprehensive model for a semi-hermetic CO₂ compressor. The model consists of three sub-models that simulate kinematics, compression process and friction losses. The model is validated for compressor

Article History:

Received: 2018/01/23

Accepted: 2018/02/27

Online: 2018/09/07

Correspondence to: Yusuf Ali Kara
Bursa Technical University, Department
of Mechanical Engineering, Cevre Yolu
Avenue, Bursa, Turkey
Tel: 0(224) 300 34 12
E-Mail: yusufali.kara@btu.edu.tr

power and mass flow rate. Damle et al. [3] proposed an object oriented numerical simulation. Pe' rez-Segarra et al.[4] proposed a thermodynamics model calculating volumetric efficiency, isentropic efficiency and combined mechanical-electrical efficiency. Klein [5] proposed a semi-analytical model determining performance curve of a compressor. The model is validated by employing a calorimetric experimental setup. Refrigerant-12 is used as a heat source while cooling the condenser by a chiller. Flesch and Normey-Rico [6] designed a calorimeter for evaluating the performance of a refrigeration compressor; they proposed a model to calculate the performance parameters by using measured data.

In this study, designing, manufacturing and performance testing processes of a semi-hermetic, 4-piston refrigeration compressor is presented. All the processes are based on domestic facilities. The processes presented in this study are design, material selection, stress analysis, compressor manufacturing, motor design, manufacturing the rest of the compressor's components, and design and manufacturing of calorimetry.

MATERIAL AND METHODS

The Compressor

Thermodynamics design calculation of the compressor is done according to the model given by Bin Yang et al. [2]. Some geometrical dimension of the designed compressor is given in Table 1. The design of the compressor is done by using Solidwork (see Fig. 1). All of the components of the compressor are manufactured in Turkey.

Table 1. Compressor dimensions

Type	Semi-hermetic reciprocating refrigeration compressor
Number of piston	4
Bore diameter	55 mm
Stroke	39,5 mm
Revolution	1450 rpm
Displacement rate	0.009072 m ³ /s

Material selection

The microstructural investigation and chemical analysis of compressor bodies are performed in Bock and Bitzer



Figure 1. Explosion of designed and manufactured compressor

compressors in order to enlighten material selection of the designed compressor in this work. The cross sections of both compressors are subjected to metallographic investigation. The sample surfaces are grounded using 120,240,320,600,800 and 1200 mesh papers and polished using 6, 3 and 1µm diamond solutions. Fig. 2 and 3 show microstructural images of Bock and Bitzer compressor bodies and engine crank surfaces, respectively. The microstructural investigation of piston materials is performed for both compressors. Fig.4 shows microstructural investigation results of both piston materials

The systematic investigation is carried out for compressor body material selection as shown in Fig. 2 to 4. These systematic investigations lead to the selection of compressor body materials as GG 25. The chemical analysis results of the designed compressor body material are given in Table 2. Standard E-145 and E-171 are selected as piston and rod materials.

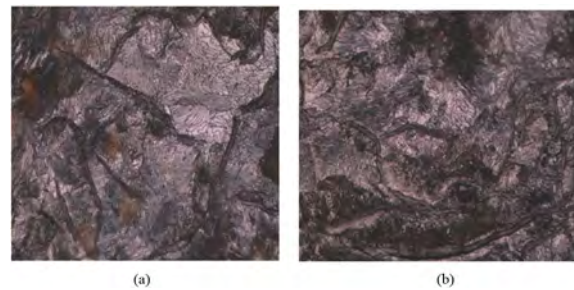


Figure 2. Microstructures of compressor (a) Bitzer trademark (b) Bock trademark

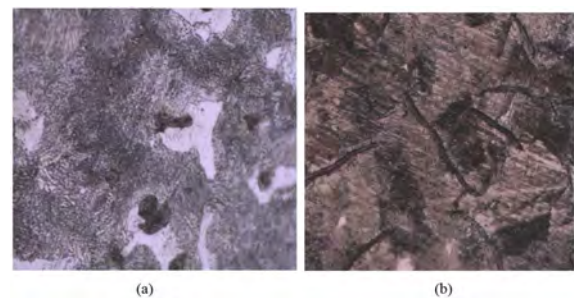


Figure 3. Microstructure of compressor crank and connecting rod surfaces (a) Bitzer trademark (b) Bock trademark

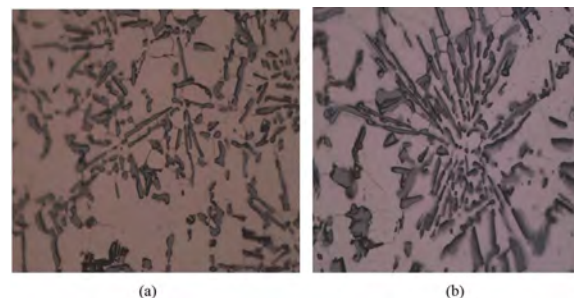


Figure 4. Microstructures of piston materials (a) Bitzer trademark (b) Bock trademark

Table 2. The chemical composition of the designed compressor body material

Material	C	Si	Mn	P	Si
GG25	3.28	2.14	0.750	0.014	0.023

Structural Reliability of Critical Parts

Compressor body and crankshaft are evaluated to be the most critical parts to check structural reliability because they are subjected to variable loading as a result of reciprocating motions. Therefore, displacement, strain and stress distributions of compressor body and crankshaft are analyzed using Finite Element Method by means of Solidworks Professional (Dassault Systèmes SOLIDWORKS Corp., Waltham, Massachusetts, USA). The membrane valve controlling the flow of cooling gas is not analyzed specifically because it is more prone to failure due to fatigue. Structural analysis of compressor body is executed for the conditions representing explosion of pressure tanks. According to this, a 4.6 MPa pressure is applied all over the inside of compressor body without assembling crankshaft, pistons and electric motor with caps kept closed. If compressor body can bear this much loading conditions, it is safe for service conditions which are less critical. For instance, maximum pressure experienced in service is 2.3 MPa and it occurs only inside of cylinders, not all over the inner side of compressor body. The Von-Misses stress distribution and displacement distribution for the compressor body under 4.6 MPa pressure is given in Figure-5 below. As can be seen from Fig. 5, the maximum stress (198 MPa) occurs around the center of cap at the pistons side. Compressor body is made of cast iron (GG25) and the maximum stress is much lower than the ultimate tensile strength of GG25. Ultimate tensile strength is approximately 327 MPa based on tensile testing of material. Maximum displacement is around 0.1432 mm and it is evaluated to a small displacement which does not lead to yielding. Considering the fact that analysis conditions are tougher than the actual service conditions, it is concluded that compressor body is structurally reliable. For the crankshaft dynamic conditions are necessary to be considered in the analysis due to its high angular velocity. For this purpose, a quasi-static approach is utilized where the maximum possible inertial loads are applied statically to the shaft. Velocity and accelerations are calculated based on rotational velocity created by electric motor. Pressure loads coming from piston heads and inertial effects determines the loading conditions on the crankshaft transferred by connecting rods. For one round of a crankshaft, all the loads are determined and the most critical case is determined to be 5373 N, 3063 N, 1719 N and 2243 N coming from all four connecting rods in the angles of 0°, 93°, 180° and 246° respectively. Crankshaft is constrained on one bearing radially, axially and tangentially while it is constrained only

radially on other bearing. With this type of boundary set up, the worsening effect of torque coming from electric motor is also taken into account for the most conservative estimate for reliability.

The maximum Von-Misses stress under these conditions is turned to be 184 MPa for the crankshaft and the maximum displacement is about 0.057 mm. These values are quite safe when the strength values of crankshaft material (forge steel) are considered. These analyses proved the structural reliability of compressor body and crankshaft under static and quasi-static conditions respectively. However, a modal analysis may also be necessary especially under high rate of rotational speeds. Modal analysis is also executed using Solidworks Professional and the frequencies for the first five modes are found to be 1680.7 Hz, 3585.5 Hz, 4996.2 Hz, 5304.6 Hz and 7749.9 Hz. The angular speed for service conditions is 24.16 Hz (1450 rpm) and this is much smaller than the frequency of first mode. Therefore, it is predicted that vibrations will not be a problem under the set-up considered in this compressor.

The Motor

In this study, three phase squirrel cage induction motor has been chosen as the drive motor of the compressor due to suitable for semi-hermetic refrigeration compressor and ease of manufacture. Design power of the compressor is 7.5 kW and revolutions per minute are 1450 rpm. In order to provide 7.5 kW output power of the motor, stator and rotor core length has been chosen as 120 mm.

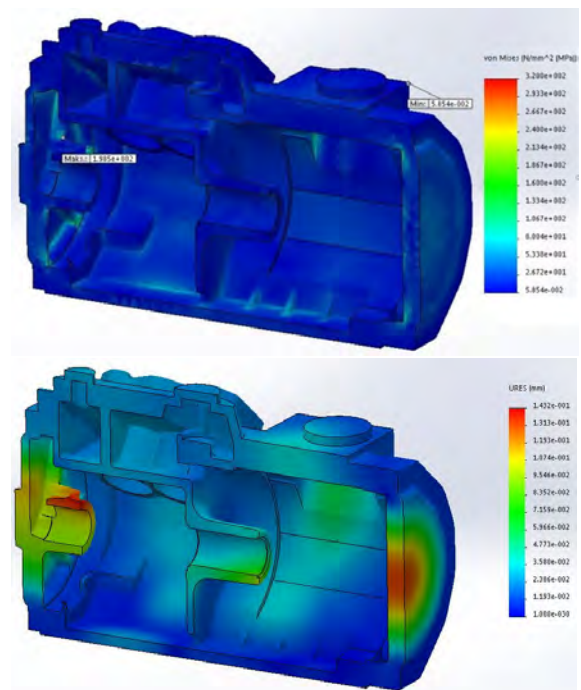


Figure 5. Finite element analysis results for compressor body (a) Von-Misses stress distribution (b) Displacement distribution

Table 3. Data for the designed induction motor

Number of stator slots	36
Outer diameter of stator	190 mm
Outer diameter of rotor	114 mm
Number of conductor per slot	27
Number of wires per conductor	3
Wire diameter	0.861 mm
Slot filling factor	51.2 (%)
Number of rotor slots	32
Air gap	0.5 mm
Inner diameter of rotor	32.65 mm
Skew width	1 slot

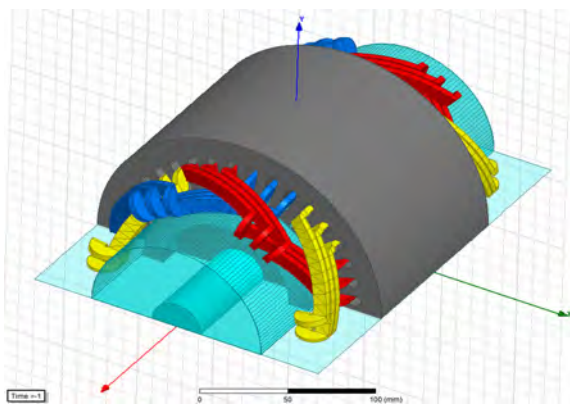


Figure 6. The cross-sectional image of the designed induction motor

In order to get desired speed, stator windings have been chosen as 4 poles. Since the compressor and motor will be in the same body, the stator outer and inner diameter values are defined as given in the Table 3. Performance analysis of the motor was carried out by using Maxwell, which software is using analytical and finite elements methods. As a result of the analysis, the motor is manufactured according to the data, which are given in Table-3 and placed in the main body of the compressor. Since the insulation of the winding wires is manufactured according to the coolant flow, the stator slot filling factor has been chosen about 50%. The cross-sectional image of the designed induction motor is given in Fig. 6.

Design and Manufacture of Calorimetric Setup

A calorimetric experimental setup is designed to determine the coefficient of performance (COP) of the manufactured compressor. The illustration of the setup is shown in Fig. 7. After charging oil into the manufactured compressor, it is connected to the setup. An oil separator is used after compressor exit to ensure a precise mass flow rate measurement of the working fluid, which is Refrigerant-404A.

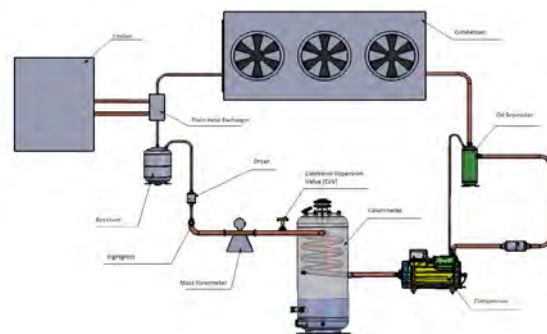


Figure 7. Calorimetric Experimental Setup

An air-cooled condenser with PID controlled-fan is used in the setup. The PID control on the condenser fan allows regulating the condensation temperature. The condenser unit is placed in outdoor environment. A plate heat exchanger (PHE) is used as subcooler that is connected to a chiller unit. Depending on the outdoor temperature, incomplete condensation may occur in the condenser. The subcooler ensures a complete condensation. Otherwise, incomplete condensation results in unstable working conditions, as a result, the system does not reach to steady conditions in case of incomplete condensation.

The Working Principle of Calorimeter

The calorimeter is the most important equipment of the experimental setup. Basically, the calorimeter is a tank containing a helical coil, refrigerant-134a, and electrical heater as it is seen from Fig. 8. R-404A, which is the working fluid of the experimental setup, boils while flowing through the coil. Heat sink to the coil is R-134a which is available at the bottom of the tank. The heater is immersed into liquid R-134a. The heater causes liquid R-134a to evaporate. And vapor of the R-134a rises and contacts to the coil and condenses on it while R-404A evaporates inside the coil. The state of R-404A is superheated vapor at the coil exit. The core idea designing the calorimeter is to provide an isothermal heat sink to the working fluid of R-404A. Charging pressure of the R-134a inside the tank is around 6 bar corresponding 20 °C saturation temperature. The heater is equipped with PID-capacity control that changes the heater power to ensure a desired super-

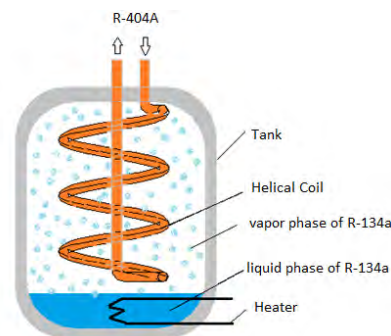


Figure 8. Calorimeter

heat of R-404A. Because refrigeration capacity of a compressor is given according to the superheat at the compressor inlet in compressor's catalogues, the superheat value is attained as a control parameter. The PID control of the heater measures the temperature of R-404A at the inlet of the coil and calculates desired temperature of the R-404A at the exit of the coil by adding a set value of superheat to the inlet temperature. The PID control arranges the heater power according to difference between the desired and the measured exit temperature.

The Calculations of Calorimeter

Heat transfer surface area of the coil and the pressure drop across the coil are important parameters for designing the coil. Heat transfer surface area of the coil is calculated as follow,

$$A_{s,coil} = \frac{Q_{ev}}{U \times (T_t - T_{ev})} \quad (1)$$

where $A_{s,coil}$, Q_{ev} , U , T_t , T_{ev} denote surface area of the coil based on outer diameter, refrigeration capacity of the compressor, overall heat transfer coefficient of the coil, saturation temperature of the fluid inside the tank (R-134a), and evaporation temperature of the fluid flowing inside the coil, i.e., R-404A, respectively. Q_{ev} in Eq. 1 must be the maximum refrigeration capacity of the compressor.

Total tube length of the coil,

$$L_{coil} = \frac{A_{s,coil}}{\pi \times d_o} \quad (2)$$

where L_{coil} is the open length of the coil tube, and d_o is outer diameter of the tube. The inner diameter of the tube is determined by calculating pressure drop.

Overall heat transfer coefficient for the coil is calculated as follows,

$$U = \frac{1}{\frac{1}{h_{coil,i}} + \frac{1}{h_{coil,o}}} \quad (3)$$

where $h_{coil,i}$ and $h_{coil,o}$ stand for convective heat transfer coefficient inside and the outside of the coil, respectively. The thermal resistance of the tube wall is ignored in Eq. 3.

Convective heat transfer coefficient inside the coil, $h_{coil,i}$, is called convective boiling heat transfer coefficient (CBHTC) in the literature. Correlations are available for CBHTC in helical coil [7-11]. The most famous one among those correlations is Schrock-Grossman's correlation [7,8]. Zhao et al.[8] made some modifications on Schrock-Grossman's correlation to make it more accurate, namely the accuracy of the modified correlation is around %12. The modified Schrock-Grossman's correlation is given below,

$$\frac{h_{coil,i}}{h_o} = 1.6 \left(\frac{1}{X_{tt}} \right)^{0.74} + 183,000 B_o^{1.46} \quad (4)$$

$$h_o = \frac{1}{41} Re_{lo}^{5/6} Pr_l^{0.4} \left(\frac{d_i}{D_{helix}} \right)^{1/12} \times \left(1 + \frac{0.061}{\left(Re_{lo} (d_i / D_{helix})^{2.5} \right)^{1/6}} \right) \frac{k_l}{d_i} \quad (5)$$

$$Re_{lo} = \frac{G d_i}{\mu_l} \quad (6)$$

$$X_{tt} = \left(\frac{1-x}{x} \right)^{0.9} \left(\frac{\rho_g}{\rho_l} \right)^{0.5} \left(\frac{\mu_l}{\mu_g} \right)^{0.1} \quad (7)$$

$$B_o = q / G^* i_{fg} \quad (8)$$

$$G = \frac{\dot{m}_r}{A_c} \quad (9)$$

$$q = \frac{Q_{ev}}{A_{s,coil}} \quad (10)$$

where $h_{coil,i}$ is CBHTC, h_o and Re_{lo} are liquid only heat transfer coefficient and Reynolds number for the total flow assumed to be liquid, d_i inner diameter of coil tube, D_{helix} is helix diameter of coil, X_{tt} is Martinelli parameter, B_o is boiling number, i_{fg} is enthalpy of vaporization, \dot{m}_r is mass flow rate of working fluid, G is mass flux, q is heat flux, Q_{ev} evaporation heat rate in the coil or another saying compressor refrigeration capacity, $A_{s,coil}$ is coil surface area, A_c is cross-sectional area of coil tube, and the subscript lo denotes for liquid only.

CBHTC, $h_{coil,i}$ in Eq. 4 is calculated depending on the quality, namely, x . Therefore, the local $h_{coil,i}$ is calculated by incrementing the quality, dx , from its value at the inlet of the coil to unity. Then, integral average of $\bar{h}_{coil,i}$ is calculated as follows,

$$\bar{h}_{coil,i} = \frac{\int_{x_i}^1 h_{coil,i} dx}{1 - x_i} \quad (11)$$

The quality at the coil inlet is calculated by using the correlation given below,

$$x_i = 0.00675 \left(1 + 0.001677 T_{cd,e} + 0.00472 T_{ev} \right) (T_{cd,e} - T_{ev}) \quad (12)$$

where $T_{cd,e}$ is temperature of working fluid (R-404A) at coil exit, T_{ev} is evaporation temperature inside the coil. Because laminar film condensation occurs at outer surface of the coil, i.e., tank side, the correlation known as Nusselt theory [12] is used for the tank side heat transfer coefficient.

$$h_{coil,o} = 0.729 \left[\frac{g \rho_l (\rho_l - \rho_v) k_i^3 i_{fg}'}{\mu_l (T_{cd} - T_w) d_o} \right] \quad (13)$$

where subscript v stands for vapor phase, T_{cd} is condensation temperature of R-134a inside the tank, T_w is wall temperature of the coil that is calculated as follows,

$$T_w = \frac{q}{h_{coil,i}} + T_{ev} \quad (14)$$

The parameter i_{fg}' in Eq. 3 is calculated as follows,

$$i_{fg}' = i_{fg} + 0.68 c_{p,l} (T_{cd} - T_w) \quad (15)$$

The coil surface area is calculated according to the flowchart given in Fig 9.

When the pressure drop is calculated, it must be taken into consideration that the flow is two-phase and the construction of the coil is helix. Two-phase flow pressure drop in a helical coil is calculated by using the correlation given by Zhao et.al.[8]. The correlation is given briefly for the reader convenience. Generally, the two-phase frictional multiplier is employed to correlate the frictional pressure drop of two-phase flow. Its definition is

$$\phi_{lo}^2 = \frac{\Delta P_{TP}}{\Delta P_{lo}} \quad (16)$$

where ΔP_{TP} is the two-phase flow frictional pressure drop and ΔP_{lo} is the single-phase frictional pressure drop. Zhao et al. [8] suggested following correlation, which has an uncertainty of $\pm 15\%$, for the two-phase frictional multiplier.

$$\phi_{lo}^2 = 1 + \left(\frac{\rho_l}{\rho_g} \right) \left[0.303 x^{1.63} (1-x)^{0.885} Re_{lo}^{0.282} + x^2 \right] \quad (17)$$

Friction factor for single-phase flow in helical coil is calculated by using White correlation [8].

$$f = 0.08 Re_{lo}^{-1/4} + 0.012 (d_i / D_{helix})^{1/2} \quad (18)$$

The single-phase frictional pressure drop is calculated as follows,

$$\Delta P_{lo} = 4f \frac{L_{coil}}{d_i} \frac{G^2}{2\rho} \quad (19)$$

where L_{coil} is total tube length of the coil and G is the mass flux.

Because the pressure drop through the coil is fulfilled by the tested compressor, the higher the pressure drops inside the coil, the lower the COP of compressor. Therefore, the two-phase flow frictional pressure drop calculated according to Eqs. 16-19 must be minimal for designing helical coil.

Refrigeration Capacity Calculations of the Compressor

The mass flow rate of the working fluid is measured by a mass flowmeter. Thermodynamic properties of the working fluid (R-404A) are calculated by using the equations given by Sözen et.al. [13].

Refrigeration capacity of the compressor is calculated as follows,

$$SPT = \frac{P_{fc} \cdot C_{fc}}{\rho} \quad (21)$$

where \dot{m}_r , $i_{coil,e}$ and $i_{coil,i}$ are mass flow rate and the enthalpies of the working fluid at inlet and outlet of the compressor.

The volumetric efficiency of the compressor is calculated as follows,

$$\eta_v = \frac{\dot{m}_r}{V_{sw}} \times v_{com,i} \quad (22)$$

where $v_{com,i}$ is specific volume of the working fluid at the compressor inlet.

The isentropic efficiency of the compressor is calculated as follows,

$$\eta_i = \dot{m}_r \frac{i_{com,isen} - i_{com,i}}{P_m} \quad (23)$$

where $i_{com,isen}$ is the isentropic enthalpy of working fluid at the compressor exit, $i_{com,i}$ is the enthalpy of the working fluid at the compressor inlet, P_m is the electrical power of the

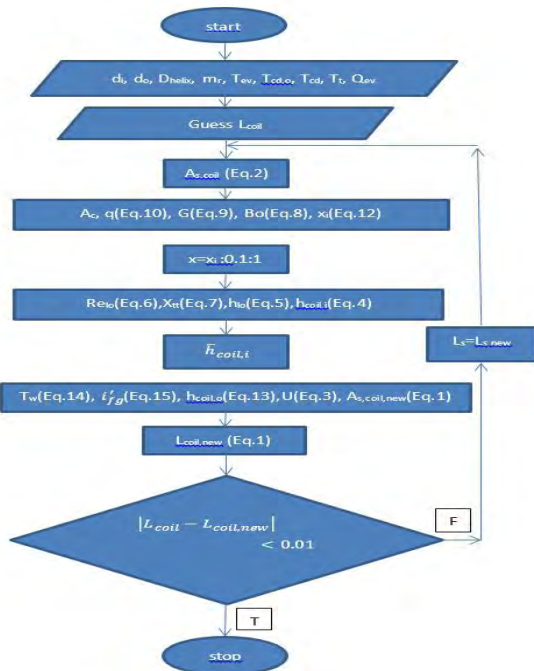


Figure 9. Flowchart

motor. V_{sw} is the displacement rate of the compressor and it is calculated as follows,

$$SPT_{sw} = \frac{C_{cy} P_e}{AEP \left[C_{cy} - \frac{C_{cond}}{\eta_{cs}} + \left(\frac{\eta_{ms}}{\eta_{cs}} - 1 \right) f_m \frac{C_{cond}}{\eta_{ms}} \right]} \quad (24)$$

where N_{cy} is number of cylinder (4), D_{cy} is diameter of cylinder (55mm), H is stroke (39.5mm), n is revolution per minute (1450 rpm).

Refrigeration coefficient of performance of the compressor (COP_R) is calculated as follows,

$$COP_R = \frac{\dot{Q}_{ev}}{P_m} \quad (25)$$

Where \dot{Q}_{ev} is calculated by using Eq. 21.

Condenser heat capacity is calculated as follows,

$$\dot{Q}_{cd} = \dot{m}_r (i_{cd,e} - i_{cd,i}) \quad (26)$$

Where $i_{cd,e}$ and $i_{cd,i}$ are enthalpy of working fluid at outlet and inlet of the condenser.

Subcooler heat rate is calculated as follows,

$$\dot{Q}_{sc} = \dot{m}_r (i_{sc,e} - i_{sc,i}) \quad (27)$$

where $i_{sc,e}$ and $i_{sc,i}$ are the enthalpies of working fluid at exit and inlet of subcooler.

Motor work rate is calculated as follows,

$$\dot{W}_{com} = \dot{m}_r (i_{com,e} - i_{com,i}) \quad (28)$$

Overall efficiency of the compressor is calculated as follows,

$$\eta_{com,g} = \frac{\dot{W}_{com}}{P_m} \quad (29)$$

where \dot{W}_{com} is calculated by using Eq. 28, P_m is the motor power that is measured.

MEASUREMENT, DATA ACQUISITION AND CONTROL

Working principle and control of the experimental setup

The automation, control and data acquisition system of calorimetric experimental setup work on following principle: simultaneous data reading from the sensors on the setup, saving those data on PLC, converting the saved data to desired units, inserting the converted data to the mathematical model given in the previous section and saving results, activating or inactivating required control functions depending on those saved results, rearranging analog outputs of some of the control functions and then saving the yielded raw data, converted data and results

of calculations on arrays of PLC, importing those data arrays to a USB file through USB port located on HMI.

Instrumentation

Uninsulated, flat-surface PT100 and PT1000 sensors are used for temperature measurements to ensure a short response time and high accuracy. Also, these sensors are placed into their slots on the experimental setup by applying heat transfer paste. The uncertainty and conversion accuracy of the PT100 and PT1000 sensors are ± 0.1 °C, ± 0.01 °C and 0.1 °C, 0.01 °C, respectively. Analog signals of the sensors are transferred to the PLC via PT100/PT1000 data input module of the PLC's manufacturer.

Pressure transmitters are chosen as 4-20mA output signal, because of possible static electricity and EMI effects. Analog signals of the transmitters are transferred to the PLC via 4-20mA data input module of the PLC's manufacturer. Measuring range of the transmitters is chosen in two different types due to pressure level of the system. Meanwhile, -0.8 to 7 bar measurement range is chosen in low level pressure part of the system, 0 to 30 bar measurement range is chosen in high level pressure part of the system.

Energy analyzer is used to measure electrical current, voltage, cosØ, frequency, and both real time and total consumption of power. In measurement of the current, the current transformers are used, which have C1:0.5 accuracy class and they are certified by UEDAŞ laboratory. Data acquisition between energy analyzer and PLC is done via RS 485/2 port by using MODBUS RTU protocol with 38,600 bps.

Rotational speed of the condenser fans and subcooler pump are controlled with an AC inverter and the power of the heaters is controlled by a SRC unit with 50 kW. Both the inverter and the SRC are controlled by the PLC. Mass flow rate of the working fluid of R-404A is controlled by using electronic expansion valve (ExV) that has a DANFOSS® EKD 316 superheat controller. Data acquisition between the superheat controller and PLC is done via RS 485/2 port by using MODBUS RTU protocol with 38,600 bps.

A Coriolis type mass flowmeter is used for measuring mass flow rate of R-404A. Data acquisition between the flowmeter and PLC is done via RS 485/2 port by using MODBUS RTU protocol with 38,600 bps. The oil flow rate is measured by using a mass flowmeter with pulse signal output that is converted to desired units via high speed HSC counter placed on the PLC.

A touch-screen with high resolution HMI is used to start the experimental setup, enter the input parameters, and monitor tables, graphics and analogue or digital data. The HMI has a large data saving capacity and it is capable

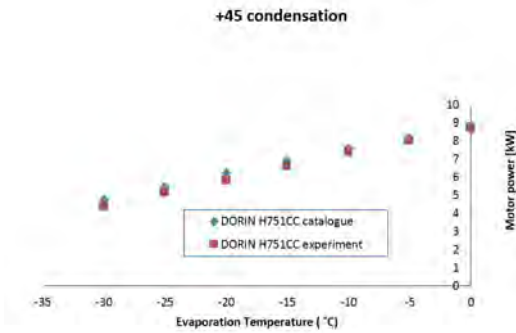


Figure 10. Experimental validation of the calorimetric setup: the motor power consumption.

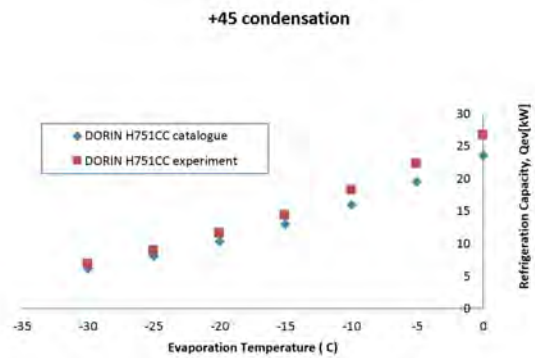


Figure 11. Experimental validation of the calorimetric setup: Refrigeration Capacity

to import data to USB. Data acquisition between HMI and the PLC is done via RS 232 port by using MODBUS RTU protocol with 115,200 bps.

A high speed PLC having a particular MCU that is capable of doing 32 bite float mathematical operations is preferred. The PLC has a CPU with 19 ns cycle speed. Analog to digital conversion of all analogue sensors and transmitters is done in 69 ms and also finishes all of the communications via MODBUS RTU protocol in 160 ms. The cycle duration for the entire programme 97 ms and the programme runs independent of communication process.

Besides the equipment mentioned above, various relays, fuses, power contactors, and terminal blocks are used.

RESULTS AND DISCUSSION

The coil, i.e., evaporator, is designed by a code written according to the flowchart based on the model given in the previous sections. Considering manufacturing limitations, inner diameter of coil tube and helix diameter of the coil are attained as $d_i = 12$ mm and $D_{helix} = 125$ mm, respectively. As results, the total tube length of the coil is calculated 43 m and corresponding pressure drop is calculated as 18.7 MPa, which is unacceptable. Governing parameters on the pressure drop are tube diameter, total tube length and mass flow rate. It is not reasonable to increase the tube diameter because of manufacturing limitations. The largest tube diameter that we enable to manufacture coil is limited to $\frac{1}{2}$ inch. Therefore, in order to decrease the pressure drop, the total length of the tube is divided into 7 parts and 7 identical helical coils are manufactured. The flow rate for every coil is decreased by one out of seven in this case. Therefore, decreasing the tube length and flow rate one out of seven, it is expected to decrease the pressure drop dramatically because the tube length and the flow rate for any coil are a multiplier

factors as it is seen from Eqs. 16 to 19. Thus, running the code again with this new design approach yields 0.054 MPa of pressure drop that is acceptable. As a result, 7 identical helical coils are manufactured, one of the helical coils is placed on center and while the rest are placed in circumference of the tank. A refrigerant distributor is used to ensure an equal mass flow through each coil.

As it is mentioned before, R-134a as a seconder fluid is charged into tank with 5.7 bar and 20 °C. A sight glass is placed on the tank wall at the bottom side for surveillance if the liquid level of the R-134a above the heaters. Besides, pressure and temperature inside the tank are measured with a pressure transmitter and a PT100 sensor to check if the design conditions are satisfied.

Because the calorimetric experimental setup is our own product, first of all, experimental validation is necessary. For this purpose, a H751CC model DORIN® compressor that is European original trademark is tested via the calorimetric experimental setup and the measured performance parameters are compared with those given in the compressor’s catalog. Results are given in Fig. 10 to 12.

Fig. 10 shows the comparison of the motor power while Fig. 11 is showing refrigeration capacity. As it is seen from those figures, values given in the catalog for both motor power and refrigeration capacity are in good agreement with those experimentally measured data by using the setup. Refrigeration COP of the compressor is compared in Fig. 12. As it is seen from the figure, the deficiency between the measured values and catalog values for COPR are around 11-15 % . The uncertainty calculated by using the method given by Kline and McClintock [14] for the COPR is $\pm 10.3\%$. Considering the uncertainty of $\pm 10.3\%$ and the uncertainty of the catalog’s values, the deficiency in Fig. 3 is in acceptable limitations. As results Fig. 10 to 12 shows that the validity of

Table 4. Design results of the coil

L_{coil}	$A_{s,coil}$	item	d_o	d_i	D_{helix}	ΔP_{TP}	m_r	U	T_{cd}	T_{ev}	Q_{ev}
m	m ²		mm	mm	mm	bar	kg/s	W/m ² K	°C	°C	W
6,77	0,27	7	12,7	12	125	0,54	0,0434	1338,99	30	5	5428

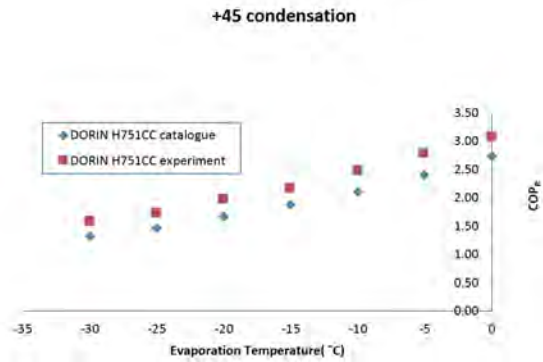


Figure 12. Experimental validation of the calorimetric setup: Refrigeration coefficient of performance

test results from the experimental setup is always reliable.

After validating the experimental setup, the manufactured compressor is tested by employing the setup. The parameters such as refrigeration capacity, motor power and COPR, which are necessary performance parameters that

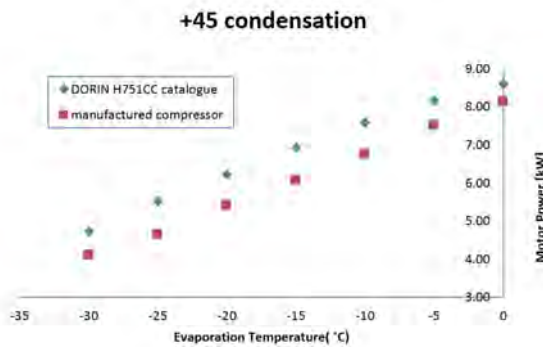


Figure 13. The motor power consumption

a compressor catalog must contain, are determined and a compressor catalog is prepared [15]. The performance parameters mentioned above are calculated by using the mean values of 50 measured data saving 30 s time intervals.

Fig. 13 shows the comparison of the motor power of the manufactured compressor and DORIN compressor. As seen, the manufactured compressor consumes less power comparing to DORIN. It is better to compare both of the

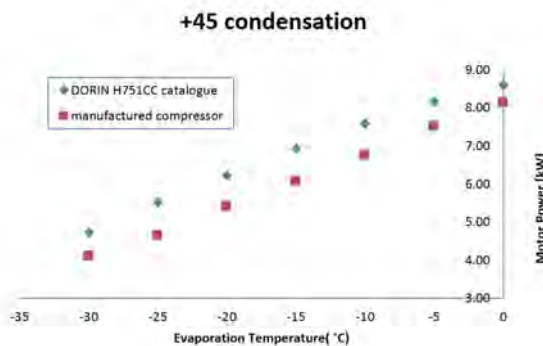


Figure 14. Refrigeration Coefficient of Performance

compressors with a dimensionless parameter of COPR. Fig. 14 shows the comparison of COPR of the compressors. As seen, the COPR of the manufactured compressor is higher than that of DORIN compressor's by around 12%. As a result, performance of the first domestic compressor of Turkey is as good as an equivalent European original.

ACKNOWLEDGEMENT

This project is implemented in corporation with Gökçeler Refrigeration Company, and funded by The Scientific and Technological Research Council of Turkey (TUBITAK) with the project number of TEYDEP1507- 7140320. The authors thank to TUBITAK and Gökçeler Refrigeration Company for their contributions.

Symbols and Abbreviations

Symbols		Subscripts	
q	Heat flux [W/m ²]	a	atmosphere
Bo	Boiling number	c	cross-sectional
x	Quality	cd	condenser
H	Stroke [m]	com	compressor
Q	Heat rate [W]	cy	cylinder
i	Enthalpy [kJ/kg]	e	exit
T	Temperature [°C]	ev	evaporator
\dot{m}	Mass flow rate [kg/s]	i	inner, inlet
d, D	Diameter [m]	l	liquid
L	Length [m]	lo	liquid only
k	Heat conduction coefficient [W/mK]	m	motor
G	Mass flux [kg/m ² s]	o	outer
h	Convective heat transfer coefficient [W/m ² K]	r, R	refrigerant, refrigeration
f	Friction factor	s	surface
A	Area [m ²]	sc	subcooler
V	Displacement [m ³ /s]	t	tank
U	Overall heat transfer coefficient [W/m ² K]	TP	two-phase
X_{tt}	Martinelli number	v	volumetric
n	Rotational speed [rpm]	w	wall

Abbreviations

COP	Coefficient of performance	PLC	Programmable logic controller
PID	Proportional-Integral-Derivative controller	HMI	Human Machine Interaction
USB	Universal Serial Bus	HSC	High speed counter
PT	Platinum temperature sensor	CPU	Central Process Unit
ExV	Electronic Expansion Valve	UEDAŞ	Uludağ Electric Company
MODBUS RTU	MODBUS Remote Terminal Unit		

REFERENCES

1. Navarro E, Granryd E, Urchuegui JF, Corberan JM. A phenomenological model for analyzing reciprocating compressors. *International Journal of Refrigeration* 30(2007)1254 – 1265.
2. Yang B, Bradshaw CR, Groll EA. Modeling of a semi-hermetic CO₂ reciprocating compressor including lubrication submodels for piston rings and bearings. *International journal of refrigeration* 36(2013) 1925 – 1937.
3. Damle R, Rigola J, Pe´rez-Segarra CD, Castro J, Oliva A. Object-oriented simulation of reciprocating compressors: Numerical verification and experimental comparison. *International journal of refrigeration* 34(2011)1989 – 1998.
4. Pe´rez-Segarra CD, Rigola J, So`ria M, Oliva A. Detailed thermodynamic characterization of hermetic reciprocating compressors. *International Journal of Refrigeration* 28(2005)57 – 59.
5. Klein SA. Develop Data Base for Determining Optimum Compressor Rating Points for Residential Refrigerator and Freezer Compressors. ASHRAE RP-870 (1999)
6. Flesch RCC, Normey-Rico JE. Modelling identification and control of a calorimeter used for performance evaluation of refrigerant compressors. *Control Engineering Practice* 18(2010)254 –261.
7. Elsayed AM, Raya K, Dadah AL, Mahmoud S, Rezk A. Investigation of flow boiling heat transfer inside small diameter helically coiled tubes. *International Journal of Refrigeration* 35(2002) 2179 – 2187.
8. Zhao L, Guo L, Bai B, HouY, Zhang X. Convective boiling heat transfer and two-phase flow characteristics inside a small horizontal helically coiled tubing once-through steam generator. *International Journal of Heat and Mass Transfer* 46(2003) 4779 – 4788.
9. Chung YJ, Bae KH, Kim KK, Lee WJ. Boiling heat transfer and dryout in helically coiled tubes under different pressure conditions. *Annals of Nuclear Energy* 71(2014) 298 – 303.
10. Wongwises S, Polsongkram M. Evaporation heat transfer and pressure drop of HFC-134a in a helically coiled concentric tube-in-tube heat exchanger. *International Journal of Heat and Mass Transfer* 49(2006) 658 – 670.
11. Cui W, Li L, Xin M, Jen TC, Chen Q, Liao Q. A heat transfer correlation of flow boiling in micro-finned helically coiled tube. *International Journal of Heat and Mass Transfer* 49(2006) 2851 – 2858.
12. Kakaç S, Liu H. *Heat Exchangers: Selection, rating and thermal design*. CRC Press, 2012.
13. Sözen A, Arcaklioğlu E, Menlik T. Derivation of empirical equations for thermodynamic properties of a ozone safe refrigerant (R404a) using artificial neural network. *Expert Systems with Applications* 37(2010)1158 – 1168.
14. Holman JP. *Experimental Methods for Engineers*, 6th ed., McGraw-Hill, Singapore, 1994.
15. Gökçeler A.Ş., <http://www.gokcelersogutma.com.tr/>

Investigation Of Working Temperature Effect On Micro-Cogeneration Application Of Proton Exchange Membrane Fuel Cells

Yağmur Budak¹  Ekin Özgirgin Yapıcı²  Yılsır Devrim¹ 

¹Atılım University, Department of Energy Systems Engineering, Ankara, TURKEY

²Çankaya University, Department of Mechanical Engineering, Ankara, TURKEY

ABSTRACT

In this study, micro-cogeneration application is used to increase the efficiency of Proton Exchange Membrane Fuel Cell (PEMFC) systems and effect of different operation temperatures on system performance is observed. For this reason, two different PEMFC systems were comparatively studied operating at 70°C and 160°C, respectively. Micro-cogeneration system design has done considering experimentally determined current density, power and temperature values. Since the amount of heat extracted from each PEMFC system is different related to the operating temperatures, different heat transfer fluids have been used for the cooling systems. These systems are designed for utilization of electricity and hot water for Atılım University Hydrogen Energy Laboratory. Heat loss calculation is made for the laboratory and thermal energy needed for heating the laboratory is calculated. Parallel to the design calculations, simple payback times for PEMFCs with micro-cogeneration applications were determined. LT-PEMFC and HT-PEMFC systems have 402 W and 456 W thermal powers respectively and 87.4 % and 92.8 % total cogeneration efficiencies were calculated for each system respectively. For each system maximum water temperatures and flow rates are calculated as a result of micro-cogeneration application. HT-PEMFC system has found to be capable of higher amount of heating. Even LT-PEMFC system has a lower thermal power and efficiency; it is determined to be more economical and has a lower pay pack time then HT-PEMFC system. For both systems, necessary number of stacks to be used for laboratory heating is calculated as four.

Article History:

Received: 2018/01/31

Accepted: 2018/02/27

Online: 2018/09/07

Correspondence to: Ekin Özgirgin Yapıcı
Çankaya University, Faculty of Engineering,
Department of Mechanical Engineering,
06790, Ankara, Turkey
Tel: +90 (312) 233-13-00
E-Mail: ekinozgirgin@cankaya.edu.tr

Keywords: Proton Exchange Membrane Fuel Cell, Micro-cogeneration, Hydrogen energy

INTRODUCTION

With the increasing population and developing technology, energy demand is increasing more and more. Nowadays, most of the energy required is provided from primary resources which are called as fossil fuels like petroleum and natural gas and as a result of the use of these limited and declining resources, environmental pollution and global warming occurs. In this extent, use of clean, environmentally friendly, low price, natural renewable energy resources are spreading. Hydrogen, which is a clean energy carrier, is one of the most important renewable energy resources. Fuel cell systems are electrochemical systems which use hydrogen energy to produce electrical energy. Fuel cell technology is reliable and is capable of achieving higher efficiencies, with lower emissions among the renewable energy technologies. Among all fuel cells, proton exchange membrane type fuel cells (PEMFC) gain the highest

interest because of their high performances, high power densities, modular structures, small size and low operating temperatures [1]. Besides mobile and stationary applications of PEMFC's in industry and defense sector, recently household or mobile co-generation applications have become a current issue. PEMFC's are classified into two categories; operation temperatures between 60- 80 °C are called low temperature PEMFC's (LT-PEMFC) and operation temperatures above 100°C are called high temperature PEMFC's (HT-PEMFC) [2]. HT-PEMFCs have high CO tolerances, easy heat removal and have developed electrode kinetics and they do not need to be humidified [3]. LT-PEMFCs have low operation temperatures, high gas impermeability and they are more economical [4].

Heat released during electricity production in PEMFC's should be removed with the help of cooling

fluid or air cooling systems for high performance and a stable operation [5]. For especially HT-PEMFCs, where air cooling is less effective, liquid cooling fluid is pumped among the cell via cooling channels to remove the excess heat [6]. The utilization of removed heat simultaneously with the electrical energy of the PEMFC system enables to recover the heat otherwise should be wasted and increase the total efficiency of the system as to about 85-90%. This way the system utilizes energy more economically and effectively. Such applications are named as micro-cogeneration applications [2]. To supply the necessary thermal load (heating requirement) of a building or a space, first the heat loss and the corresponding heat demand should be calculated. During calculations, wall structural components, window and door properties and all relevant dimensions have great importance.

One of the most important issues for operation of fuel cells is the feasibility of the fuel cell system. Simple payback time calculation is a simple but effective methodology for determination of feasibility of a fuel cell system. This method simply shows how fast the investment pays its initial cost back and is a means for comparing different systems but inflation, or changes in electricity and natural gas prices are not considered [2].

MATERIAL AND METHODS

In this study, comparison of micro-cogeneration applications of a LT-PEMFC system with 480 W of electrical power and a HT-PEMFC system with 480 W electrical power has been done operating on 0.6 V cell voltage. Different types of membranes are used for the different systems. The excess heat produced by the fuel cells is used for heating Hydrogen Energy Laboratory in Atılım University. For that, heat loss calculations have been done for determination of the necessary heat load of the laboratory.

To see the economic advantage of micro-cogeneration system, simple pay back times (SPT) for LT-PEMFC and HT-PEMFC systems were calculated before and after cogeneration applications.

Schematically representations of LT-PEMFC and HT-PEMFC systems are shown in Fig. 1. In Figure 1.a flow diagram of the LT-PEMFC system can be seen where air first passes through the filter then with the help of the compressor air is flown into the humidifier.

Fig. 1.b shows HT-PEMFC system. In this system, air firstly passes through the filter, then through the compressor and then to the pre heater. In both systems, hydrogen is fed to the PEMFC via hydrogen tanks. In HT-PEMFC system, hydrogen is heated in the pre-heater before being

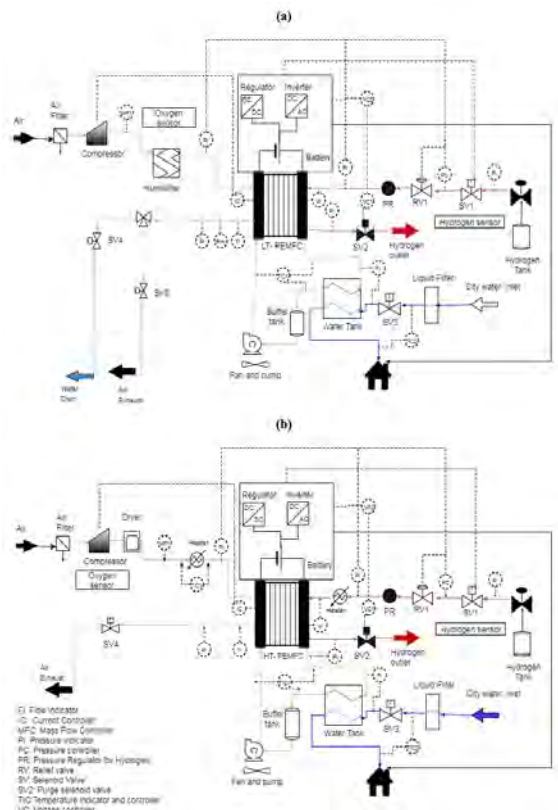


Figure 1. a) LT-PEMFC and b) HT-PEMFC micro-cogeneration applications flow diagrams

fed to the system. Properties of the PEMFC systems can be seen in Table 1.

Excess heat of the fuel cell system is removed by using heat transfer oil 32 (Petrol Ofisi) and water in the water tanks are heated by the heat transfer oil. This heat is used for space heating purposes and the cooled heat transfer oil passes through circulation tank equipped with a fan and pumped back to the cell. All flows are controlled by valves and control equipment.

Table 1. LT-PEMFC and HT-PEMFC stack properties

PEMFC type	Parameters	Value
LT-PEMFC	Current Density (0.6 V/cell)	0.9 A/cm ²
	Membrane	Nafion 212
	Active Area	150 cm ²
	Cell number	6
HT-PEMFC	Max. Power @0.6 V/cell	480 W
	Current Density (0.6 V/cell)	0.41 A/cm ²
	Membrane	Polybenzimidazole (PBI)/H ₃ PO ₄
	Active Area	150 cm ²
	Cell number	13
	Max. Power @0.6 V/cell	480 W

THEORY AND CALCULATIONS

Assumptions used in the calculations are:

- PEMFC micro-cogeneration systems operate in steady state conditions.
- The ideal gas principles are applied to gases.
- One-dimensional flow is assumed.
- The kinetic and potential energy changes are negligible.
- LT-PEMFC stack consist of Nafion® 212 membrane, HT-PEMFC stack consist of PBI membrane
- Working temperature of the LT-PEMFC stack is 70°C at 100% humidity and working temperature of the HT-PEMFC stack is 160°C with dry gas feed.

PEMFC Stack Calculations

H₂ flows into the PEMFC at the anode gas inlet. The H₂ concentration N_{H₂} at the inlet depends on the current density I (A/cm²), stoichiometric ratio H₂, S_{H₂}, cell active area A (cm²) and number of cells N_{cell}. The H₂ concentration at the anode gas inlet of the PEMFC is calculated by Eq. 1. F is the Faraday constant.

$$N_{H_2} = S_{H_2} \cdot \frac{I \cdot A}{2 \cdot F} \cdot N_{cell} \quad (1)$$

Air is fed to PEMFC at the anode gas inlet. Oxygen concentration in air is 21 %. NO₂ is concentration of oxygen and N_{air} is concentration of air. The concentration of O₂ depends on the current density I, cell active area A, number of cells N_{cell} and stoichiometry of O₂. The concentration of O₂ and air are calculated as follows:

$$N_{O_2} = S_{O_2} \cdot \frac{I \cdot A}{4 \cdot F} \cdot N_{cell} \quad (2)$$

$$N_{air} = \frac{S_{O_2}}{r_{O_2}} \cdot \frac{i \cdot A}{4 \cdot F} \cdot N_{cell} \quad (3)$$

The energy balance for a PEMFC stack system is expressed with the following equation:

$$\sum \dot{E}_{mass,in} - \sum \dot{E}_{mass,out} + \dot{Q} - \dot{W}_{net} = 0 \quad (4)$$

In Equation 4, $\sum \dot{E}_{mass,in}$ is the total enthalpy of the inlet gasses and $\sum \dot{E}_{mass,out}$ is the total enthalpy of the outlet gasses. For the low temperature cell, air is humidified at the inlet; and there is also water vapor among the inlet gases. \dot{Q} refers to the heat dissipation from the PEMFC stack to the ambient, \dot{W}_{net} denotes the net power of the cell stack.

PEMFC Heat Loss Calculations

Maximum heat loss from the cell stack by natural convection and radiation is calculated by Eq. 5.

$$\dot{Q}_{loss} = \frac{T_s - T_o}{R_{th}} \quad (5)$$

In Eq. 5, \dot{Q}_{loss} denotes the heat loss, T_s is the stack surface temperature, T_o is the ambient temperature (room temperature) and R_{th} is the thermal resistance. Heat losses from the low temperature cells can be neglected but for the high temperature cells, heat loss is too high to be neglected. To prevent this much heat loss from the cell surface, HT-PEMFC stack is insulated by means of an insulation material. The optimum thickness of the insulation material which was chosen to be glass wool is calculated by the following equation.

$$\Delta x = \frac{k \cdot \Delta T \cdot A}{Q_{loss}} \quad (6)$$

Here, k is the thermal conductivity, ΔT is the difference between T_s and T_o and A is the heat transfer area of the HT-PEMFC stack.

Micro- Cogeneration System Calculations

PEMFC System efficiency given in Eq. 9 is the sum of electrical efficiency of the stack (Eq. 7) and thermal efficiency of the stack (Eq. 8)

$$\eta_{el} = \frac{P_{exit}}{\dot{n}_{H_2} \times LHV} \quad (7)$$

$$\eta_{th} = \frac{P_{cooler}}{P_{H_2}} = \frac{\dot{m}_{ss} \cdot c_{p,cl} \cdot \Delta T_{cl}}{P_{H_2}} \quad (8)$$

$$\eta_{cogeneration} = \eta_{el} + \eta_{th} \quad (9)$$

In this equation; \dot{n}_{H_2} is the hydrogen molar flow rate and LHV is the lower heating value of hydrogen gas (241.83 kJ/mol).

Energy balance in the water tank can be calculated by Eq. 10.

$$\dot{m}_{cl} c_{p,cl} \Delta T_{cl} \Delta \eta = \dot{m}_w c_{p,w} \Delta T_w \quad (10)$$

In this equation, \dot{m}_{cl} and \dot{m}_w are mass flow rates of cooling liquid and heating water respectively. $c_{p,cl}$ and $c_{p,w}$ are constant specific heat values of cooling liquid and heating water respectively. ΔT_{cl} and ΔT_w are cooling liquid inlet and exit temperature difference and heating water inlet and exit temperature difference respectively. η denotes the PEMFC system heat exchange effectiveness and in this study, it is estimated that about 10% of the heat is lost to the surrounding.

Simple Payback Time Calculations

For application of cogeneration, PEMFC system is estimated to be operating 10 hours per day for 6 months. Electrical production is calculated based on this estima-

tion. Annual electrical production (AEP) is calculated in Eq.11.

$$AEP = 8760 \times CF \times P_{fc} \quad (11)$$

In Eq.11, CF is the capacity factor which is the ratio of produced power in a specified time to maximum possible power production of the system operating on its rated power during same period and P_{fc} is the PEMFC system nominal power. PEMFC systems are estimated to operate at their rated (maximum) power during the studied time.

Payback time of the PEMFCs is calculated by Equation 12 seen below.

$$SPT = \frac{P_{fc} \cdot C_{fc}}{AEP \cdot \left[C_{el} - \frac{C_{hg}}{\eta_{fc}} \right]} \quad (12)$$

In this equation; C_{fc} is fuel cell price, C_{el} (TL/kWh) is the cost of produced electricity. C_{hg} is natural gas price in TL/kWh, η_{fc} is average annual efficiency of the cell stack system. Since the produced power is constant for PEMFC system, average annual efficiency is equal to the system efficiency. The cost of the PEMFC is determined upon an amount of 1000 production annually which decreases the unit price [4].

Ratio between the heat actually utilized in cogeneration and the heat produced by a PEMFC system is called heat utilization factor and is very important for SPT calculations of PEMFC. It can be seen in Eq. 13.

$$\frac{Q_{cogeneration}}{Q_{heat\ production}} \quad (13)$$

Simple payback time of the micro-cogeneration application of PEMFCs is calculated by Eq. 14;

$$SPT_{chp} = \frac{C_{fc} \cdot P_{fc}}{AEP \cdot \left[C_{el} - \frac{C_{fuel}}{\eta_{el}} + \left(\frac{\eta_{tot}}{\eta_{el}} - 1 \right) \cdot f_{hu} \cdot \frac{C_{fuel}}{\eta_{heat}} \right]} \quad (14)$$

where, η_{tot} is the total PEMFC efficiency, f_{hu} is the heat utilization factor and η_{heat} is the natural gas combustion efficiency.

Calculation of Heat Loss and Necessary Thermal Load For the Laboratory

Thermal energy needed for heating the laboratory where micro-cogeneration is applied is calculated using computer software called; NZN. There are 4 different temperature zones in Turkey regarding the average seasonal temperatures and Ankara is in the 3rd temperature zone.

Constructional components of the Hydrogen Energy Laboratory located at the -1st floor of Atilim University in

İncek, Ankara can be seen in Table 2. Each component has different value of thermal conductivity. In Figure 2, Laboratory schematically representation can be seen with the required dimensions.

Table 2. Constructional components of walls

External wall	Internal wall
Ferroconcrete	Reinforced concrete wall
Pumice Concrete	Rough cast
Rough cast	Gypsum plaster
Condensed XPS	
Carbon based foam material	Exterior Paint
Stucco	
Exterior Paint	

Thermal load calculations have been done considering the temperature differences between the laboratory and the adjacent rooms, corridors or outside. Also regarding the directions, external and internal wall areas, doors and windows play an important role on calculation of heat loss through a room. Besides that, thickness of constructional components of walls has a great impact on the thermal resistance thus the heat loss as well.

All important properties of constructional components are given in Table 3. For the calculations of areas of the wall, doors and windows are excluded for a more precise solution of thermal energy needed for heating the laboratory.

RESULTS AND DISCUSSION

PEMFC Results

Firstly, for performance characteristics LT-PEMFC and HT-PEMFC systems were studied and relevant results were given in Fig. 3a and 3b respectively. For both systems, design power value of 480 W at 0.6 V cell voltage have successfully obtained.

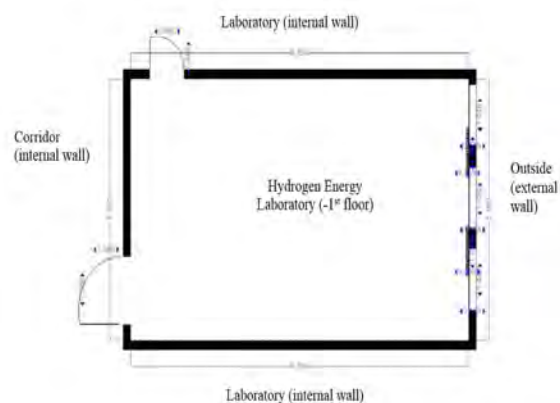


Figure 2. Hydrogen Energy Laboratory schematically representation with dimensions in meters

Table 3. Properties of Constructional Components

Constructional Component	Direction ^a	Thickness (m)	Length (m)	Width (m)	Number	Neighbor ambient temperature (°C)	Excluded area ²	Area to exclude (m ²)
External window (S_w)	NW	0.010	1.44	1.43	3	-12		
External Wall (E_w)	NW	0.300	2.85	5.16	1	-12	S_w	2.89
Inner door (I_{d1})	W	0.042	2.12	0.86	1	18		
Inner door (I_{d2})	S	0.042	2.31	1.38	1	18		
Internal Wall (I_{w1})	W	0.170	2.85	8.36	1	18	I_{d1}	2.2
Internal Wall (I_{w2})	S	0.210	2.85	5.16	1	18	I_{d2}	3.19
Internal Wall (I_{w3})	E	0.210	2.85	8.36	1	18		
Roof	SE	0.500	5.16	8.36	1	18		
Floor	NW	0.500	5.16	8.36	1	18		

The higher current densities and power values can be achieved by using lower cell voltages. However, when working with the HT-PEMFC system in low voltage regions, the water generated on the cathode side causes the acid leaching in the membrane and performance loss in long term operation.

In addition to this, although the membrane used in the LT-PEMFC system is different, the water formed on the cathode side of the cells is returned to the membrane and can cause the electrodes and the membrane to be drowned by water due to excessive moisture. When all of these is taken into consideration, it has been chosen as a 0.6 V operating voltage per cell in order to provide long term performance.

Design parameters and experimental results of low temperature and high temperature PEMFC systems can be seen in Table 4. Because of the property of the membrane used for low temperature PEMFC, air with 100% humidity is fed to the system. For high temperature PEMFC on the other hand, to prevent acid loss in the PBI membrane, and also because of the nature of high temperature, dried gases are fed to the system. Thermal power outputs for LT-PEMFC and HT-PEMFC systems are found to be 402 W and 456 W respectively.

Table 4. LT-PEMFC and HT-PEMFC design parameters

PEMFC Type	H_2 flow rate (slpm) ^a	Air flow rate V(slpm)	Gas humidifying ratio (%)	Thermal output (W)
LT-PEMFC	5.1	30.3	100	402
HT-PEMFC	6.7	30.3	0	456

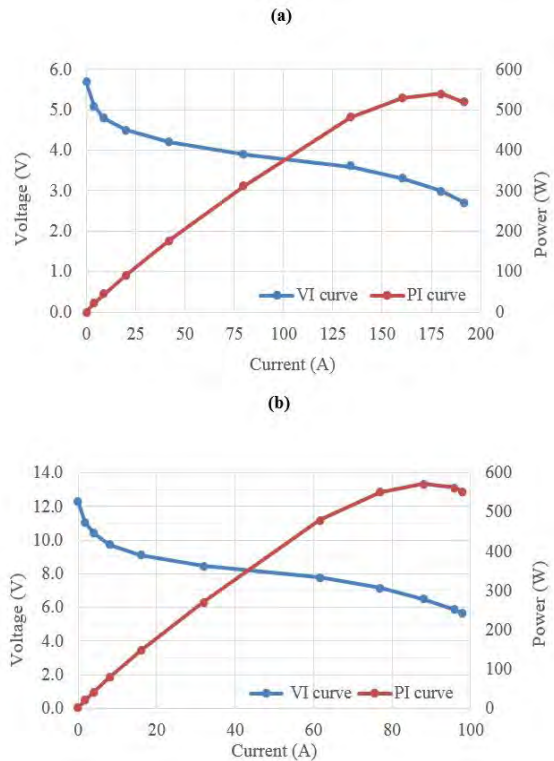


Figure 3. a) LT-PEMFC and b) HT-PEMFC systems performance curves

Micro-Cogeneration Application Results

For micro-cogeneration application of PEMFCs, as heat transfer fluid deionized water is used in LT-PEMFC system and heat transfer oil is used for cooling HT-PEMFC system.

In Table 5, physical properties, temperature differences and mass flow rates of cooling fluid and water can be seen for both systems. Because of high operation temperature

Table 5. Micro-cogeneration Application Results of PEMFC's

PEMFC Type	$C_{p,ss}$ (Kj/kg.°C)	ΔT^1 (°C)	\dot{m}_{ss} (kg/s)	η_{el}	η_{th}	η_{cogen}	ΔTw^2 (°C)	\dot{m}_W (kg/s)
LT-PEMFC	4.187	6	0.016	47.8	40	87.4	40	0.0022
HT-PEMFC	2.400	10	0.019	47.8	45	92.8	40	0.0025

¹ PEMFC cooling liquid inlet and exit temperature difference

² Heating water inlet and exit temperature difference for winter month average

Table 6. Thermal energy needed for heating the laboratory

Constructional Component		Heat Dissipation Calculation				Total heat requirement
Constructional Component	Width (cm)	Heat Dissipation ¹	Calculated area	Total heat transfer coefficient	Temperature difference	
		q_o (W)	A (m ²)	U (W/m ² K)	DT (°C)	q_h (W)
Location	B01	-	-	-1	-	Room Temperature: 22°C-
Sw	-	441	6.18	2.100	34	
Ew	-	216	1.82	0.538	34	
ld1	-	15	1.82	2.000	4	
ld2	-	26	3.19	2.000	4	
lw1	0.2	153	21.63	1.770	4	
lw2	0.2	82	11.52	1.770	4	
lw3	0.2	240	23.83	2.513	4	
Roof	0.5	22	43.14	0.128	4	
Floor	0.5	67	43.14	0.390	4	
TOTAL		1262	66.27			1578 ²

¹ Calculation of the amount of heat requirement of the laboratory not including direction, location, etc. ² Calculation of the amount of heat requirement of the laboratory including direction, location, etc.

of HT-PEMFC, to prevent heat loss, stack was insulated by glass wool of 1 cm thickness.

In Fig. 4, maximum water temperature-flowrate graphics of both PEMFC systems can be seen. In both systems, water is heated by means of a radiator (heat exchanger).

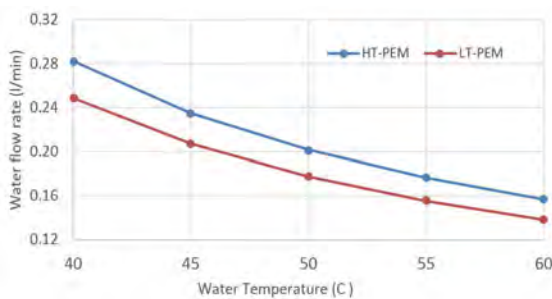


Figure 4. LT-PEMFC and HT-PEMFC cogeneration systems, water flowrate-water temperature graph

When examined, it can be concluded that for same temperature difference, HT-PEMFC system is capable of heating a higher amount of water per unit time.

Determination of Heating Load of the Laboratory

After all values are inputted to NZN software program, thermal energy needed for heating the laboratory is calculated and details can be seen in Table 6 below.

For heating the laboratory, necessary number of PEM fuel cells for HT-PEMFC system is calculates as 4 and total thermal power is determined as 1820 W. For LT-PEMFC cogeneration application, again a total of 4 cells are to be used but total thermal power is determined to be 1608 W. During the year, operational capacity of the systems can be arranged by changing the flow rate for cold months. In Table 7, maximum water temperature values for different flow rates are given for both systems.

Table 7. Flow rates required for water heating for both systems

LT-PEMFC			HT-PEMFC		
Water temperature (°C)	Water flow rate (kg/s)	Water flow rate (l/m)	Water temperature (°C)	Water flow rate (kg/s)	Water flow rate (l/m)
40	0.035	0.25	40	0.0039	0.28
45	0.0029	0.21	45	0.0033	0.24
50	0.0025	0.18	50	0.0028	0.20
55	0.0022	0.16	55	0.0025	0.18
60	0.0019	0.14	60	0.0022	0.16

Table 8. Simple pay back times for LT- PEMFC and HT -PEMFC systems.

PEMFC type	f_{hu}	SPT (year)	SPT_{exp} (year)
LT- PEMFC	0.596	3.3	2.4
HT-PEMFC	0.848	7	5.1

Pay Back Time Calculation Results

Simple pay back times for PEMFC systems and micro-cogeneration application of the systems are given in Table 8. Even though HT-PEMFC cogeneration system is more efficient, LT-PEMFC and its equipment are cheaper which makes this system more economical and advantageous with a SPT of 2.4 years.

RESULTS

In this study, effects of different operation temperatures on PEMFC system micro-cogeneration applications are examined. Firstly design of the LT-PEMFC and HT-PEMFC systems has been done and these systems have been experimentally tested. As heat transfer fluid deionized water is used in LT-PEMFC system and heat transfer oil is used for cooling HT-PEMFC system because of high oxidation durability.

LT-PEMFC and HT-PEMFC systems have 402 W and 456 W thermal powers respectively and by using this excess heat of the PEMFC systems simultaneously with electricity production, 87.4 % and 92.8 % total cogeneration efficiencies are calculated for LT-PEMFC and HT-PEMFC system respectively. For each system maximum water temperatures and flow rates are calculated as a result of micro-cogeneration application and HT-PEMFC system is found to be capable of higher amount of heating. Although LT-PEMFC system has a lower thermal power and efficiency, it is determined to be more economical and has a lower pay pack time then

HT-PEMFC system. For both systems, necessary number of cells to be used for laboratory heating is calculated as four and both systems are found technically convenient for micro-cogeneration applications.

ACKNOWLEDGEMENTS

This study was supported by The Scientific and Technological Research Council Of Turkey (TÜBİTAK) (1001 Project No: 214M301). We would also like to express our gratitude to TEKSİS Ltd. Şti. (METU-Tech) for their support during our studies.

SYMBOLS

A	Cell area [cm ²]
C_p	Specific heats [J/gK]
C_{fc}	Cost of fuel cell power system per kW of nominal power [\$/kW]
CF	Capacity factor
C_{el}	Cost of electricity [\$/kW]
C_{h2}	Cost of hydrogen [\$/kW]
C_{fuel}	Cost of natural gas [\$/kW]
\dot{E}	Enthalpy [J/s]
f_{hu}	Heat utilization factor
F	Faraday constant [96485 A.s/mol]
I	Current density [A/cm ²]
\dot{m}	Mass flow rate [g/s]
\dot{n}	Rates of consumed and generated gases [mol/s]
N_{cell}	Number of cell
Q	Heat dissipation [W]
P_{fc}	Fuel cell system nominal power [W]
r_{O2}	Oxygen volume in air
R_{th}	Thermal resistance K/W]
S	Stoichiometric ratio
T	Temperature [°C or K]
W_{net}	Net power [W]
η	Water heating efficiency
η_{el}	Electrical efficiency of fuel cell
η_{fc}	Average annual efficiency
η_{tot}	Total fuel cell efficiency
η_{heat}	Efficiency of conventional heat generation
AEP	Annual electric production
Δh	Low heating value of H2 gas
\dot{m}_{cl}	Mass flow rate of cooling liquid
\dot{m}_w	Mass flow rate of city water
$C_{p,cl}$	Specific heat of cooling liquid
$C_{p,w}$	Specific heat of city water
ΔT_{cl}	Inlet and outlet temperature difference of cooling liquid
ΔT_w	Inlet and outlet temperature difference of city water

REFERENCES

1. Devrim Y, Erkan S, Baç N, Eroğlu, I. Improvement of PEMFC performance with Nafion /inorganic nanocomposite membrane electrode assembly prepared by ultrasonic coating technique. *International Journal of Hydrogen Energy* 37(21) (2012) 16748-16758.
2. Barbir F. *PEM Fuel Cells: Theory and Practice*, second ed. Academic Press, New York, 2012
3. Araya SS, Zhou F, Liso V, Sahlin SL, Vang JR, Thomas S, Kær SK A Comprehensive Review of Pbi-Based High Temperature PEM Fuel Cells. *International Journal of Hydrogen Energy* 41(46) (2016) 21310-21344.
4. Gosselin D., A Stack Cost Comparison of 100 kW Combined Heat and Power Fuel Cell Systems, Department of Energy 2014, Website: <http://lma.berkeley.edu/research.html>, last access: 01.10.2017
5. Song T, Yi J, Kim J, Choi K. *Challenges and Opportunities of Thermal Management for High -Temperature Proton Exchange Membrane Fuel Cells*, 2010.
6. Alejandro J, Arce A, Bordons C. Development and experimental validation of a PEM fuel cell dynamic model. *Journal of power sources*, 173(1) (2007) 310-324.

Tree Shaped in Channels Parallel and Counter Flow Through Heat Exchanger Heat Transfer and Flow Investigation of Characteristic

A. Bugra COLAK, Isak KOTCIOGLU  Mansour NASIRI KHALAJI
Ataturk University, Department of Mechanical Engineering , Erzurum, TURKEY

ABSTRACT

In this study, a heat exchanger system capable of working on tree-shaped three-level parallel and counter flow basis was designed and manufactured based on the branched Fractal like flow channel structure. A similar phylum of heat exchanger on discs onto one surface of the lower and upper plates and both surfaces of middle plate, 156 Branched-micro channels with cylindrical sections were opened in three levels symmetrically with each other at different levels and diameters. According to the parallel and counter flow type based open circuit and closed circuit principle, the fluid enters the system at equal thermal capacity ratios from the axial or radial connection points and discharges. In the open circuit operating conditions, the heating water is in the temperature range of 35-45°C and the flow rate is 2,0-4,0 lt / min. Similarly, in the closed circuit operating conditions, the heating water is in temperature range of 45-60°C and the flow rate is 2,0-4,0 lt / min. During the experimental work, the temperature and hydrodynamic characteristics of the system are controlled through software written in the MATLAB R2013b package program. Experimental and numerical analyzes were carried out using ANSYS-Fluent ready packet programs. In the analysis, in the increasing flow rate, positions of some external and lateral channels are determined as cause of the decreasing in level of velocity. The result, requirement of designation as the bifurcation geometry divides the mass flow rate equally for each level of branching, is obtained. The results show that increase in level of branches is not important on the fluid channels which includes this kind (fractal) branch channel with tree-shaped. The results also show that, in the branched model heat exchanger, for opened and closed circuits, parallel flow (increasing branching levels, heating unit and cooling unit) is more efficient than the counter flow (increasing branching levels heating unit and decreasing branching level cooling unit) conditions.

Article History:

Received: 2018/02/28

Accepted: 2018/02/28

Online: 2018/09/07

Correspondence to: A. Bugra Colak,
ATATURK University, Faculty of Engineering,
Department of Mechanical Engineering,
Erzurum, TURKEY

Keywords:

Fractal Theory; Constructal Theory; MATLAB; ANSYS; Tree-Shaped Heat Exchanger; Parallel and Counter Flow; Branching Micro-Channel

INTRODUCTION

The cooling problem faced during use of electronic systems of industrial applications, which are designed in small size with high-performance and require high-technology, has gradually increased up to today.

Especially micro-channel heat sinks with high heat flux and an expanded surface, having an effective cooling mechanism, have gained importance. General cha-

racteristic of such heat sinks is to maximize the ability of heat rejection by minimizing volume and mass of the expanded surfaces. For higher heat transfer coefficients and minimum volume, a large surface area per unit volume provides an advantage in such channel geometries. The literature has various studies on thermal and hydrodynamic behaviours of micro-channels used as a cooling system.

A great number of scientific studies on micro-channel heat sinks have been carried out by researchers such as Tuckerman and Pease (1981), Vafai and Lu (1999), Peterson (1999), Stief et al. (1999), Chong et al. (2002), Lee et al. (2008), Moreno et al. (2015), Yang et al. (2014), Hernando et al. (2009), Bier et al. (1993). These researchers carried out thermal and flow analyses with heat exchangers designed in different geometries and with different flows in their studies. They examined optimization of single and double layered counter-flow micro-channel heat sink, and attempted to determine the optimum design parameters by carrying out thermal performance and temperature distribution analyses for micro-channel types that they have designed.

FRactal AND CONSTRUCTAL THEORY

In the cooling technology, the systems called *fractal channel network*, which is a symmetrical geometric structure that appears similar to itself at an infinitely little ratio and has major physical and mathematical characteristics of a non-uniform and fractured flow environment at the largest and smallest scale, have gained importance in theoretical and experimental studies in terms of applied engineering.

Fractal-like channel network is a new structure that can be assimilated to many geometric forms in the nature with its decreasing diameters from large to small. The purpose here is to obtain an appropriate surface temperature distribution without increasing the pressure drop. In the literature, the study regarding two-phase flows in the channel structures developed as similar to above mentioned structures was carried out by Daniels et al (2005).

As similar to such structures, channels known as constructal structures were also developed for the same purposes. Constructal theory is a physics law which summarizes a phenomenon existing in engineering and the nature. To express more clearly, constructal structure is a complex structure consisting of a large number of elements, and the theory defining this structure is called constructal theory. This theory is based on behaviour of various structures and forms in the nature, which are produced to obtain an optimum performance.

In the literature, most of the studies conducted on this subject are theoretical and number of experimental studies is quite low. With regard to thermodynamic optimization theory of such flow systems; researchers such as Bejan (1996, 1997, 2002, 2007), Wechsato et al. (2002); Bonjour et al. (2003); Silva et al. (2004), Murray (1926) and Cohn (1954), Lee and Lin (1995, 1997), Lorenzini and Rocha (2006), Xia et al. (2015), Chen and Cheng (2002), Chen and Cheng (2005), Silva and Bejan (2006), Zimparov et al. (2006), Xu et

al. (2006), Kwak et al. (2009), Chen et al. (2010), Heymann et al. (2010), Zhang et al. (2013), Salakij et al. (2013), Xu et al. (2015), Escher et al. (2009), Ghodoossi (2005), Andhare et al. (2016), Hong et al. (2007), Meyer et al. (2005), Kim et al. (2014), Kuen Tae Park et al. (2014) etc. developed models in their studies for estimation of pressure drops and surface temperatures in fractal-like flow channels as well as diameters and lengths of the channels. They analytically and numerically studied thermal performance of a dendritic *constructal* heat exchanger with small-scale crossflows and larger-scale counter flows.

In their studies, they compared dendritically designed fins of Y-type, T-type and H-type and numerically performed their optimal solutions that minimize their thermal resistances and increase their optimal performances. Dendritic branching-channel heat exchangers are more advantageous in terms of pressure drop when compared to other types of heat exchangers. They can also be manufactured in very small sizes, which is quite important in terms of their usability for advanced technologies such as MEMS.

In this study, a heat exchanger comprised of 3 discs with engraved branch-like cylindrical section channels was designed and manufactured, and thermal and hydrodynamic behaviours of the heat exchanger were experimentally and numerically examined by means of a test mechanism. They conducted an experimental study where pressure drop and flow energy were minimized in the test system. In addition to the experimental study; temperature, rate and pressure distributions were numerically researched through ANSYS packaged software.

MATERIALS AND METHOD

Test System

In this study, schematic drawing of the test mechanism for dendritic branching-channel heat exchanger is given in Fig. 1. The test zone of the test mechanism for the dendritic branching-channel heat exchanger is comprised of two heating units, two circulation pumps, cross flow cooling radiators, a switchboard, a computer communication unit and measuring equipment. Assembly drawing of the test mechanism equipment is shown in Figure 5. Heating and cooling sides of the dendritic branching-channel heat exchanger, which are main components of the experiment system, have been designed and manufactured to be operated with water.

Since the thermal efficiency is higher, the lower branched plate was used for heating process, while the upper branched plate was used for cooling process. The experiment system was so designed that the heating side can be

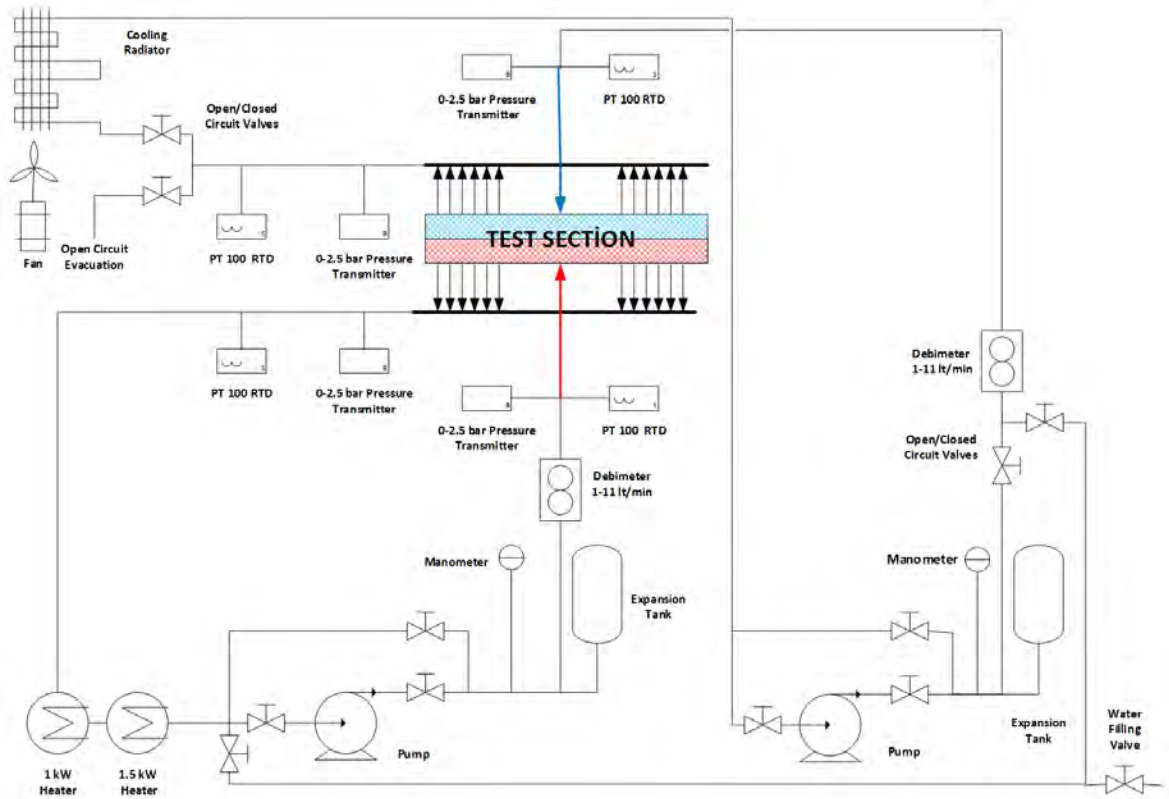


Figure 1. Schematic drawing of the test system

operated as closed circuit and the cooling side can be operated as both closed and open circuits, and tests were performed.

Schematic drawings for closed and open circuit operations are given in Fig. 2 and 3. In order to enable fluid circulation in heating and cooling units, two circulation pumps with the same power was used one for each fluid circuit.

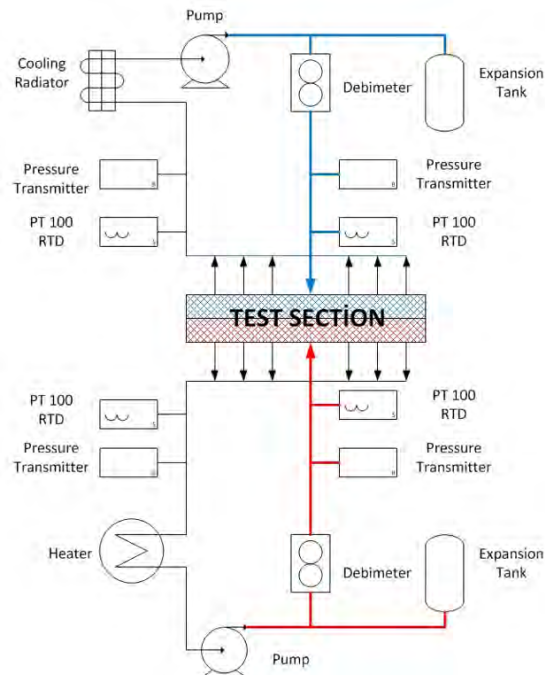


Figure 2. Closed circuit operation of the test system

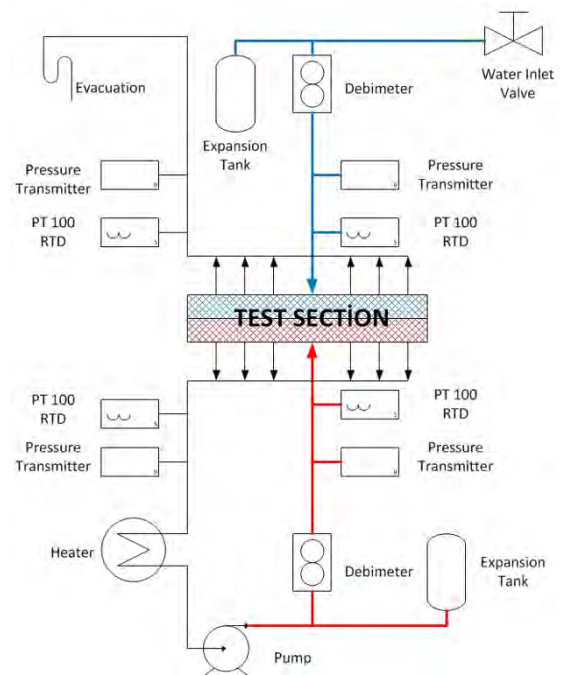


Figure 3. Open circuit operation of the test system

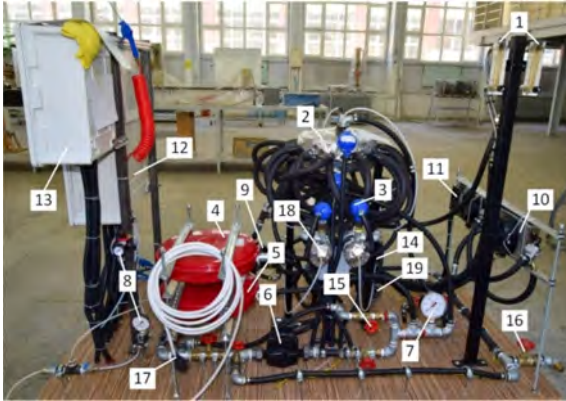


Figure 4. Components of the test system; (1) Flowmeter (2) Test Zone (3) PT100 Temperature Transmitter (4) Expansion Tank (Heating Side) (5) Expansion Tank (Cooling Side) (6,19) Circulation Pump (7) Hydro-meter (8) Pressure Gauge (9) Heating Tank (10) Cooling Radiator (11) Cooling Fan (12) Switchboard (13) Electronic System Panel (14) Pressure Transmitter (15) Bypass Valve (16) Filling Valve (17) Power Connection (18) Collector

Both circuits were set with float flowmeters to measure the amount of the fluid. In addition, 2 sleeve-type resistance heaters were used in order to heat the fluid used in the heating side.

It has two electrically operated heaters, each of which is situated into an individual small-volume tank, with the power of 1 kW and 1.5 kW; and the fluid is transmitted into the system after consecutively passing through these two heaters.

The heaters were not controlled by a separate thermostat; instead, they were precisely set through MATLAB software, which allows operation of the test system and receiving the test data, and controlled through contactor groups. The experiment system was controlled and stabilized beforehand through the pre-heating software prepared in MATLAB software package, and tests were started after pre-heating process.

Heat Transfer Process

In this study, the fluid in the heating side (hot water) circulates through the test system on a closed circuit basis and the fluid in the cooling side (cold water) circulates through the system on both open circuit and closed circuit bases. Under the closed circuit operating conditions, the fluid exiting from the test zone as heated is cooled by the radiators, then pressurized by the circulation pump and returned to the test zone. Under the open circuit conditions, the fluid entering the cooling unit is taken from the mains system, and pressure of the mains is used for circulation in the system. The heated fluid exiting from the test zone leaves the system after its temperature is measured. Heat transfer values of the fluids entering into and exiting from the heating and cooling sides du-

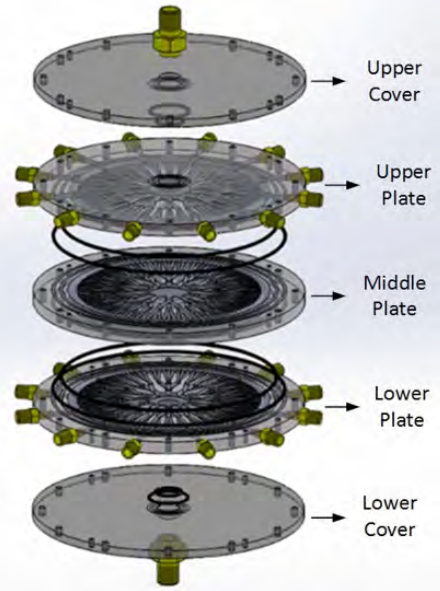


Figure 5. Test zone of the test system

ring the tests were individually calculated. In calculation, heat transfer values for entry and exit are averaged and the following equation is used,

$$Q_{mean} = \frac{Q_g + Q_r}{2} \quad (1)$$

In this equation, Q_g is the heat transfer value for entry into the system and Q_r is the heat transfer value for exit from the system. Heat balance of the system is given with the equation below.

$$Q_{top} = Q_{transm} + Q_{con} + Q_{rad.} + Q_{losses} \quad (2)$$

The heat loss in the test zone due to radiation is about 5% of the heat received from the fluid entering into the dendritic branching-channel heat exchanger. Since this value can be omitted when compared to the heat transfer value at the fluid inlet, and the equation is rearranged as below;

$$Q_{top} = Q_{transm} + Q_{con} + Q_{losses} \quad (3)$$

The heat transfer to the system due to the hot fluid passing through between the lower and middle plates is calculated with the following equation.

$$Q_g = \dot{m}_h C_p (T_1 - T_2) \quad (4)$$

In this equation, T_1 temperature is the inlet temperature of the hot fluid entering into the dendritic branching-channel heat exchanger. T_2 temperature is the outlet temperature of the hot fluid exiting from the collector. The heat transfer from the system due to the cold fluid passing through between the upper and middle plates is calculated with the following equation.

$$Q_r = \dot{m}_c C_p (T_4 - T_3) \tag{5}$$

In this equation, T_3 temperature is the inlet temperature of the cold fluid entering into the heat exchanger. T_4 temperature is the outlet temperature of the cold fluid exiting from the collector. Similarly, the heat loss can be calculated as below,

$$Q_{\% \text{ thermal difference}} = \left(1 - \left(\frac{Q_r}{Q_g} \right) \right) \times 100 \tag{6}$$

R.S. Andhare et al. (2016) stated that this thermal difference can be at 10% level; and this ratio was calculated in our studies and given as a diagram in Fig. 17.

Reynolds (Re) Prandtl (Pr) and Nusselt (Nu) Numbers

In calculation of the flow and the heat transfer, the flow inside a cylindrical section pipe and relevant pure numbers are given with the equations below.

$$Re = \frac{\rho V D_h}{\mu} \tag{7}$$

Prandtl number, which is the ratio of momentum diffusion to thermal diffusion in the thermal and hydrodynamic boundary layers, was calculated with the following equation;

$$Pr = \frac{\nu}{\alpha} = \frac{c_p \mu}{k} \tag{8}$$

In this equation, (ν) is kinematic viscosity, (α) is thermal diffusivity, (c_p) specific heat, and (μ) is dynamic viscosity. Separate Nusselt numbers for fully developed and developing flows are given in the following equation, for a cylindrical section pipe with a diameter of D_h , according to (h) heat transfer coefficient and k heat convection coefficient.

$$Nu = \frac{h D_h}{k} \tag{9}$$

In the dendritic branching-channel heat exchanger test mechanism, thermally and hydrodynamically developing laminar flow conditions have been applied to the flow in the heat exchanger up to a flow rate of 4.0 l/min at branching level 0. Thermally and hydrodynamically developing flow conditions have been applied to all ranges of flow rate at branching levels 1 and 2.

Nusselt correlations required for this study depending on the Reynolds number, the flow regime and the thermal conditions are given below.

Branching and Branch Levels Measurement Details

Design specifics of the dendritic branching-channel heat exchanger are given in Fig. 6. In this type of heat exchan-

gers; N number of branching means number of the branches to be developed by the current channel at the next level, and k branching level means the number of branching points starting from the fluid inlet. For the heat exchanger modelled in this study, $N=3$ and $k=2$, i.e. $k=0, k=1, k=2$. As it is seen in Figure 6, D_0, D_1 and D_2 and L_0, L_1 and L_2 indicate channel diameters and lengths for three different levels from level zero to level two, respectively. As it is shown in Fig. 8; starting from the inlet point, the fluid splits into 12 branches at level 0, and then it splits again into 3 at level 1 thus creating 36 branches. At level 3, the

Table 1. Nu number correlations for developing flows (Stephan,Preusser)

Reynolds Number	Flow Regime	Thermal Conditions
$Re < 2300$	Thermally and Hydrodynamically Developing Flow	Constant heat flux
		$Nu = 4.364 + \frac{0,086 \left(\frac{RePrD}{L} \right)^{1.33}}{1 + 0.1Pr \left(\frac{ReD}{L} \right)^{0.83}}$
$Re < 2300$	Thermally and Hydrodynamically Developing Flow	Constant Surface Temperature
		$Nu = 3.657 + \frac{0,0677 \left(\frac{RePrD}{L} \right)^{1.33}}{1 + 0.1Pr \left(\frac{ReD}{L} \right)^{0.3}}$

fluid splits into 3 again, thus creating 108 branches. The fluid arrives the collecting channel after branching level 2 and leaves the heat exchanger by passing through the 12 discharge points located there.

Technical details of the plates of the dendritic branching-channel heat exchanger are given in Fig. 6, Fig. 7 and Fig. 8. On the plate, there are 12 branches at level 0, 36 branches at level 1 and 108 branches at level 2. The symmetrical branching spreading on the disc-shaped plate is produced from aluminum material according to the technical details thereof given in Table 2.

Total area of the branching spreading on the heat exchanger at level N is calculated separately for each level with the following equation.

$$A_k = \pi \times N_k \times D_{h,k} \times L_k \tag{10}$$

$N_k = 12(3^k)$ In this equation, (N_k) is the number of the branches at level k , and $D_{h,k}$ is hydraulic diameter of the branch at level (L_k), is the length of the branch at level k . According to the equation 10, relevant areas at level 0, level 1

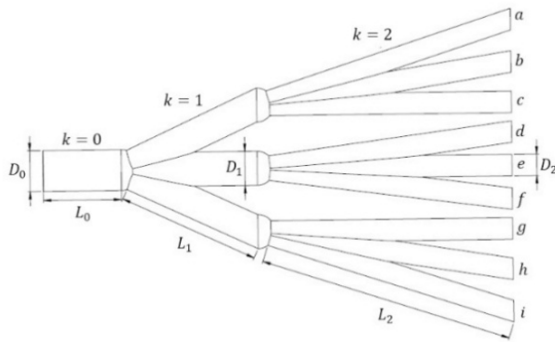


Figure 6. Branching details of the dendritic branching-channel heat exchanger

and level 2 are $A_0=2,601 \times 10^{(-3)} \text{m}^2$, $A_1=0,0113 \text{m}^2$, $A_2=0,04033 \text{m}^2$, respectively. Total area is calculated as $A_{top}=A_0+A_1+A_2=0,05423 \text{m}^2$.

Total Heat Transfer Coefficient (U)

Heat is transferred from resistances between fluid-wall-fluid due to $(T_h - T_c)$ temperature differences. When equal surface areas are considered, total heat transfer coefficient (U) is obtained with the following equation,

$$\frac{1}{U} = \frac{1}{h_h} + \frac{t}{k} + \frac{1}{h_c} \tag{11}$$

U is total heat transfer coefficient, $1/h$ is convection resistances, and t/k is transfer resistance. Heat transfer values were calculated separately on the basis of mass flows, inlet and outlet temperatures and thermal capacities of both fluids. Heat transfer from hot fluids is found by using the equation below,

$$Q_h = \dot{m}_h c_p (T_{h,i} - T_{h,o}) \tag{12}$$

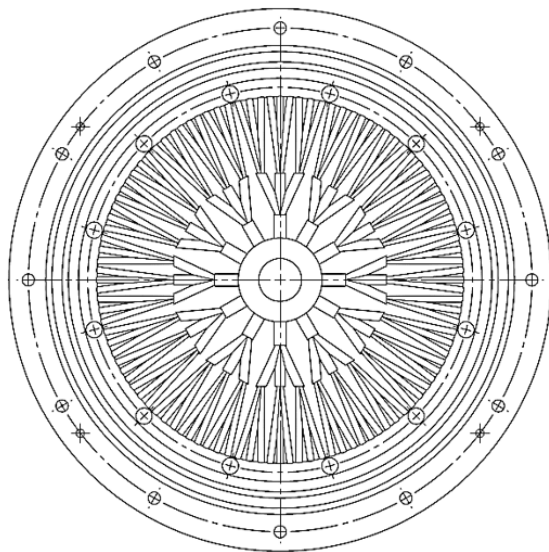


Figure 7. Upper and lower plate details of the dendritic branching-channel heat exchanger

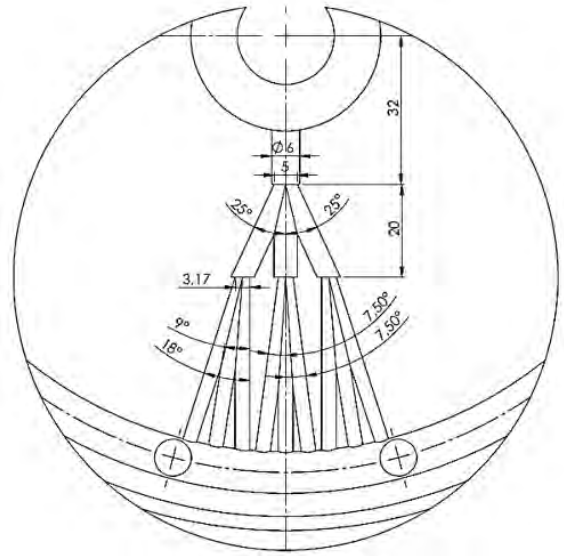


Figure 8. Technical drawing of branching details of the dendritic branching-channel heat exchanger

Similarly, heat transfer to cold fluid is calculated by using the following equation,

$$Q_c = \dot{m}_c c_p (T_{c,i} - T_{c,o}) \tag{13}$$

Coefficient for total heat transfer between the hot fluid and the inner surface of the plate is found through the equation below,

$$U = \frac{Q_h}{A_{top} \frac{(T_{h,i} - T_{c,i}) - (T_{h,o} - T_{c,o})}{\ln \frac{(T_{h,i} - T_{c,i})}{(T_{h,o} - T_{c,o})}}} \tag{14}$$

In these equations, Q_h is heat transfer from the hot fluid, $T_{h,i}$ is temperature of the hot fluid entering into the heating side of the heat exchanger, $T_{h,o}$ is temperature of the cooled fluid exiting from the heating side of the heat exchanger, $T_{c,i}$ is temperature of the fluid entering into the cooling side of the heat exchanger, $T_{c,o}$ is temperature of the heated fluid exiting from the cooling side of the heat exchanger, and A_{top} is total surface area of the branching spreading on the heat exchanger.

Log Mean Temperature Difference (LMTD)

In the thermal analysis of the heat exchanger, the Log Mean Temperature Difference (LMTD) method and the

Table 2. Geometric properties of the fractal channels

Branching Level	Number of the Channels in a Branch	Hydraulic Diameter	Branch Length
k	N_k	$D_{h,k} \text{ (mm)}$	$L_k \text{ (mm)}$
0	12	6.00	11.50
1	36	5.00	20.00
2	108	3.17	37.50

ε - NTU method were used. In the log mean temperature difference method, heat transfer value of the heat exchanger is calculated with the equation given below.

$$\dot{Q} = UA\Delta T_{lm} \quad (15)$$

Log mean temperature difference in the equation above is given with the following equation,

$$\Delta T_{lm} = \frac{\Delta T_1 - \Delta T_2}{\ln\left(\frac{\Delta T_1}{\Delta T_2}\right)} = \frac{(T_{h,i} - T_{c,i}) - (T_{h,o} - T_{c,o})}{\ln\left(\frac{T_{h,i} - T_{c,i}}{T_{h,o} - T_{c,o}}\right)} \quad (16)$$

For log mean temperature difference in a parallel flow heat exchanger, ΔT_1 and ΔT_2 temperature differences at inlet and outlet points are calculated as below,

$$\Delta T_1 = T_{h,i} - T_{c,i} \quad (17) \quad \text{and} \quad \Delta T_2 = T_{h,o} - T_{c,o} \quad (18)$$

In these equations, $T_{h,i}$ is inlet temperature of the hot fluid entering into the heat exchanger, $T_{c,i}$ is inlet temperature of the cold fluid entering into the heat exchanger, $T_{h,o}$ is outlet temperature of the hot fluid exiting from the heat exchanger, and $T_{c,o}$ is outlet temperature of the cold fluid exiting from the heat exchanger.

For log mean temperature difference in a counter-flow heat exchanger, ΔT_1 and ΔT_2 temperature differences at inlet and outlet points are calculated as below,

$$\Delta T_1 = T_{h,i} - T_{c,o} \quad (19) \quad \text{and} \quad \Delta T_2 = T_{h,o} - T_{c,i} \quad (20)$$

At the same inlet and outlet temperatures of the heat exchanger, log mean temperature difference was found higher in case of counter-flow when compared to parallel flow.

ε - NTU Method

Before defining effectiveness for a heat exchanger, the maximum possible heat transfer value Q_{max} should be calculated for that heat exchanger. In such case, $(T_{h,i} - T_{c,o})$ maximum heat transfer will occur due to the maximum difference of temperature obtained between the fluids in the heat exchanger.

For this, the thermal capacity flow rate $C_c = \dot{m}_c c_p$, of the cold fluid must be lower than the thermal capacity flow rate $C_h = \dot{m}_h c_p$ of the hot fluid ($C_c < C_h$). In this case, it would be $|dT_c| > |dT_h|$. For $r, L \rightarrow \infty$, outlet temperature of the cold fluid can rise up to inlet temperature of the hot fluid where $C_c < C_h$ and $T_{c,o} = T_{h,i}$, Q_{max} is obtained with the equation below,

$$Q_{max} = C_c (T_{h,i} - T_{c,i}) \quad (21)$$

Similarly, if $C_h < C_c$, a bigger exchange of heat would occur in the hot fluid and it can get cooled down to the inlet temperature of the cold fluid. Where $C_h < C_c$ and $T_{h,o} = T_{c,i}$, Q_{max} is given in the following equation.

$$Q_{max} = C_h (T_{h,i} - T_{c,i}) \quad (22)$$

In these two cases, Q_{max} heat transfer value is given according to the minimum heat capacity C_{min} in the equation below.

$$Q_{max} = C_{min} (T_{h,i} - T_{c,i}) \quad (23)$$

In this equation, C_{min} thermal capacity flow rate is accepted equal to the lower one of C_c or C_h values. In a heat exchanger, the ratio of the actual heat transfer Q value to the maximum possible heat transfer Q_{max} value is defined as ε effectiveness, and presented with the following equation.

$$\varepsilon = \frac{Q}{Q_{max}} \quad (24)$$

Effectiveness ε can also be calculated on the basis of temperature difference and thermal capacities through the equation below.

$$\varepsilon = \frac{C_h (T_{h,i} - T_{h,o})}{C_{min} (T_{h,i} - T_{c,i})} \quad (25)$$

In this relation, C_{min}/C_{max} ratio can take C_c/C_h or C_h/C_c value, depending on thermal capacity flow rates of the hot and cold fluids. NTU Number of Transfer Unit is equal to the ratio of total heat transfer coefficient and heat transfer surface area to the minimum thermal capacity, and given with the following equation.

$$NTU = \frac{UA}{C_{min}} \quad (26)$$

Effectiveness- NTU Relations

$C_{min} = C_h$ let a parallel flow heat exchanger with is considered. If the effectiveness value ε for a parallel flow heat exchanger is found;

$$\varepsilon = \frac{1 - \exp\{-NTU [1 + (C_{min} / C_{max})]\}}{1 + (C_{min} / C_{max})} \quad (27)$$

$C_{min} = C_c$ since the same result is obtained for; regardless of whether the minimum thermal capacity flow rate of fluid belongs to the hot fluid or the cold fluid, this relation can be applied to any parallel flow heat exchanger. When $C_c < 1$, the effectiveness value for counterflow operating conditions is given with the equation below,

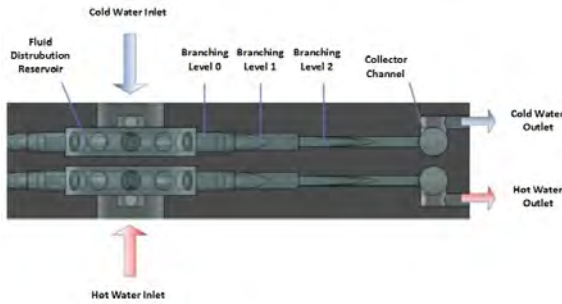


Figure 9. Sectional view of parallel flow operation of the dendritic branching-channel heat exchanger

$$\varepsilon = \frac{1 - \exp\{-NTU(1 - C_r)\}}{1 - C_r \exp\{-NTU(1 - C_r)\}} \quad (28)$$

In case that $C_r=1$, effectiveness value is given with the following equation,

$$\varepsilon = \frac{NTU}{1 + NTU} \quad (29)$$

In this study, tests were conducted by assuming that flow rates of both fluids are equal; and thermal capacity flow rates of both fluids are equal ($C_{min}=C_{max}$).

RESULTS

Thermal Transfer Analysis

In this study, while thermal capacity flow rates of the designed dendritic branching-channel heat exchanger at its upper-middle and lower-middle plates were kept equal, operation at similar fluid inlet temperatures (closed circuit) and operation at distinct fluid inlet temperatures (open circuit) were studied. Performances of parallel flow and counter-flow configurations were compared. In Fig. 9 and Fig. 10, representative sectional views of the heat exchanger in cases of parallel flow and counter-flow are given. Findings obtained from the tests conducted under operating conditions of the parallel flow closed circuit are given as a diagram in Fig. 11. In this diagram, change of the heat transfer value (Q) by the volumetric flow rate (\dot{V}) at different temperatures in case of the parallel flow closed circuit is presented. It is observed that the heat transfer value increases at the same ratio with each increase of temperature. For the values lower than 4 liter/minute volumetric flow rate, laminar flow conditions apply at branching levels 0, 1 and 2 of the dendritic branching-channel heat exchanger.

For the volumetric flow rate values over 4 liter/minute, it was seen in the calculations that the turbulent flow conditions applies at level 0. When the inlet water temperature ($T_{h,i}$) rises over 60°C, turbulent flow conditions occur in branches at levels 0 and 1 at a volumetric flow rate of 9,0 li-

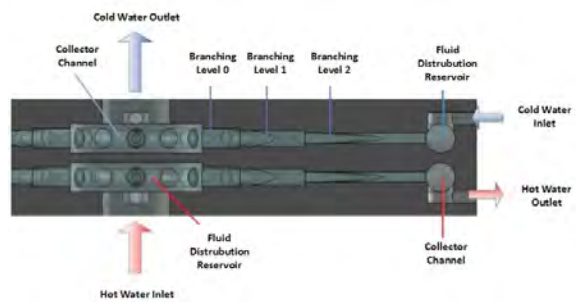


Figure 10. Sectional view of counter-flow operation of the dendritic branching-channel heat exchanger

ter/minute.

When change of the heat transfer values and the volumetric flow rates are compared between the parallel flow closed circuit given in Fig. 11 and the counter-flow closed circuit given in Fig. 12, it is seen that the heat transfer value is higher for the parallel flow at the same volumetric flow rate. Flow conditions occurring toward increasing branching levels also increase the amount of the transferred heat while increasing pressure losses. In the computer-aided study carried out under this research, it was seen that the outlet temperature values obtained for both sides as a result of the analyses performed through ANSYS-Fluent software package were approximately equal to the outlet temperature value of the fluid exiting from the system in the tests.

In the diagrams in Fig. 13 and Fig. 14, changes of the heat transfer values of the parallel flow and counter-flow open circuits respectively by the volumetric flow rate of the fluid are separately presented. In these diagrams, it is seen that the parallel flow open circuit is more effective than the counterflow.

In the diagram in Fig. 15, the ratio of the heat transfer value to the inflowing heat value at the same temperature and flow rate values (45°C, 2.0-4.0 l/min) for the tests conducted in closed and open circuits is presented. Under the same conditions, this ratio is higher for the open circuit.

$$Q_{\% \text{ thermal difference}} = \left(1 - \left(\frac{Q_r}{Q_g} \right) \right) \times 100 \quad (30)$$

Pressure Losses

In order to find the pressure losses for increasing and decreasing levels of branching of the dendritic branching-channel heat exchanger, pressure losses were measured at flow rates between 2.0-9.0 l/min. For measuring purpose, pressure transmitters situated at fluid inlet and collector outlet points of the dendritic branching-channel heat exchanger were used.

As it is seen in Fig. 16, Reynolds number in the heat ex-

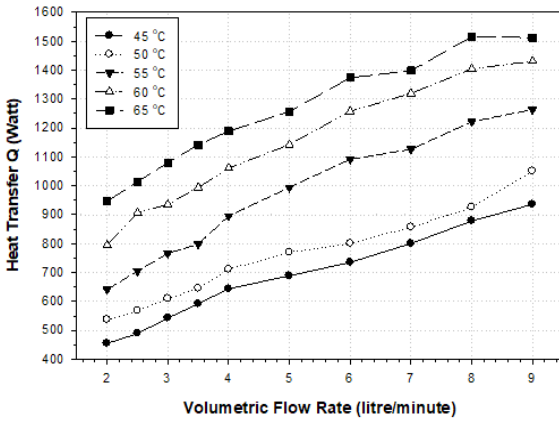


Figure 11. Change of the heat transfer value by the volumetric flow rate in the parallel flow closed circuit

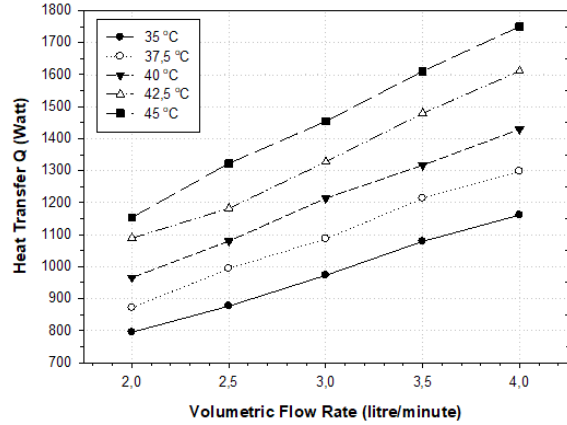


Figure 14. Change of the heat transfer value by the volumetric flow rate in the counterflow open circuit

hanger consisted of cylindrical section branching increased by increasing volumetric flow rate, and it caused an increase

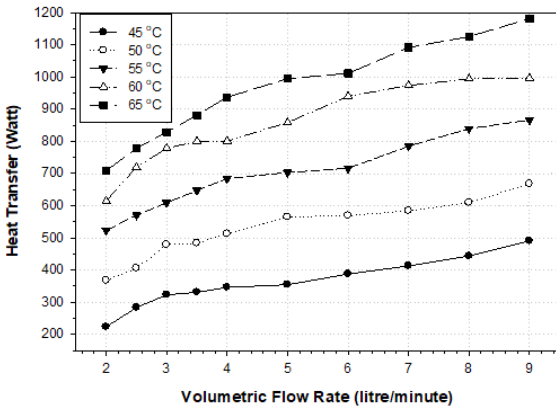


Figure 12. Change of the heat transfer value by the volumetric flow rate in the counterflow closed circuit

laminar flow to transient region occurs for branching level 0.

As it is seen in the diagram, the pressure losses towards increasing branching levels are higher than those towards decreasing branching levels in case of the laminar flow. It is seen that a transient flow occurs after 4.0 l/min value at branching level 0 and the pressure and its losses are almost equal for the flows toward both ways. At other branching levels, the flow is laminar for both flow conditions. At branching levels 1 and 2, the flow rate decreased further. This result indicates that further branching is not important in the flow channels with such dendritic branching (fractal) channel structure. This situation shows that, in terms of shedding light on the limited number of studies carried out on this subject, and experimental result in this study is consistent with the theoretical and experimental results in the literature.

also in the pressure losses. The flow is laminar at the flow rates below 4.0 l/min at all branching levels. In the laminar flow region, Reynolds numbers range between 200-1950. After the volumetric flow rate of 4.0 l/min, a transition from

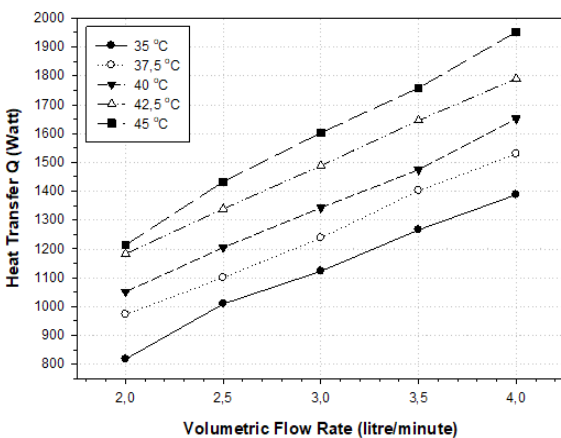


Figure 13. Change of the heat transfer value by the volumetric flow rate in the parallel flow open circuit

Log Mean Temperature Differences

In order to be able to experimentally calculate the total heat transfer coefficient (U) in a heat exchanger, the log mean temperature (ΔT_{LM}) difference method is used. In the experiments carried out for the dendritic branching-

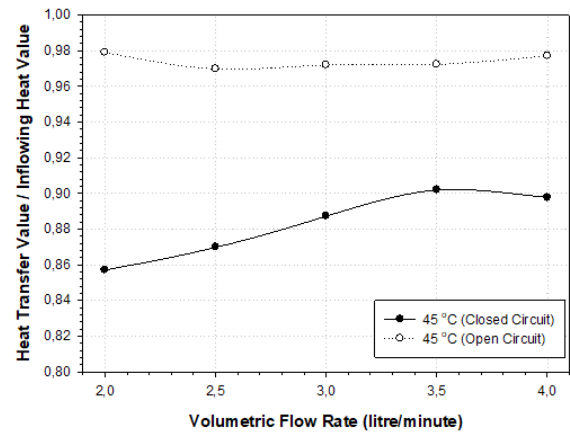


Figure 15. Change of the ratio of the heat transfer value / inflowing heat value by the volumetric flow rate in cases of closed and open circuits

channel heat exchanger, changes between the volumetric flow rates and the log mean temperature differences for different operating conditions and different situations are separately presented in the diagrams in Fig. 17-20. When Fig. 17 and Fig. 18 are compared, the log mean temperature difference is higher in the parallel flow closed circuit when compared to the counter-flow closed circuit.

Change of Nusselt-Reynolds Numbers

The change of the Nusselt numbers calculated for the heating and cooling sides at a maximum heating water inlet temperature of 65°C under the operating conditions of the parallel flow closed circuit by the Reynolds number is given in Fig. 21. According to the Nu relation given above, change of the Nusselt numbers for laminar flow at level 1 and 2 of the dendritic branching-channel heat exchanger by the Reynolds number under the operating conditions of parallel flow closed circuit was calculated. Change of

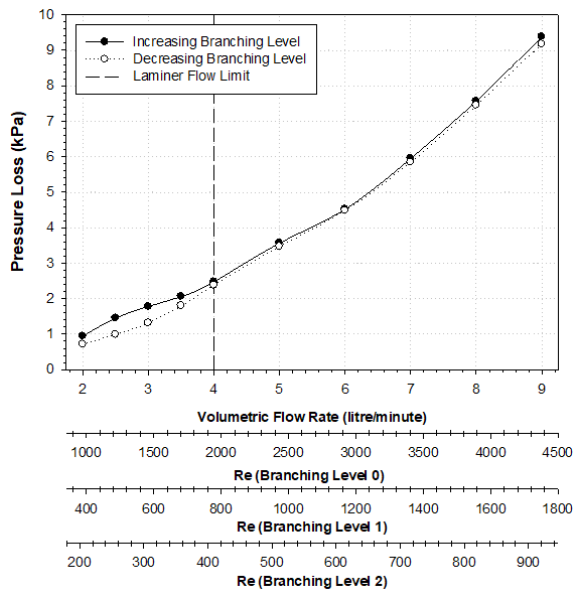


Figure 16. Change of the pressure losses towards increasing and decreasing branching levels by the volumetric flow rate and the Reynolds number in the branches

the Nusselt number and the Reynolds numbers at level 0 is not shown in the diagram because the flow becomes turbulent flow for the values over 4.0 l/min.

In Fig. 22, Change of the Nusselt numbers calculated for the heating and cooling units at a maximum heating water inlet temperature of 65°C under the operating conditions of the counter-flow closed circuit by the Reynolds number is given. As it is seen in all of the three diagrams, the Nusselt numbers increased as the Reynolds number increased.

Change of Total Heat Transfer Coefficient (U)

In the dendritic branching-channel heat exchanger, flow in each channel thermally and hydrodynamically re-develops at each branching level, and the boundary layer reforms again for each level. Channel lengths being too short which do not allow the flow to fully develop thermally and hydrodynamically, and this causes an increase in h heat convection coefficient thus causing an increase in the total heat transfer coefficient.

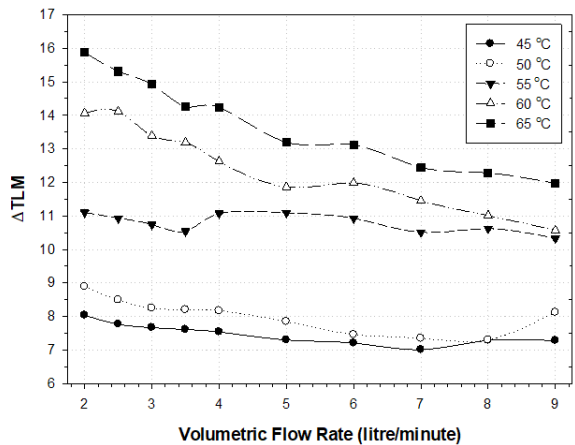


Figure 17. Change of the log mean temperature difference by the volumetric flow rate between the heating and cooling units in the parallel flow closed circuit

In Fig. 23-26, change of the total heat transfer coefficient U ($W/m^2.K$) by the volumetric flow rate (\dot{V}) for the parallel flow and counterflow operating conditions in open and closed circuits. It is seen in the diagrams given for the parallel flow and counterflow operations in the closed circuit that as the volumetric flow rate increases, the total heat transfer coefficient increases as well. Geometry of the dendritic branching-channel heat exchanger, increasing plate section towards increasing branching level, further occur-

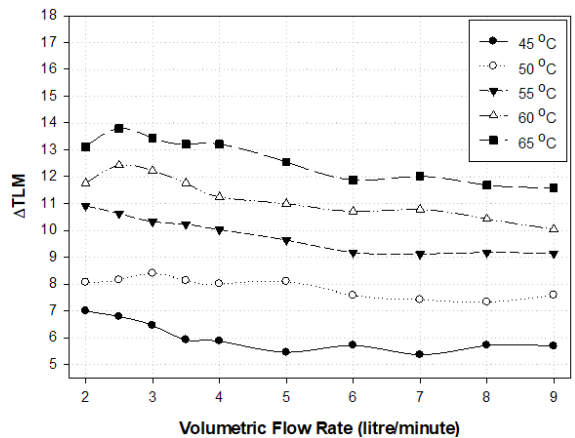


Figure 18. Change of the log mean temperature difference by the volumetric flow rate between the heating and cooling sides in the counter-flow closed circuit

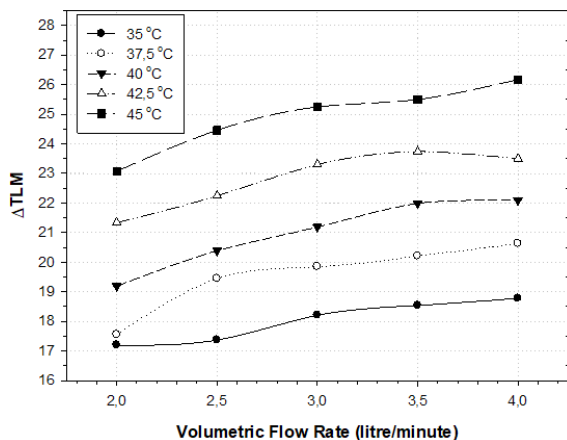


Figure 19. Change of the log mean temperature difference by the volumetric flow rate in the parallel flow closed circuit

rence of swirling flows, and also occurrence of jet flow at both points under the parallel flow conditions at the point where the distribution reservoirs are located cause the heat transfer coefficient to be found higher in case of parallel flow.

It is seen in the diagrams that the total heat transfer coefficient takes similar values depending on the temperature at a heating water inlet temperature of 45°C and a volumetric flow rate ranging between 2.0-4.0 l/min under the same operating conditions of the open circuit and closed circuit during the tests. Likewise, it is seen as a result of the tests that the most effective variable for change of the total heat transfer coefficient is the volumetric flow rate and the

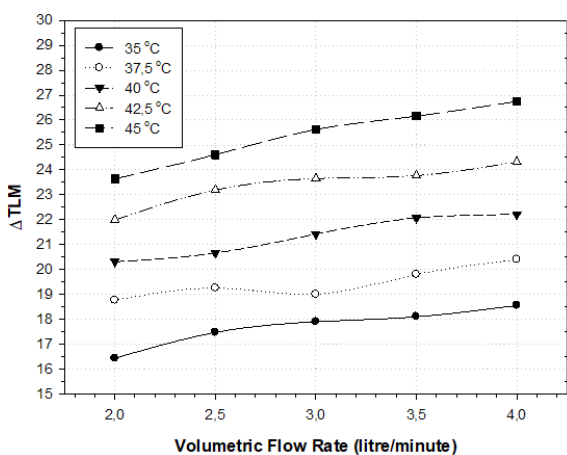
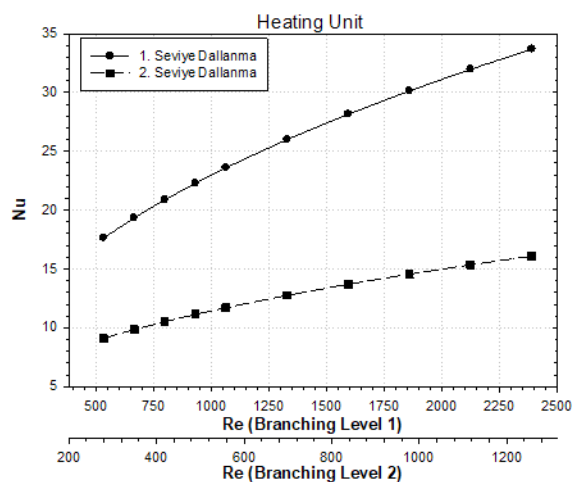
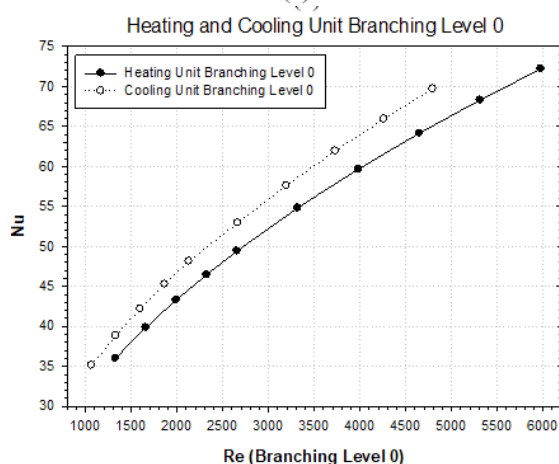


Figure 20. Change of the log mean temperature difference by the volumetric flow rate in the counter-flow open circuit

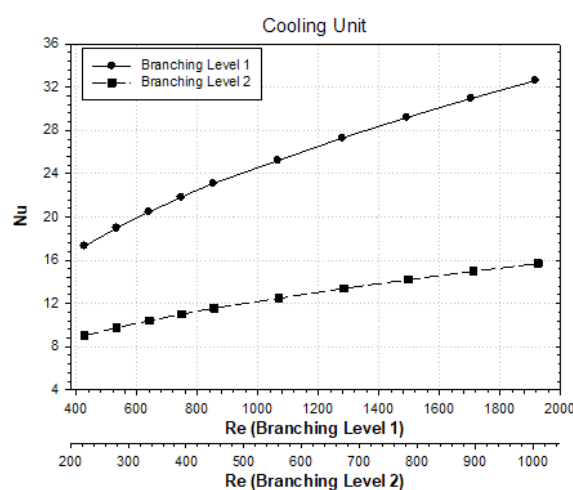
temperature range does not have a significant impact. It is a known fact that changing the inlet temperature of the heating unit of the heat exchanger would cause a change in the physical characteristics of the heating fluid. However, as a result of the test data it is not as effective as the volumetric flow rate value. It can be said according to the following four



(a)



(b)



(c)

Figure 21. Change of the Nu-Re numbers at an inlet temperature of 65°C for the operating conditions of the parallel flow closed circuit

diagrams that the highest total heat transfer coefficient at the same temperature and flow rates ranging between 2.0-4.0 l/min for parallel flow and counterflow in cases of the closed and open circuits is seen in the parallel flow closed

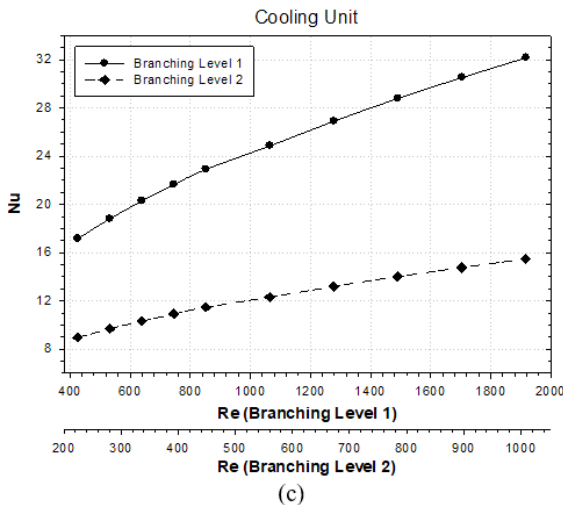
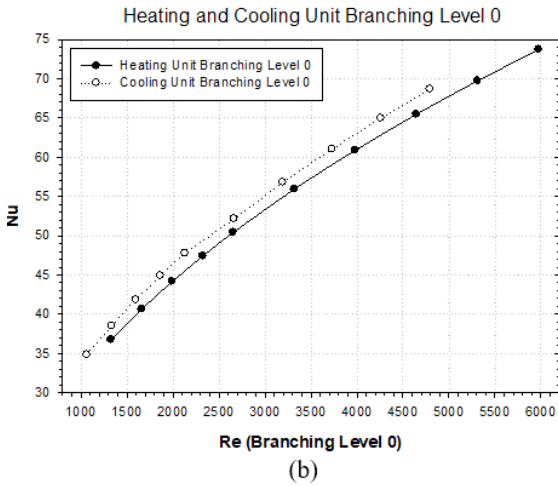
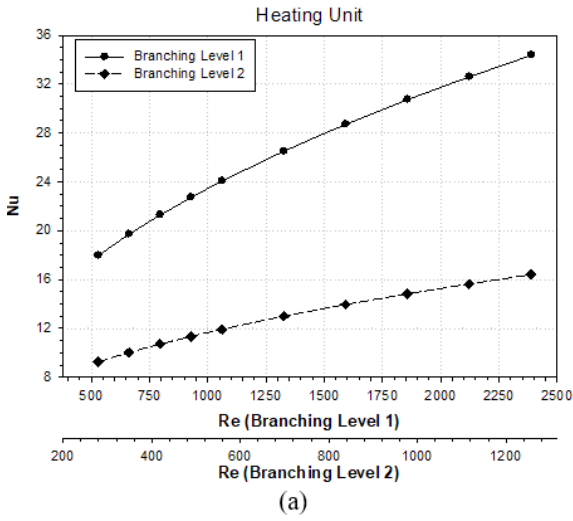


Figure 22. Change of the Nu-Re numbers at an inlet temperature of 65°C for the operating conditions of the counterflow closed circuit

circuit. It was observed that the total heat transfer coefficient U ($W/m^2.K$) showed a greater change in the parallel flow operation when compared to the counterflow operation at the same temperature and in the same range of flow rate for

closed and open circuits.

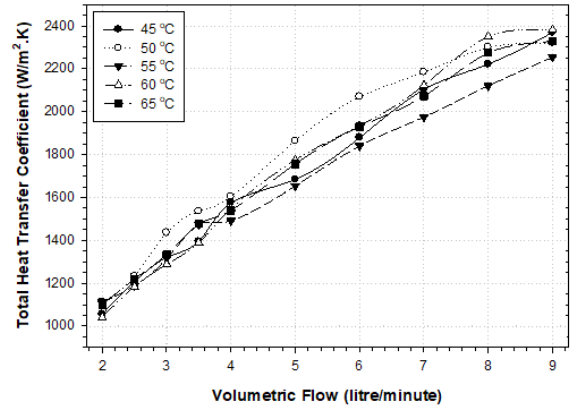


Figure 23. Change of the total heat transfer coefficient by the volumetric flow rate in the parallel flow closed circuit

Impact Analysis of Thermal Capacity Rates

In order to evaluate theoretical and experimental research and compare the impacts of thermal capacity rates on effectiveness, tests were carried out for the thermal capacity rates of $Cr=1$, $Cr=0.25$ and $Cr=0.125$ and a fluid inlet temperature of 65°C in the heating unit.

For a thermal capacity rate of $Cr=1$, fluid flow rates of the heating and cooling fluids are equal while entering into the system.

For a thermal capacity value of $Cr=0.25$, while the heating fluid ranges between 4.00 l/min – 8.00 l/min, the cooling fluid ranges between 1.00 l/min – 2.00 l/min. For a thermal capacity value of $Cr=0.125$, the heating fluid has a value of 8.00 l/min and the cooling fluid has a value of 1.00 l/min. Increasing the heating fluid inlet flow rate causes an increase in the mean temperature of the heated part of the middle plate and a further heat transfer to the fluid in the

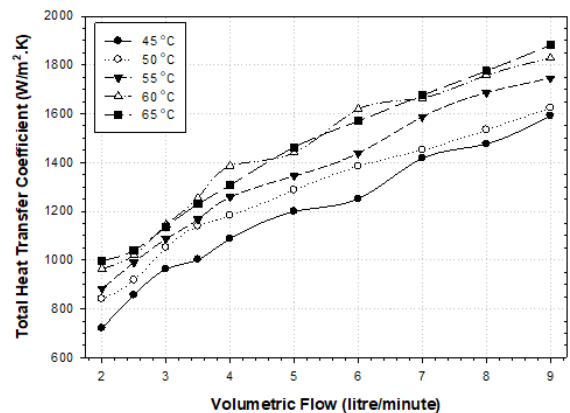


Figure 24. Change of the total heat transfer coefficient by the volumetric flow rate in the counterflow closed circuit

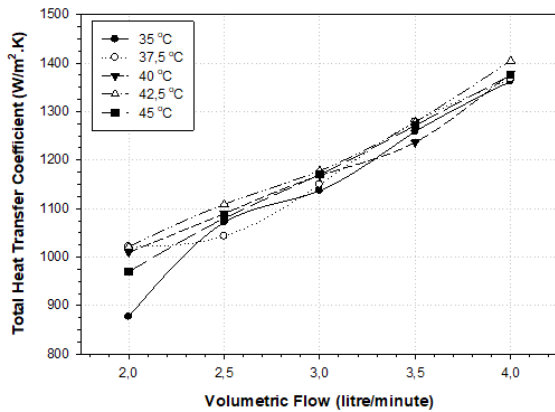


Figure 25. Change of the total heat transfer coefficient by the volumetric flow rate in the parallel flow open circuit

cooling side. In Fig. 27, results of the test, which shows the impacts of thermal capacity rates on effectiveness, are presented. As it is seen in the diagram, according to the ϵ - NTU method for different Cr values, it ranges between $\epsilon=0.24$ - 0.58 , $NTU=0.3$ - 0.81 . In addition, a theoretical and experimental comparison was made according to the ϵ - NTU method for different Cr values, and it was seen that both experimental and theoretical results are consistent with the literature. As a result of the conducted tests, it was concluded that increasing the thermal capacity rates causes an increase in effectiveness (ϵ).

ANSYS-FLUENT ANALYSES

In this study, the designed dendritic branching-channel heat exchanger was geometrically modelled in Solid Works and numerically analyzed in ANSYS-Fluent 16.0 software package. While laminar model was applied in the tests up to a fluid flow rate of 4.0 l/min, k - ϵ turbulence model was applied in a higher flow rate than 4.0 l/min; and they were thermally analysed by solving the energy and Navier-Stokes equations. Upon the designed dendritic branching-channel heat exchanger;

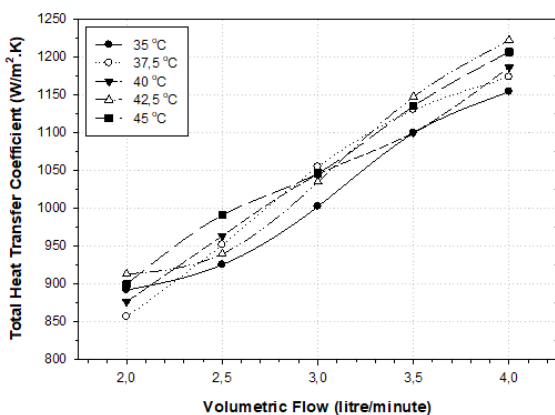


Figure 26. Change of the total heat transfer coefficient by the volumetric flow rate in the counterflow open circuit

- i) Impacts of Temperature Change,
- ii) Impacts of Flow Rate Change,
- iii) Impacts of Operation Regime Change were examined in ANSYS-FLUENT.

It was seen that results obtained from the analyses performed by using ANSYS-FLUENT software was consistent with the test results. It was seen in the performed analyses that, in accordance with the constructal theory, flow rate of the fluid in sub-branches other than branching level zero ($k=0$) was lower when compared to the pipes which are coaxial with branching level zero. It was observed that this situation caused a lower flow rate in sub-branches from branching level one ($k=1$) and also further decrease of the rate since branching level two ($k=2$) was affected by branching level one.

CONCLUSION

In dendritic branching-channel heat exchangers, it is possible to achieve higher Nusselt numbers and to increase the heat transfer rate by carefully calculating channel sections, channel geometries and channel dimensions. Hydrodynamical and thermal re-development of the Nusselt number and heat transfer value in each channel and at each branching level is an important characteristic of this geometry. In Fig. 11-14, change of the heat transfer for parallel flow and counter-flow in the open and closed circuits by the volumetric flow rate was given, and it was observed that the heat transfer value increased with increasing volumetric flow rate.

In Fig. 15, change of the ratio of the heat transfer value to the inflowing heat by the volumetric flow rate is given, and since the mean temperature of the test zone in the experiment system was lower in the open circuit, it was determined that this ratio was higher in the open circuit.

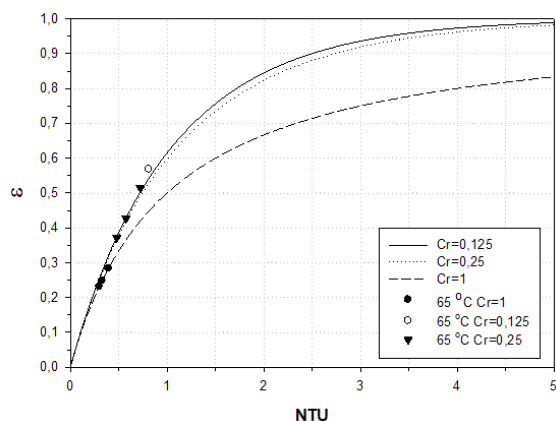


Figure 27. Impacts of the thermal capacity rates on effectiveness

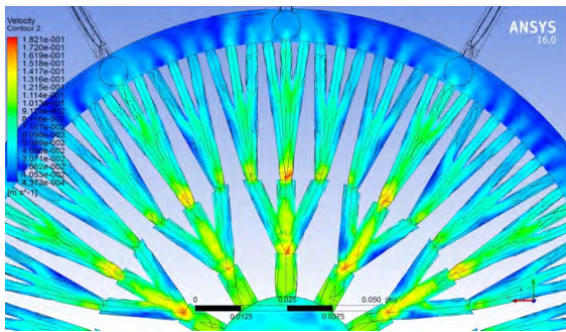


Figure 28. Rate distributions in the heat exchanger for 2.0 l/min for the flow towards increasing branching levels

In Fig. 16, change of the pressure losses towards increasing and decreasing branching levels by the volumetric flow rate and the Reynolds numbers in the branches is presented, and it is seen that pressure losses increase with increasing volumetric flow rates and Reynolds numbers in the branches. This result indicates that an increase in branching level is not important in the flow channels with such dendritic branching (fractal) channel structure.

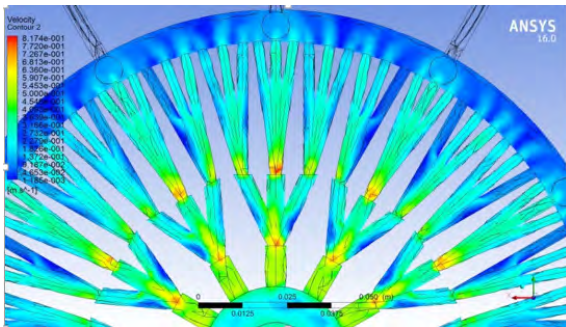


Figure 29. Rate distributions in the heat exchanger for 9.0 l/min for the flow towards increasing branching levels

In the diagrams in Fig. 17-20, change of the log mean temperature difference by the volumetric flow rate for parallel flow and counter-flow operation in open and closed circuits is given. In case of the closed circuit, the log mean temperature difference gradually decreases in both flow regimes as the volumetric flow rate increases. In case of the open circuit, the log mean temperature difference gradually increases in both flow regimes as the volumetric flow rate

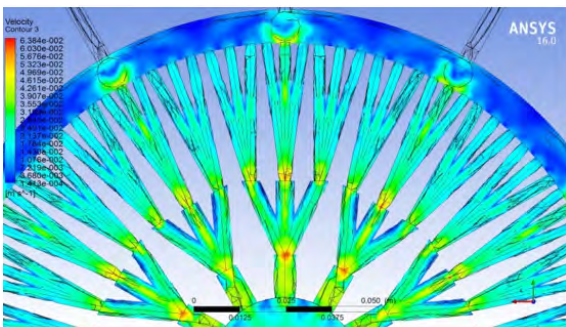


Figure 30. Rate distributions in the heat exchanger for 2.0 l/min for the flow towards decreasing branching levels

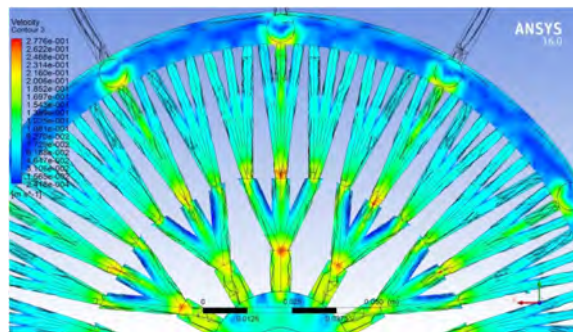


Figure 31. Rate distributions in the heat exchanger for 9.0 l/min for the flow towards decreasing branching levels

increases. The logmean temperature difference increases with increasing inlet temperature.

In the diagrams in Fig. 21-22, changes of Nu-Re numbers for different inlet temperatures in the heating side under parallel flow and counterflow operating conditions in closed and open circuits at different levels. As it is seen in the diagrams, Nusselt numbers increase with increasing Reynolds numbers, depending on branching levels at varying flow rates and temperatures. Likewise, it is graphically showed that a greater increase is seen in the Nusselt number at branching level one. The volumetric flow rate increasing in the heating and cooling sides caused the Nusselt number to increase in a decelerating manner; and thus, it caused the heat convection coefficient, and therefore the heat transfer

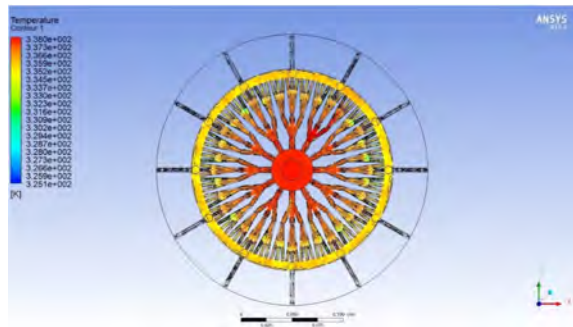


Figure 32. Temperature distribution in the heating unit under the parallel flow closed circuit conditions for a heating fluid inlet temperature of 65°C and a flow rate of 9.0 l/min

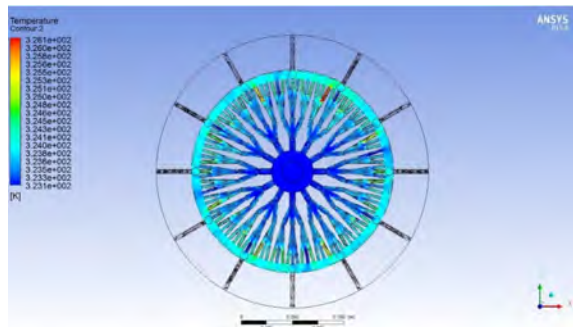


Figure 33. Temperature distribution in the cooling unit under the parallel flow closed circuit conditions for a heating fluid inlet temperature of 65°C and a flow rate of 9.0 l/min

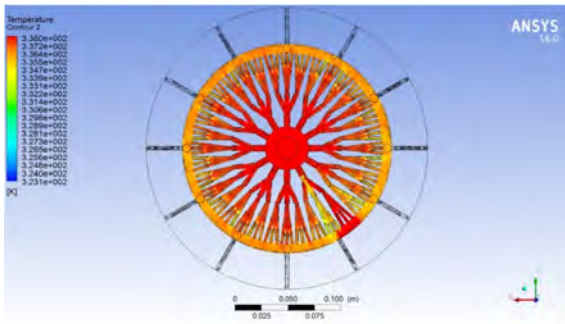


Figure 34. Temperature distribution in the heating unit under the counterflow closed circuit operating conditions for a heating fluid inlet temperature of 65°C and a flow rate of 9.0 l/min

value Q (Watt), to increase in a decelerating manner with the volumetric flow rate.

Change of the total heat transfer coefficient (U) by the volumetric (\dot{V}) flow rate according to the tests performed for parallel flow and counterflow under the closed circuit operating conditions (45, 50, 55, 60 and 65°C) are given in Figure 23-26 and under the open circuit operating conditions (35, 37.5, 40, 42.5 and 45°C) are given in Figure 33-34. It is seen in the diagrams of the experimental results that the total heat transfer coefficient increased by increasing volumetric flow rate under both parallel flow and counterflow conditions. In case of the parallel flow closed circuit, the total heat transfer coefficient was higher when compared to the counterflow. The same can be said for the open circuit as well.

Since the tests were carried out under $Cr=1$ conditions of the dendritic branching-channel heat exchanger, volumetric flow rates for the fluids circulating in both units are equal. At a thermal capacity flow rate of $Cr=1$, it was seen that the maximum effectiveness coefficient value is at $\epsilon=0.30$ level. When the thermal capacity flow rates were changed to $Cr=0.125$ level, it was seen that $\epsilon=0.58$ and $NTU=0.81$ in case of counterflow operation. In the diagram in Figure 27, the increased inlet flow rate of the heating fluid increased the mean temperature on the plate and this caused the effectiveness coefficient to rise.

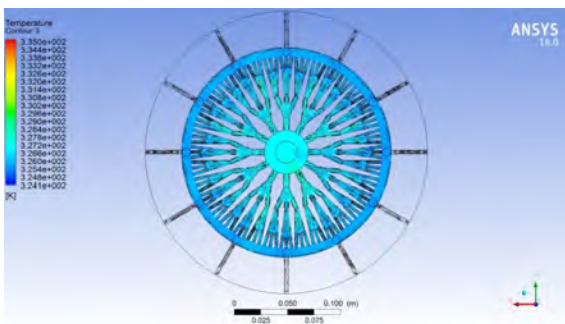


Figure 35. Temperature distribution in the cooling unit under the counter-flow closed circuit operating conditions for a heating fluid inlet temperature of 65°C and a flow rate of 9.0 l/min

Changes of rate and temperature were analyzed for different flow rate and temperature values in ANSYS, and the results are given as diagrams in Fig. 31-35.

Symbols

- A Heat Transfer Surface Area (m²)
- A_0 Level 0 Branching Heat Transfer Surface Area
- A_1 Level 1 Branching Heat Transfer Surface Area
- A_2 Level 2 Branching Heat Transfer Surface Area
- A_k Level k Channel Surface Area
- C_h Thermal Capacity Flow Rate of Hot Fluid (W/K)
- C_c Thermal Capacity Flow Rate of Cold Fluid (W/K)
- C_{max} Maximum Thermal Capacity Flow Rate (W/K)
- C_{min} Minimum Thermal Capacity Flow Rate (W/K)
- C_r Ratio of Thermal Capacity Flow Rates
- D Pipe Diameter (m)
- $D_{h,k}$ Level k Branch Hydraulic Diameter (m)
- D_h Hydraulic Diameter (m)
- ΔP Pressure Difference (Pa)
- ΔT Temperature Difference (K)
- ϵ Effectiveness
- k Thermal Conductivity Coefficient (W/mK)
- L_k Level k Branch Length (m)
- L Length (m)
- $LMTD$ Log Mean Temperature Difference (°C)
- \dot{m} Volumetric Flow Rate (kg/s)
- \dot{m}_h Hot Fluid Flow Rate (kg/s)
- \dot{m}_c Cold Fluid Flow Rate (kg/s)
- $MEMS$ Micro Electromechanical Systems
- N_k Number of Channels
- N Number of Branches
- Nu Nusselt Number
- NTU Number of Transfer Units

ρ Density

Q From Hot Fluid to Cold Fluid Heat Transfer Value

(W)

$Q_{\%thermal\ difference}$ % difference between the Heat Entering

into the Experiment System and the Heat Received from the System

Q_r Heat Received from the Experiment System (W)

Q_g Heat Entering into the Experiment System (W)

Q_{losses} Heat Loss (W)

Q_{max} Maximum Possible Heat Transfer from Hot Fluid to Cold Fluid (W/)

Q_{mean} Mean of the Heat Entering into the Experiment

System and the Heat Received from the System

$Q_{con.}$ Heat Transferred through Convection (W)

Q_{top} Total of Convection, Radiation and Lost Heat Values (W)

$Q_{rad.}$ Heat Transferred through Radiation (W)

Re Reynolds Number

T Temperature (°C)

$T_{h,i}$ Inlet Temperature of the Hot Fluid Entering into the Heat Exchanger (K)

$T_{h,o}$ Outlet Temperature of the Hot Fluid Coming out of the Heat Exchanger (K)

$T_{c,i}$ Inlet Temperature of the Cold Fluid Entering into the Heat Exchanger (K)

$T_{c,o}$ Outlet Temperature of the Cold Fluid Coming out of the Heat Exchanger (K)

U Total Heat Transfer Coefficient (W/m².K)

μ Dynamic Viscosity (Pa.s)

ν Viscosity

V Velocity (m/s)

References

1. Andhare RS, Shoostari A, Dessiatoun SV, Ohadi MM. Heat transfer and pressure drop characteristics of a flat plate manifold microchannel heat exchanger in counter flow configuration. *Applied Thermal Engineering* 96 (2016) 178-189.
2. Bejan A. Constructal-theory network of conducting paths for cooling a heat generating volume. *International Journal of Heat and Mass Transfer* 40 (1997) 799-816.
3. Bejan A. Dendritic constructal heat exchanger with small-scale crossflows and larger-scales counterflows. *International Journal of Heat and Mass Transfer* 45 (2002) 4607-4620.
4. Bonjour J, Rocha LAO, Bejan A, Meunier F. Dendritic fins optimization for a coaxial two-stream heat exchanger. *International Journal of Heat and Mass Transfer* 47 (2003) 111-124.
5. Calamas D, Baker J. Tree-like branching fins: Performance and natural convective heat transfer behavior. *International Journal of Heat and Mass Transfer* 62 (2013) 350-361.
6. Chen Y, Cheng P. An experimental investigation on the thermal efficiency of fractal tree-like microchannel nets. *International Communications in Heat and Mass Transfer* 32 (2005) 931-938.
7. Chen Y, Zhang C, Shi M, Yang Y. Thermal and Hydrodynamic Characteristics of Constructal Tree-Shaped Minichannel Heat Sink. *American Institute of Chemical Engineers* 56 (2010) 2018-2029.
8. Da Silva AK, Lorente S, Bejan A. Constructal multi-scale tree-shaped heat exchangers. *Journal Of Applied Physics* 96 (2004) 1709-1718.
9. Daniels BJ, Pence DV, Liburdy JA. Predictions of Flow Boiling in Fractal-like Branching Microchannels. *ASME Proceedings of IMECE 2005, Orlando, Florida, USA, 5 - 11 November, pp. 359-368, 2005.*
10. Escher W, Michel B, Poulikakos D. Efficiency of optimized bifurcating tree-like and parallel microchannel networks in the cooling of electronics. *International Journal of Heat and Mass Transfer* 52 (2009) 1421-1430.
11. Ghodoossi L. Thermal and hydrodynamic analysis of a fractal microchannel network. *Energy Conversion and Management* 46 (2005) 771-788.
12. Hernando NG, Iborra AA, Rivas UR, Izquierdo M. Experimental investigation of fluid flow and heat transfer in a single-phase liquid flow micro-heat exchanger. *International Journal of Heat and Mass Transfer* 52 (2009) 5433-5446.
13. Heymann D, Pence D, Narayanan V. Optimization of fractal-like branching microchannel heat sinks for single-phase flows. *International Journal of Thermal Sciences* 49 (2010) 1383-1393.
14. [14] Hong FJ, Cheng P, Ge H, Goh Teck Joo. Conjugate heat transfer in fractal-shaped microchannel network heat sink for integrated microelectronic cooling application. *International Journal of Heat and Mass Transfer* 50 (2007) 4986-4998.
15. Hung TC, Yan WM, Li WP. Analysis of heat transfer characteristics of double-layered microchannel heat sink. *International Journal of Heat and Mass Transfer* 55 (2012) 3090-3099.
16. Kim DK. Thermal optimization of branched-fin heat sinks subject to a parallel flow. *International Journal of Heat and Mass Transfer* 77 (2014) 278-287.
17. Kwak Y, Pence D, Liburdy J, Narayanan V. Gas-liquid flows in a microscale fractal-like branching flow network. *International Journal of Heat and Fluid Flow* 30 (2009) 868-876.
18. Lee YJ, Singh PK, Lee PS. Fluid flow and heat transfer investigations on enhanced microchannel heat sink using oblique fins with parametric study. *International Journal of Heat and Mass Transfer* 81 (2015) 325-336.

19. Lin WW, Lee DJ. Diffusion-convection process in a branching fin. *Chemical Engineering Communications* 158 (1997) 59-70.
20. Meyer JP, Van der Vyver H. Heat Transfer Characteristics of a Quadratic Koch Island Fractal Heat Exchanger. *Heat Transfer Engineering* 26 (2005) 22-29.
21. Moreno A, Murphy K, Wilhite BA. Parametric study of solid-phase axial heat conduction in thermally integrated microchannel networks. *Industrial Engineering Chemistry Research* 47 (2008) 9040-9054.
22. Murray CD. The physiological principle of minimum work; I. The vascular system and the cost of blood volume. *P.N.A.S.* 12 (1926) 207-214.
23. Park KT, Kim HJ, Kim DK. Experimental study of natural convection from vertical cylinders with branched fins. *Experimental Thermal and Fluid Science* 54 (2014) 29-37.
24. Pence DV. Reduced Pumping Power and Wall Temperature in Microchannel Heat Sinks with Fractal-like Branching Channel Networks. *Microscale Thermophysical Engineering* 6 (2002) 319-330.
25. Pence D, Enfield K. Inherent Benefits in Microscale Fractal-like Devices for Enhanced Transport Phenomena. *Design and Nature II Comparing Design in Nature with Science and Engineering*, WIT Press (2004) 317-327.
26. Pence DV. Improved Thermal Efficiency and Temperature Uniformity using Fractal-like Branching Channel Networks. *Proceedings of the International Conference on Heat Transfer and Transport Phenomena in Microscale*, ed. G.P. Celata, Begell House, New York, pp. 142-148, 2000.
27. Xu P, Yu B, Yun M, Zou M. Heat conduction in fractal tree-like branched networks. *International Journal of Heat and Mass Transfer* 49 (2006) 3746-3751.
28. Peterson RB. Numerical modeling of conduction effects in microscale counterflow heat exchangers. *Microscale Thermophysical Engineering* 3 (1999) 17-30.
29. Salakij S, Liburdy JA, Pence DV, Apreotesi M. Modeling in situ vapor extraction during convective boiling in fractal-like branching microchannel networks. *International Journal of Heat and Mass Transfer* 60 (2013) 700-712.
30. Da Silva AK, Bejan A. Dendritic counterflow heat exchanger experiments. *International Journal of Thermal Sciences* 45 (2006) 860-869.
31. [31] Stief T, Langer OU, Schubert K. Numerical investigations of optimal heat conductivity in micro heat exchangers. *Chemical Engineering Technology* 21 (1999) 297-303.
32. Tuckerman DB, Pease RFW. High-performance heat sinking for VLSI. *IEEE Electron Device Letters* 2 (1981) 126-129.
33. Vafai K, Zhu L. Analysis of two-layered microchannel heat sink concept in electronic cooling. *International Journal of Heat and Mass Transfer* 42 (1999) 2287-2297.
34. Wechsato W, Lorente S, Bejan A. Optimal tree-shaped networks for fluid flow in a disc-shaped body. *International Journal of Heat and Mass Transfer* 45 (2002) 4911-4924.
35. West GB, Brown JH, Enquist BJ. A General Model for the Origin of Allometric Scaling Laws in Biology. *Science* 276 (1997) 122-126.
36. Xia C, Fu J, Lai J, Yao X, Chen Z. Conjugate heat transfer in fractal tree-like channels network heat sink for high-speed motorized spindle cooling. *Applied Thermal Engineering* 90 (2015) 1032-1042.
37. Xu S, Wang W, Fang K, Wong CN. Heat transfer performance of a fractal silicon microchannel heat sink subjected to pulsation flow. *International Journal of Heat and Mass Transfer* 81 (2015) 33-40.
38. Yang Y, Morini GL, Brandner JJ. Experimental analysis of the influence of wall axial conduction on gas-to-gas micro heat exchanger effectiveness. *International Journal of Heat and Mass Transfer* 69 (2014) 17-25.
39. Zhang C, Lian Y, Yu X, Liu W, Teng J, Xu T, Hsu CH, Chang YJ, Greif R. Numerical and experimental studies on laminar hydrodynamic and thermal characteristics in fractal-like microchannel networks. Part B: Investigations on the performances of pressure drop and heat transfer. *International Journal of Heat and Mass Transfer* 66 (2013) 939-947.
40. Zimparov VD, Da Silva AK, Bejan A. Constructal tree-shaped parallel flow heat exchangers. *International Journal of Heat and Mass Transfer* 49 (2006) 4558-4566.
41. Chong SH, Ooi KT, Wong TN. Optimisation of single and double layer counter flow microchannel heat sinks. *Applied Thermal Engineering* 22 (2002) 1569-1585.
42. Lee YJ, Singh PK, Lee PS. Fluid flow and heat transfer investigations on enhanced microchannel heat sink using oblique fins with parametric study. *International Journal of Heat and Mass Transfer* 81 (2015) 325-336.
43. Bier W, Keller W, Linder G, Seidel D, Schubert K, Martin H. Gas to gas heat transfer in micro heat exchangers. *Chemical Engineering and Processing: Process Intensification* 32 (1993) 33-43.
44. Bejan A. Street network theory of organization in nature. *Journal of Advanced Transportation*, 30 (1996), 85-107.
45. Bejan A. Constructal theory of pattern formation, *Hydrology and Earth System Sciences* 11 (2007) 753-768.
46. Bonjour J, Rocha LAO, Bejan A, Meunier F. Dendritic fins optimization for a coaxial two-stream heat exchanger. *International Journal of Heat and Mass Transfer* 47 (2003) 111-124.
47. Cohn DL. Optimal systems: I. The vascular system. *Bulletin Of Mathematical Biophysics* 16 (1954) 59-74.
48. Lee DJ, Lin WW. Second law analysis on fractal-like fin under crossflow. *American Institute of Chemical Engineers Journal* 41(1995) 2314-2317.
49. Lin WW, Lee DJ. Diffusion-convection process in a branching fin, *Chemical Engineering Communications* 158 (1997) 59-70.
50. Chen Y, Cheng P. Heat transfer and pressure drop in fractal tree-like microchannel nets. *International Journal of Heat and Mass Transfer* 45 (2002) 2643-2648.
51. Park KT, Kim HJ, Kim DK. Experimental study of natural convection from vertical cylinders with branched fins. *Experimental Thermal and Fluid Science* 54 (2014) 29-37.
52. Lorenzini G, Rocha LAO. Constructal design of Y-shaped assembly of fins. *International Journal of Heat and Mass Transfer* 49 (2006) 4552-4557
53. Cengel YA, Cimbala JM. *Akiskanlar Mekanigi Temelleri ve Uygulamalari*. Guven Bilimsel, İzmir, 2007.
54. Cengel YA. *Isi ve Kotle Transferi*. Guven Kitabevi, Izmir, 2011.
55. Genceli OF. *Isi Degistiricileri*. Birsen Yayınevi, İstanbul, 2010.
56. Stephan K, Preusser P. Heat Transfer and Critical Heat Flux in Pool Boiling of Binary and Ternary Mixtures. *German Chemical Engineering*, 2 (1979) 161-169.

Analysis of Steam Injection into Combustion Chamber of Gas Turbine Cogeneration Cycles

Rabi KARAALI¹  İlhan Tekin ÖZTÜRK² 

¹Bayburt University, Department of Mechanical Engineering, 69000, Bayburt, TURKEY

²Kocaeli University, Department of Mechanical Engineering, 41380, Kocaeli, TURKEY

ABSTRACT

Cogeneration is known as the generation of heat energy and electricity at same time by using the fuel's energy. There are various cogeneration systems, and steam injection is made into combustion chamber to increase the efficiency of the cycle and to reduce nitrogen oxide emissions. The most fundamental thermodynamic, operational, economical and thermo-economic factors must be considered when choosing the appropriate cogeneration system and designing the system. For the thermodynamic factors, such as the amount of fuel to be consumed, the electric heat rate, the artificial thermal efficiency, the fuel energy gain rate must be found for the unit amount of electric power to be obtained. The cost and availability of the fuel to be used must also be estimated by considering the problems will be affected by repair maintenance and economic fluctuations. In economic factors, the annual cash flow of the system and the amortization itself are calculated. In the thermo-economic factors, the investment costs depend on the exergy efficiency and the exergy of the products of the devices and the fuel required to operate are calculated. In this study, the analysis of steam injection into cogeneration systems according to performance and evaluation criteria was done using energy, exergy and economic methods. To calculate the energy and exergy values of the flows, a program was written by the authors in the FORTRAN programming language and the results obtained by running them were used. The results obtained were compared with the literature values and correctness was observed.

Keywords:

Cogeneration; Performance; Evaluation Criteria

Article History:

Received: 2018/03/23

Accepted: 2018/03/30

Online: 2018/09/07

Correspondence to: Rabi Karaali,
Bayburt University, Department of
Mechanical Engineering, 69000, Bayburt,
TURKEY
E-Mail: rabikar@gmail.com

INTRODUCTION

As is known, the usage of electric energy continues to increase in our country and in the world. Industrial establishments set up cogeneration facilities to meet both electricity and heat energy needs, and provide a more efficient use of fuels. Thus, energy consumption reduces their costs and they are also avoided of electricity interruptions. Small-scale cogeneration facilities, however, are also widely used in small businesses, university campuses, hotels, and district heating systems.

In the cogeneration plants, electrical energy and heat energy are produced at the same time so that higher efficiencies can be obtained. The energy efficiency of such plants is approaching 90%. If these plants are used especially for heating of the houses, cooling water can be produced by operating an absorption cooling

group with the help of exhaust heat even outside the heating season. In this regard, the production is directed to three purposes, so three generation is the issue and the annual usage period of the cogeneration plant is increasing [1, 15, 19]. When these advantages are evaluated, more economical energy production can be saved. In addition, less pollution is created and the amount of CO₂ released to the atmosphere is lower. Different cogeneration systems are available. These can be classified as steam turbines, gas turbines, internal combustion diesel or gas engines and fuel cells. Different methods are proposed and used in the design stage and usage stage to increase the efficiency of the selected cogeneration plants according to the usage purposes.

Steam injection into the cycle's combustion chamber has continued to be implemented since in the 1950s

with the aim of reducing the outlet temperature and increasing the work force achieved, and now reducing NO_x and its compounds to minimum levels. Studies of exergy analysis in this area have been started by many researchers since the 1980s [24].

The concept of thermoeconomics was first introduced in the 1960s and later developed by C. Frangopoulos, G. Tsatsaronis, A. Valero and M. Spakovsky, especially in the 1990s [17, 20, 22]. By describing a recuperative gas turbine cogeneration system called the CGAM problem (consisting of the initials of their names), as a simple and defined optimization problem, they propose their own optimization methods by comparing their respective solution paths. This system has a steam capacity of 30 MW electricity and saturated steam at 14 kg/s, 2 MPa, and each researcher's optimization method gave similar results.

Lazzeratto and Tsatsaronis developed cost equations, that are named SPECO / AVCO-specific cost / average cost approach [12, 13, 21, 23]. Kim et al., proposed Modified productive structure analysis (MOPSA), and Rosen and Dincer, proposed Exergy cost energy mass analysis (EXCEM) methods [16]. According to El-Sayed and Gaggioli, thermoeconomics implements two basic methods [6]. These are integral calculation methods and algebraic method. The algebraic method always uses the cost equations of the devices, and gives information on the average cost. In the integral calculation method, flow costs are calculated for each flow and device using differential equations and marginal costs are found. The Lagrange multipliers method is used most frequently [23]. The definition of cost equations for devices in the algebraic method is not objective.

The method of integral calculus is also subjective. Because, it is based on the Lagrange multipliers technique and is based on the definition of the mathematical function of each device, and when the isolation of the devices is not successful, there would be major errors in the iterative steps. For the solution of this problem, C. Frangopoulos proposed the thermoeconomic functional approach in his doctoral dissertation in 1983. Accordingly, a function and a product are defined for each device, to eliminate the need of a cost equation [7].

Cerqueira and Nebra compared the CGAM cycle by using the four thermoeconomic analyzes. According to this, the thermoeconomic functional approach gives a result in the middle among others (7.1 \$ / GJ), and the exergetic costs method gives the most expensive power cost (8.2 \$ / GJ). The exhaust gas cost is taken as zero at the exergy cost. The result is that all the irreversibilities are found in the heat exchanger [3]. Kwak et al. applied MOPSA and SPECO / AVCO methods to solve the CGAM problem, and compared these

findings with the findings of Torres et al. [10]. According to Torres et al., for per the unit cost, \$ 7.42 \$ / GJ for their method, 8.46 \$ / GJ for the MOPSA and 7.80 \$ / GJ for the SPECO / AVCO methods.

According to Boyce, steam injected into the combustion chamber injects about 2-3% of the air mass for reducing and controlling NO_x, which increases the electric power obtained by about 3-5%. When steam mass injected into the combustion chamber about 5% of the air mass, the electricity efficiency increases in the sample cycle 8.3% and if this steam is produced from the exhaust of the turbine, the electricity efficiency is increased by 19%. According to the same article, if the amount of water or steam is about 12% of the amount of air, the electric power obtained increases by about 25% [2]. Kehlhofet et al., draws curves showing the effect of the amount of injected steam on relative work and relative efficiency, where the amount of work obtained is 14% when the steam fuel ratio is 1.5 [9]. According to Wang and Chiou, the amount of steam to be injected can be up to 20% of the mass of the compressor inlet air [24]. The energy efficiency does not change when the compression ratio in the steam injection cycle increases from 5 to 20 in the study. In addition, the same researchers analyzed the use of regeneration and steam injection methods to increase the efficiency of a simple gas turbine power generation system based in Taiwan. All the findings of Wang and Chiou are consistent with the findings in this study.

In this study, the sample, the air preheated and the air fuel preheated cogeneration systems are analyzed by using the first and second laws of thermodynamics, and the required income methods. The cost of the main product is calculated in four steps in the economic analysis with the required income method. These are cost accounting and forecasting of the total investment, determination of economic, financial, labor and market input parameters for the detailed cost account, calculation of total income needed and calculation of product cost with these values.

In the calculations the compression ratios, the compressor and turbine isentropic efficiencies the combustion chamber outlet temperatures, the change in air flow, fuel flow and the recuperator outlet temperatures are taken into consideration. Thus, the effects of steam injection into these three different cycles, design differences and the effect of each added device on optimum values are also investigated. The thermoeconomic analysis of the sample, air, and fuel air preheated cycles, for the injection of steam into their combustion chamber, for the different air fuel and compression ratios are done, and the performance curves obtained and compared. For this, two separate studies have been carried out, namely the performance of all the systems and the performance of each device that constitutes the systems. The

effects of various air fuel and compressor compression ratios on the power, the efficiency, the cost of obtained products, the artificial thermal efficiency, the fuel energy gain, the electric heat ratios and fuel consumption have been drawn and related curves are plotted.

Many advanced computer programs exist in the market to be used in performing the analyze described in this study and can be grouped into two groups, one approaching solving sequential modules and equations systems. In sequential module approach programs, the devices are combined by selecting from the menu, the input values are given and the program is executed and results are obtained. These are ready-made visual programs, such as ASPEN PLUS, PROCESS, CHEMCAD programs are such programs. The SPEED UP and the EESP programs are solving the equations of the systems of by establishing a mathematical model of each device so that the mathematical model of the system is revealed as hundreds of equations (or set of equations) and solved for the common variables. Here, as a two-tuple synthesis, mathematical and economic models of systems with separate sequential modules are developed in the FORTRAN programming language, executed, and the results obtained are discussed.

MATERIALS AND METHODS

In conventional systems, heat is generated at two separate sites to produce power and heat. In the cogeneration system, heat is generated by a single heat generation system. Electric energy is generated by the energy carrier fluid and the remaining energy is used for the production of heat (steam or hot water). The obtained total energy of the conventional system is around 50%, while the efficiency of the cogeneration plant is around 80-90%. In addition, by installing a cogeneration plant, the operating and initial investment costs of the system can be significantly reduced [25]. In gas turbine cogeneration plants, the main machine is the gas turbine.

As can be seen in Figure 1, after the high-pressure air from the compressor is burned with methane gas in the combustion chamber, and after that some of the energy of the exhaust gases are converted to electrical energy in the gas turbine. After that the resulting high-temperature exhaust gases are released by leaving a large portion of the remaining energy in the heat exchanger to the water [1, 18]. The obtained hot water is used for steam heating, drying, meeting the process requirement, generating steam by using steam turbine, absorbing cooling and similar processes. Different cycles are obtained by adding other devices to the main machine such as recuperator, steam injector, heat exchanger, absorption cooling, and steam turbine [1].

In Figure 1 steam injection of a) air preheated, b) air-fuel preheated, and c) sample cycles are shown. Cogeneration plants consist of different devices, in which temperature, pressure, chemical composition change. There is also a chemical reaction in the combustion chamber. The assumptions made in the analysis of the systems in this thesis are as follows [1].

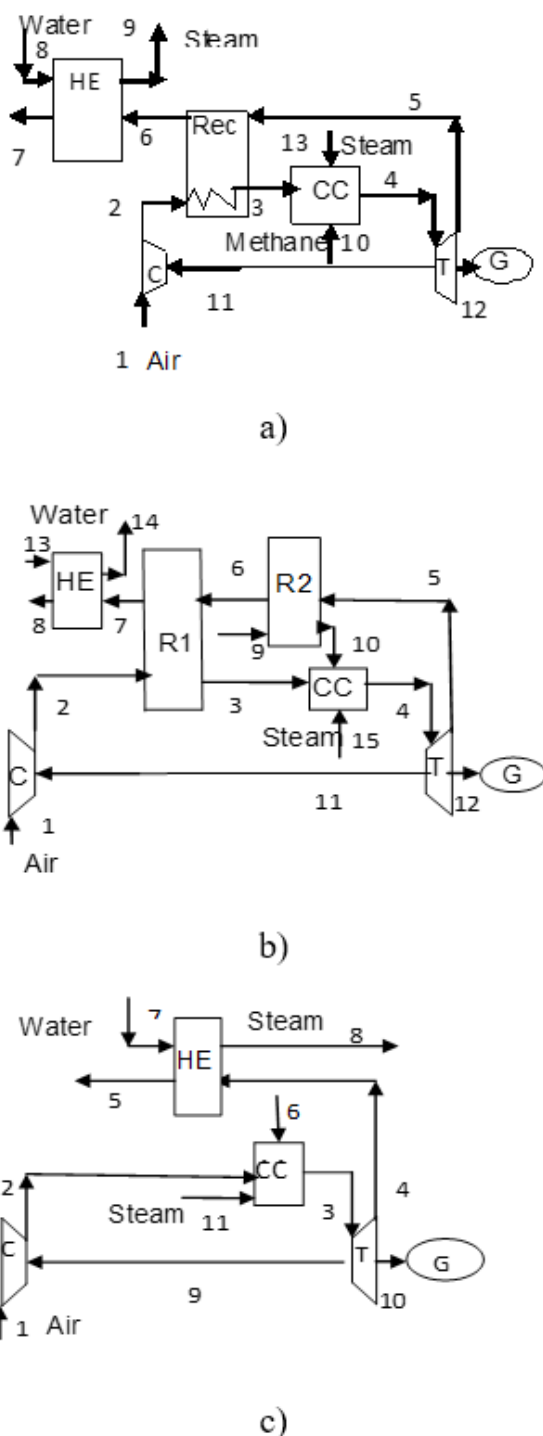


Figure 1. Steam injection of a. air preheated, b. air-fuel preheated, and c. sample cycles.

Table 1. Mass, energy and entropy equations of each devices of the air preheated cycle [4, 5].

Devices	Mass equations	Energy equations	Entropy equations
Compressor	$\dot{m}_1 = \dot{m}_2$	$\dot{m}_1 h_1 + \dot{W}_C = \dot{m}_2 h_2$	$\dot{m}_1 s_1 - \dot{m}_2 s_2 + \dot{S}_{gen,C} = 0$
Recuperator	$\dot{m}_2 = \dot{m}_3$ $\dot{m}_5 = \dot{m}_6$	$\dot{m}_2 h_2 + \dot{m}_5 h_5 = \dot{m}_3 h_3 + \dot{m}_6 h_6$	$\dot{m}_2 s_2 + \dot{m}_5 s_5 - \dot{m}_3 s_3 - \dot{m}_6 s_6 + \dot{S}_{gen,R} = 0$
Combustion chamber	$\dot{m}_3 + \dot{m}_{10} + \dot{m}_{13} = \dot{m}_4$	$\dot{m}_3 h_3 + \dot{m}_{10} h_{10} + \dot{m}_{13} h_{13} - 0.02 \dot{m}_{10} LHV = \dot{m}_4 h_4$	$\dot{m}_3 s_3 + \dot{m}_{10} s_{10} + \dot{m}_{13} s_{13} - \dot{m}_4 s_4 + \dot{S}_{gen,CC} = 0$
Turbine	$\dot{m}_4 = \dot{m}_5$	$\dot{m}_4 h_4 = \dot{W}_T + \dot{W}_C + \dot{m}_5 h_5$	$\dot{m}_4 s_4 - \dot{m}_5 s_5 + \dot{S}_{gen,T} = 0$
Heat exchanger	$\dot{m}_6 = \dot{m}_7$ $\dot{m}_8 = \dot{m}_9$	$\dot{m}_6 h_6 + \dot{m}_8 h_8 = \dot{m}_7 h_7 + \dot{m}_9 h_9$	$\dot{m}_6 s_6 + \dot{m}_8 s_8 - \dot{m}_7 s_7 - \dot{m}_9 s_9 + \dot{S}_{gen,HE} = 0$
All cycle		$\bar{h}_i = f(T_i)$ $\bar{s}_i = f(T_i, P_i)$ $\dot{m}_{air} h_{air} + \dot{m}_f LHV_{CH_4} - \dot{Q}_{Loss,CC} - \dot{m}_{eg,out} h_{eg,out} - \dot{W}_T - \dot{m}_{steam} (h_{w,in} - h_{steam,out}) = 0$ $\dot{Q}_{Loss,CC} = 0.02 \dot{m}_f LHV_{CH_4}$	

The cogeneration system operates in a steady state regime, the ideal gas mixture laws are valid for air and exhaust, methane is chosen as fuel and it is accepted as ideal gas, the combustion is complete, there is no NOx formation and the heat loss in the combustion chamber is 2% of the upper heat value of the fuel.

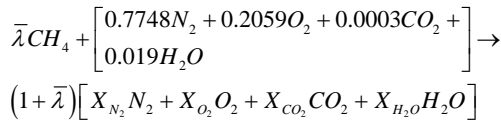
There is no heat loss in other devices and kinetic and

potential energy effects are not considered. In addition, the environmental conditions are taken as follows; $T_0 = 298.15$ K and $P_0 = 1.013$ bar, pressure loss for combustion chamber, recuperator and heat exchanger 5% and capacity for compressor $\dot{m}_1 = 91.4$ kg / s, heat exchanger $\dot{m}_v = 14$ kg / s saturated vapor pressure 20 bar, gas turbine net electric power 30 MW, combustion chamber fuel mass $\dot{m}_f = 1.64$ kg / s methane. The thermodynamic model and calculation procedure

Table 2. Exergy and exergy efficiency equations of each devices of the air preheated cycle [11, 14].

Devices	Exergy equations	Exergy efficiency
Compressor	$\dot{E}_{D,C} = \dot{E}_1 + \dot{W}_C - \dot{E}_2$	$\eta_{ex,C} = \frac{\dot{E}_{O,C} - \dot{E}_{I,C}}{\dot{W}_K}$
Recuperator	$\dot{E}_{D,R} = \dot{E}_2 + \dot{E}_5 - \dot{E}_3 - \dot{E}_6$	$\eta_{ex,R} = \frac{\dot{E}_{O,air,R} - \dot{E}_{I,air,R}}{\dot{E}_{O, eg,R} - \dot{E}_{I, eg,R}}$
Combustion chamber	$\dot{E}_{D,CC} = \dot{E}_3 + \dot{E}_{10} + \dot{E}_{13} - \dot{E}_4$	$\eta_{ex,CC} = \frac{\dot{E}_{O,CC}}{\dot{E}_{I,CC} + \dot{E}_{Fuel}}$
Turbine	$\dot{E}_{D,T} = \dot{E}_4 - \dot{E}_5 - \dot{W}_C - \dot{W}_T$	$\eta_{ex,T} = \frac{\dot{W}_{net,T} + \dot{W}_C}{\dot{E}_{I,T} - \dot{E}_{O,T}}$
Heat exchanger	$\dot{E}_{D,HE} = \dot{E}_6 - \dot{E}_7 + \dot{E}_8 - \dot{E}_9$	$\eta_{ex,HE} = \frac{\dot{E}_{Steam,HE} - \dot{E}_{Water,HE}}{\dot{E}_{I, eg,HE} - \dot{E}_{O, eg,HE}}$
All cycle	$\dot{E} = \dot{E}_{ph} + \dot{E}_{ch}$ $\dot{E}_{ph} = \dot{m} (h - h_0 - T_0 (s - s_0))$ $\dot{E}_{ch} = \frac{\dot{m}}{M} \left\{ \sum X_k \bar{e}_k^{ch} + \bar{R} T_0 \sum X_k \ln X_k \right\}$ $\eta_{ex} = \frac{\dot{W}_{net,T} + (\dot{E}_{Steam,HE} - \dot{E}_{Water,HE})}{\dot{E}_{Fuel}}$	

are given in Table 1 and Table 2 for the air preheated cycle. The combustion equation is taken as follows.



The cost of the main product is calculated in four steps in the economic analysis with the required income method. These are cost accounting and forecasting of the total investment, determination of economic, financial, labor and market input parameters for the detailed cost account, calculation of the total income needed and calculation of the product cost with these values. The CEPCI equipment index (CHEMICAL ENGINEERING PLANT COST INDEX) was used to find the current values of past device prices.

$$C_{EQ} = C_{ref} (2016CEPCI EQ.IN. / 1994CEPCI EQ.IN.) \quad (1)$$

There are three methods used for cost estimation of the purchased equipment: cost indices, cost estimating charts, and calculation effect of size on equipment. The last one is used in this study. For the overall system operating at steady state the cost balance is given as

$$C_{ref-year} = C_{ref} (\dot{E}_{net} / \dot{E}_{ref})^a \quad (2)$$

$$\dot{C}_{P,tot} = \dot{C}_{f,tot} + \dot{Z}_{tot}^{CI} + \dot{Z}_{tot}^{OM} \quad (3)$$

In this equation, Z is non exergy related cost rate, C is cost rate, f is fuel, CI is capital investment, P is product, OM is operating and maintenance and tot is total [1, 26, 27]. The details of the calculation can be found in literatur [1, 8].

RESULTS AND DISCUSSION

Table 3 shows the net work, net heat energy, loss of energy, compressor work, air and exhaust mole numbers, combustion chamber outlet temperature, for the air preheated cogeneration cycles. Also energy efficiency and energy balances are given.

Accordingly, as the amount of steam injected increases, the net work, the energy withdrawn from the boiler, the net heat energy, energy efficiency and combustion chamber outlet temperature are decreases for the sample, the air and the fuel air preheated cogeneration cycles.

In Figure 2, it can be seen that increasing the injected steam flow increases the electrical power of the systems. The increases the injected steam increase the flow rate entering the turbine, and the work obtained from the turbine are increased.

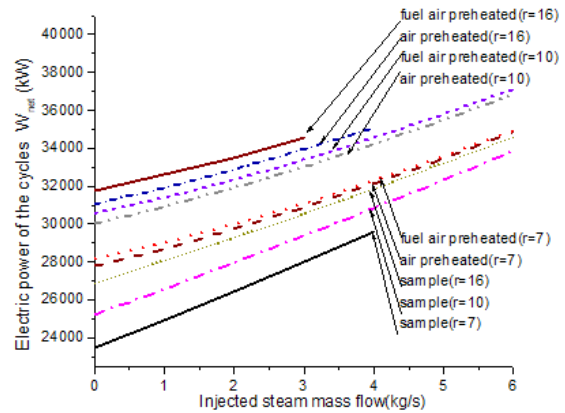


Figure 2. Variations of electric power of the cycles with steam injected mass flow. ($m_{fuel}=1,64$ kg/s, $m_{air}=91,3$ kg/s, $\eta_{isc}=\eta_{ist}=0,86$, $T_1=298,15$ K, $T_{rec,out}=850$ K, $T_{steam}=485,57$ K, $T_{eghaust}=426$ K).

In steam injected cycles, increasing the compressor compression ratio increases, the amount of the electricity. In some of the cycles, the curves are cut off at certain mass flow, since the heat energy required for the operation is not provided.

Figure 3 shows the change in the electric heat energy ratio of the systems with the injected steam flow at different compressor compression ratios. As the injected steam flow increases, the heat power decreases rapidly and the electric power increases rapidly. It is understood that the compression ratio is very effective in the ratio of electric heat energy to the air and the fuel air preheated cogeneration cycles.

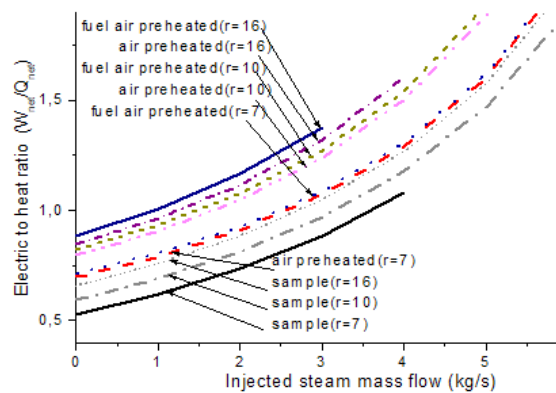


Figure 3. Variations of electric to heat ratio of the cycles with steam injected mass flow. ($m_{fuel}=1,64$ kg/s, $m_{air}=91,3$ kg/s, $\eta_{isc}=\eta_{ist}=0,86$, $T_1=298,15$ K, $T_{rec,out}=850$ K, $T_{steam}=485,57$ K, $T_{eghaust}=426$ K).

Table 3. Variations of steam injection mass flow with some parameters and the energy balance of the steam injected sample, air preheated and fuel air preheated cycles.

HHV		Sample cycle ($m_{air}=91.3$ kg/s)						
Steam(Kg/s)	Fuel En.(kW)	W_{net} (kW)	Q_{net} (kW)	Q_{egz} (kW)	CC Loss** (kW)	WC(kW)	CC outlet temp.(K)	I.Law Efficiency
0	91011	25166	42339	24369	1820	29675	1303	0,7415
1	91011	26513	38325	27046	1820	29675	1287	0,71216
2	91011	27908	34256	29727	1820	29675	1271	0,68281
3	91011	29342	30148	32408	1820	29675	1256	0,65347
4	91011	30809	26008	35090	1820	29675	1242	0,62412
5	91011	32300	21844	37771	1820	29675	1228	0,59477
6	91011	33809	17662	40453	1820	29675	1214	0,56542
Inlet En.=Outlet En. - Air En.(2663 kW)					Egzhaust Mol N.		Air Mol N.	
0	91011=91031				3,2891		3,1869	
1	91011=91040				3,34463		3,1869	
2	91011=91048				3,40014		3,1869	
3	91011=91056				3,45565		3,1869	
4	91011=91064				3,51116		3,1869	
5	91011=91072				3,56667		3,1869	
6	91011=91080				3,62218		3,1869	
HHV		Air preheated cycle ($m_{air}=91.3$ kg/s)						
Steam(Kg/s)	Fuel En.(kW)	W_{net} (kW)	Q_{net} (kW)	Q_{egz} (kW)	CC Loss** (kW)	WC(kW)	CC outlet temp.(K)	I.Law Efficiency
0	91011	29977	37526	24369	1820	29675	1519	0,74145
1	91011	30863	33967	27051	1820	29675	1498	0,7121
2	91011	31870	30286	29732	1820	29675	1479	0,6828
3	91011	32982	26501	32414	1820	29675	1460	0,6534
4	91011	34186	22624	35095	1820	29675	1442	0,6241
5	91011	35469	18667	37777	1820	29675	1424	0,5947
6	91011	36821	14643	40458	1820	29675	1407	0,5654
Inlet En.=Outlet En. - Air En.(2663 kW)					Egzhaust Mol N.		Air Mol N.	
0	91011=91029				3,28912		3,186897	
1	91011=91038				3,34463		3,186897	
2	91011=91046				3,40014		3,186897	
3	91011=91054				3,45565		3,186897	
4	91011=91062				3,51116		3,186897	
5	91011=91070				3,56667		3,186897	
6	91011=91078				3,62218		3,186897	
HHV		Fuel air preheated cycle ($m_{air}=91.3$ kg/s)						
Steam(Kg/s)	Fuel En.(kW)	W_{net} (kW)	Q_{net} (kW)	Q_{egz} (kW)	CC Loss** (kW)	WC(kW)	CC outlet temp.(K)	I.Law Efficiency
0	91011	30519	36984	24370	1820	29675	1542	0,7414
1	91011	31342	33487	27051	1820	29675	1521	0,7121
2	91011	32295	29861	29732	1820	29675	1501	0,68276
3	91011	33361	26122	32414	1820	29675	1481	0,65341
4	91011	34526	22283	35095	1820	29675	1463	0,62406
5	91011	35777	18359	37777	1820	29675	1445	0,59471
6	91011	37103	14359	40458	1820	29675	1428	0,56536
Inlet En.=Outlet En. - Air En.(2663 kW)					Egzhaust Mol N.		Air Mol N.	
0	91011=91030				3,2891		3,1869	
1	91011=91037				3,34463		3,1869	
2	91011=91046				3,40014		3,1869	
3	91011=91054				3,45565		3,1869	
4	91011=91062				3,51116		3,1869	
5	91011=91070				3,56667		3,1869	
6	91011=91078				3,62218		3,1869	

*%1,9 of the inlet air is accepted as steam and the steam in the egzhaust is accepted as condensed (HHV) so that the condensation energy of the steam in the air is taken into consideration.

**Combustion chambers heat loss is taken as % 2 of the HHV of the fuel.

In Figure 4, variations of the exergy efficiency of the cycles with injected steam rate are given. For the air and the fuel air preheated cogeneration cycles, as the injected steam flow increases, the exergy efficiency is decreases. In the case of the sample cycle, higher efficiency is obtained because higher temperature is reached at high compression ratios and efficiency decreases as the amount of injected steam increases.

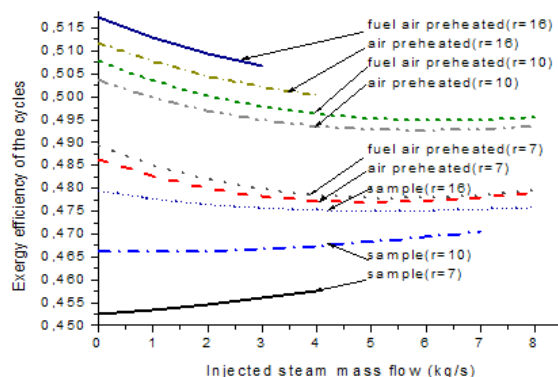


Figure 4. Variations of the exergy efficiency of the cycles with injected steam rate. ($m_{fuel}=1,64$ kg/s, $m_{air}=91,3$ kg/s, $\eta_{isc}=\eta_{ist}=0,86$, $T_1=298,15$ K, $T_{rec,out}=850$ K, $T_{steam}=485,57$ K, $T_{egzhaust}=426$ K).

As can be seen in Figure 5, as the injected steam flow increases, the obtained work increases, but reduces the artificial thermal efficiency of the systems.

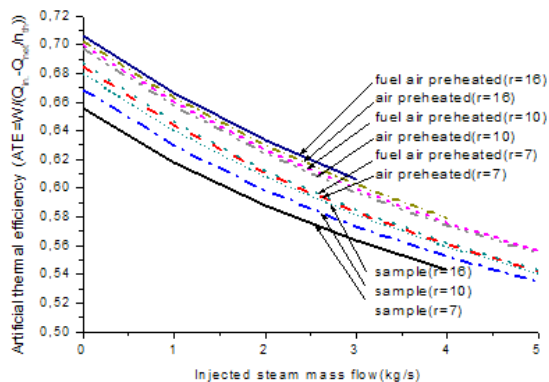


Figure 5. Variations of artificial thermal efficiency with injected steam rate. ($ATE=W/(Q_{in}-Q_{net}/\eta_h)$) ($m_{fuel}=1,64$ kg/s, $\eta_{isc}=\eta_{ist}=0,86$, $T_{rec,out}=850$ K, $T_{steam}=485,57$ K, $T_{egzhaust}=426$ K, $T_0=298,15$ K).

Figure 6 shows that as the injected steam flow increases at different compression ratios, the fuel energy gain rate of the systems decreases. That is why the heat energy obtained is thrown into the combustion chamber in the form of vapor. Decreasing the compression ratios also decreases the fuel-to-energy ratio.

In Figure 7, the variations of the cost of electricity produced by the systems at different compression ratios with

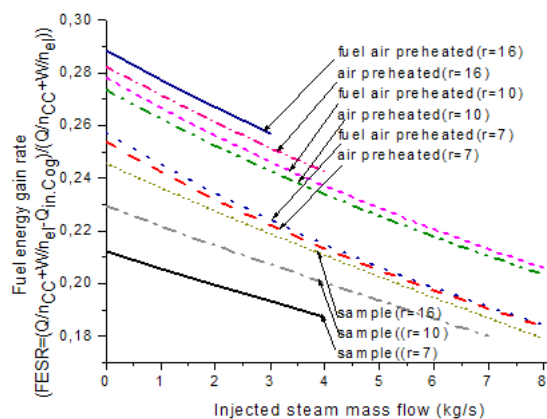


Figure 6. Variations fuel energy gain rate with injected steam rate of the compression rates. ($FESR=(Q/\eta_{cc}+W/\eta_c-Q_{in,Cog})/(Q/\eta_{cc}+W/\eta_c)$) ($m_{fuel}=1,64$ kg/s, $m_{air}=91,3$ kg/s, $\eta_{isc}=\eta_{ist}=0,86$, $T_1=298,15$ K, $T_{rec,out}=850$ K, $T_{steam}=485,57$ K, $T_{egzhaust}=426$ K).

the injected steam flow are given. Here too, curves are obtained for the operating conditions in which the cycles can run, and curves are cut off if they cannot. The cost of electricity generated by the cycles increases as the amount of injected steam increases. The amount of increase is similar in character.

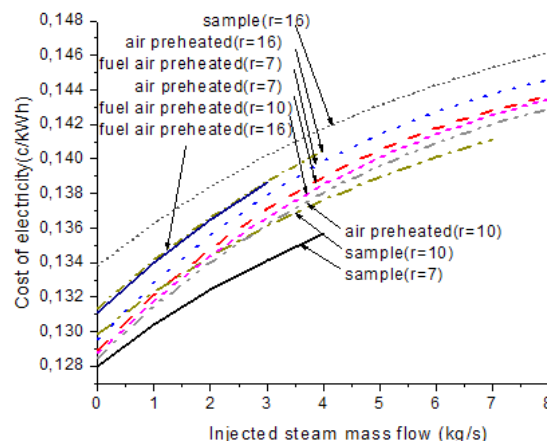


Figure 7. Variations of the cost of electricity with injected steam rate. ($m_{fuel}=1,64$ kg/s, $m_{air}=91,3$ kg/s, $\eta_{isc}=\eta_{ist}=0,86$, $T_1=298,15$ K, $T_{rec,out}=850$ K, $T_{steam}=485,57$ K, $T_{egzhaust}=426$ K).

CONCLUSION

Various cogeneration systems exist and in gas turbine cogeneration plants steam injection is made in the combustion chamber to increase the efficiency of the cycle and reduce nitrogen oxide emissions. As the amount of steam injected into the the sample, the air and the fuel air preheated cogeneration cycles increases, the net work, the energy withdrawn from the boiler and the number of moles exhausted increases, and the net heat energy, energy consumption and combustion chamber output temperature are decreases. Only a fraction of the heat

energy obtained from the exhaust gas emitted from the injected steam turbine is produced in the waste heat recovery device and then exhausted to the surroundings at 426 K. This reduces the amount of heat generated while increasing the amount of electricity generated.

At different compression ratios, it is found for all the cycles that increasing the amount of injected steam increases the electricity obtained. Since the injection of the steam obtained in the waste heat recovery device into the combustion chamber increases the flow rate entering the turbine, the work obtained from the turbine is increased. In some of the cycles, the curves are cut off at certain debts, since the heat energy required for the operation of the waste heat recovery apparatus is not provided.

As the injected steam flow increases, the heat power decreases rapidly and the electric power increases, so the electric heat energy rate increases rapidly. It is understood that the compression ratio is very effective in the ratio of electric heat energy to air and fuel air preheated cogeneration cycles.

In the air and the fuel air preheated cogeneration cycles, as the injected steam flow increases, the exergy efficiency is reduced. In the case of the sample cycle, higher efficiency is obtained because higher temperature is reached at high compression ratios and efficiency decreases as the amount of injected steam increases. But the sample cycle is worse than the other ones in all conditions.

As the amount of injected steam increases, the amount of fuel consumed for the work increases rapidly, which reduces the artificial thermal efficiency of the systems. As the injected steam flow increases at different compression ratios, the fuel energy gain rate of the systems decreases. The reason of that is the heat energy obtained is thrown into the combustion chamber in the form of vapor. Reduced compression ratios also reduce the fuel-to-energy ratio. Curves are obtained for the operating conditions in which the cycles can run, and curves are cut off if they cannot. The cost of electricity generated by cycles increases as the amount of injected steam increases. The amount of increase is similar in character.

References

1. Bejan, A., Tsatsaronis, G., Moran, M., 1996, *Thermal Design And Optimization*, Wiley Pub.
2. Boyce, M.P., 2002 *Handbook For Cogeneration And Combined Cycle Power Plants*, Asme Press, 42-220.
3. Cerqueira, S.A.G., Nebra, S.A., 1999, *Cost Attribution Methodologies In Cogeneration Systems*, *Energy Convers. Mgmt.*, 40, 1587-1597.
4. Çengel, Y.A., Boles, M.A., 2000, *Mühendislik Yaklaşımıyla Termodinamik*, Mc Graw Hill.
5. Çetinkaya, S., 1999, *Gaz Türbinleri*, Nobel Yayın Dağıtım.
6. El-Sayed, Y.M., Gaggioli, R.A., 1989, *A Critical Review Of Second Law Costing Methods- I: Background And Algebraic Procedures*, *ASME J. Energy Resour. Technol.*, 111.
7. Frangopoulos, C., 1993, *Application Of The Thermo-economic Functional Approach To The CGAM Problem*, *Energy Vol:19 No:3*.
8. Karaali, Rabi, Öztürk, İlhan Tekin, 2015, *Thermo-economic Optimization of Gas Turbine Cogeneration Plants*, *Energy* 80, 474-485.
9. Kehlhofet, R., Bachmann, R., Nielsen, H., Warner, J., 1999, *Combined Cycle Gas Steam Turbine Power Plants*, Penwell P.C.
10. Kwak, H.Y., Byun, G.T., Kwon, Y.H., Yang, H., 2004, *Cost Structure Of CGAM Cogeneration System*, *International Journal Of Energy Research.*, 28,1145-1158.
11. Kwon, Y.H., Kwak, H.Y., Oh, S.D., 2001, *Exergoeconomic analysis Of Gas Turbine Cogeneration Systems*, *Exergy, An International Journal.*, 1 (1) 31-40.
12. Lazzarato, A., Tsatsaronis, G., 2006, *SPECO: A Systematic And General Methodology For Calculating Efficiencies And Costs In Thermal Systems*, *Energy* 31, 1257-1289.
13. Lazzarato, A., Toffolo, A., Morandin, M., Spakovsky, M.R.V., 2010, *Criteria For The Decomposition Of Energy Systems In Local / Global Optimization*, *Energy* 35, 1157-1163.
14. Moran, J.M., Tsatsaronis, G., 2000, *The CRC Handbook Of Thermal Engineering*, CRC Press LLC., 15-109.
15. Özahi, E., Tozlu, A. and Abusoglu, A., 2017, *Thermodynamic Performance Assessment of Different Fluids in a Typical Organic Rankine Cycle for Usage in Municipal Solid Waste Power Plant*, *ACTA PHYSICA POLONICA A*, V. 132, No. 3-II, p:807-812.
16. Rosen, M.A., Dincer, I., 2003, *Exergy-Cost-Energy-Mass Analysis Of Thermal Systems And Processes*, *Energy Convers. Mgmt.*, 44, 1633-1651.
17. Spakovsky, M., 1993, *Application Of Engineering Functional Analysis To The Analysis And Optimization Of The CGAM Problem*, *Energy*, Vol:19, No:3.
18. Taner, T., Sivrioğlu, M., 2017, *A techno-economic & cost analysis of a turbine power plant: A case study for sugar plant*, *Renewable and Sustainable Energy Reviews* V. 78, p:722-730.
19. Tozlu, A., Abusoglu, A., and Özahi, E., 2017, *Thermo-economic Analysis and Assessment of Gaziantep Municipal Solid Waste Power Plant*, *ACTA PHYSICA POLONICA A*, V 132, No 3, p:513-517.
20. Tsatsaronis G., Moran, M.J., 1997, *Exergy Aided Cost Minimization*, *Energy Convers. Mgmt.*, 38.
21. Tsatsaronis, G., 1993, *Thermo-economic Analysis And Optimization Of Energy Systems*, *Progress Energy Combustion Sci.*, Vol:19-3.
22. Valero, A., Torres, C., Lozano, M.A., 1989, *On The Unification Of Thermo-economic Theories*, *AES Vol:9 ASME Book*.
23. Vieira, L., S., Donatelli, J., L., Cruz, M., E., 2004, *Integration Of An Iterative Methodology For Exergoeconomic Improvement Of Thermal Systems With A Process Simulator*, *Energy Convers. Mgmt.*, 45.
24. Wang, F.J., Chiou, J.S., 2002, *Performance Improvement For a Simple Cycle Gas Turbine GENSET-a Retrofitting Example*, *Applied Thermal Engineering*, 22.
25. Wilkinson, B.W., Barnes, R.W., 1993, *Cogeneration Of Electricity And Useful Heat*, CRC Pres.
26. <http://www.nyethermodynamics.com/trader/outprice.htm> (Ziyaret tarihi: 15 Kasım 2015)
27. <http://www.ere.com.tr> (Ziyaret tarihi: 5 Şubat 2015)

Rational Exergy Management Model for Effective Utilization of Low-Enthalpy Geothermal Energy Resources

Birol Kılıç¹  **Şiir Kılıç²** 

¹Başkent University, Bağlıca Campus 06810 Etimesgut, Ankara, TURKEY

²TÜBİTAK, Atatürk Bulvarı, 06100, Ankara, TURKEY

ABSTRACT

Within the broad range of sustainability and decarbonization efforts, energy and exergy-rational cities are becoming universally important. Within this context, both ORC systems, which are touted as primarily useful for utilizing low-enthalpy geothermal resources and heat pumps, which are considered as the primary tool for decarbonization are critically analyzed in this study. In this context, two cases regarding an ORC, which is used only for power generation without utilizing its waste heat and a heat pump operating on grid power, were examined and was concluded that they are not exergetically sustainable, if they operate as individual systems. This study instead developed an analysis model, which reveals with case studies and examples that a broad hybridization of combining ORC technology, heat pumps, absorption units, thermal storage, and other renewable energy resources, like solar and wind provides sustainable and exergetically rational design solutions. It is argued and verified that, within practical demand and supply constraints in the built environment, such hybrid systems lead to 4th generation district energy systems and beyond, like nearly-zero energy and exergy cities. In order to arrive such conclusions, new evaluation and rating metrics based on Rational Exergy Management Model were introduced. A novel nearly-zero energy and exergy design about a 20000-inhabitant town having geothermal energy potential at a production well-head temperature of 80°C is presented for a simplified purpose of demonstrating the algorithm of the new model This design incorporates ground-source heat pumps, waste heat utilization, cogeneration units, in addition to ORC system. Such an enrichment of the multiple systems even in a simplistic manner in an exergy economy cycle analytically reduces CO₂ emissions by about 66%, when compared to a conventional district energy system utilizing natural gas. Yet analyses have shown that results are sensitive upon design constraints and local conditions and concludes that the only option of achieving a truly sustainable solution in terms of exergy towards net-zero status is optimum bundling of the energy resources and systems on a case-by-case design with the main aim of balancing the supply and demand exergy.

Keywords:

ORC technology; Geothermal energy; Hybrid district energy system; Rational Exergy Management Model; CO₂ emissions responsibility; Heat pumps; Cogeneration; Thermal energy storage

INTRODUCTION

Based on the Rational Exergy Management Model, the objective of this study is to develop an analytical tool with new design, evaluation, and rating metrics for designing and analyzing hybrid energy systems and resources, including low-enthalpy geothermal energy towards achieving nearly-zero status of district energy systems, based on both energy and exergy performance of new establishments with

district energy systems. The main aim is to achieve maximum decarbonization efficiency in these establishments. Another aim is to resolve the conflict between decarbonization and high CO₂ content of the geothermal reservoirs in Turkey by reducing the unit CO₂ emissions per unit exergy output of the hybrid system, in addition of traditional methods of capturing and use of CO₂.

Article History:

Received: 2018/04/04

Accepted: 2018/04/12

Online: 2018/09/07

Correspondence to: Birol Kılıç,
Başkent University, Bağlıca Campus 06810
Etimesgut, Ankara, TURKEY
E-mail: bkilkis@baskent.edu.tr

In Turkey, most of the geothermal energy grabens are CaCO₃ based. This means that geothermal wells emit CO₂ that needs to be recaptured, which is considered as an expensive process in the sector. That is why most of the applications in Turkey directly release CO₂ to the atmosphere, nearly at a rate of 1 kg CO₂/kW-h. To be precise, this rate, symbolized by *u* in Equation 1, is almost equal to coal-based thermal plants [1]. CO₂ emissions per unit power generation are 0.034 kg CO₂/kW-h for Iceland, 0.33 kg CO₂/kW-h for Italy, and the world average is 0.122 kg CO₂/kW-h according to the recent studies of the World Bank in 2016 [2]. According to the same report this value, particularly for the Gediz graben in the Western Anatolia varies between 0.9 kg CO₂/kW-h and 1.3 kg CO₂/kW-h. Other publications also confirm these results [3]. For natural-gas, combined-cycle power plants this value is around 0.42 kg CO₂/kW-h (Based on an average First-Law Efficiency of 0.47 for the power generation in the plant and the CO₂ content of natural gas of 0.2 kg CO₂/kW-h lower heating value). This value for coal-base power plants is around 1.3 kg CO₂/kW-h [4, 5, 6]. In Equation 1, *u* is the unit CO₂ emissions per kW of electrical power generated, *E*.

$$u = \frac{\sum CO_2}{\sum E} \quad \{\text{kg CO}_2/\text{kW}_E\} \quad (1)$$

Equation 1 reminds us that the unit emission values, namely *u* are based only for power generation and therefore is not responsive for low-enthalpy geothermal energy resources, because their electric power generation capacity are limited or none and instead, they need to be utilized in the form of heat, or sometimes in the form of cold through absorption and most likely, through adsorption cycles. Probably that is why the waste heat of ORC systems are indeed wasted without employing it in useful applications in the field or in the city, because they are not recognized in Equation 1 nor appreciated in bank loans.

Fig. 1 further illustrates that only-electric ORC systems for example, may not be rational, especially from an exergetic point of view [7]. Fig. 2 exemplifies this condition better by comparing the ORC and District Energy bundle [7]. In this figure, options are either using ORC alone or directly using the geofluid in district heating. This example shows that, in many cases of low-enthalpy geothermal sources like below 100°C, it is better to utilize the geothermal energy as heat or cold (through absorption or adsorption cycle) rather than trying to generate power with such a low efficiency around 10% in practical terms. See Fig. 3 for several working fluids [8].

According to the example given in Fig. 2, exergy of ORC power output is only 0.08kW/kW while the exergy of the geofluid, which could be directly used for heating is 0.2 kW/

kW. The latter is definitely higher. A new criterion has been defined, which is named the Added Value, *AV*. It is a simple product of the First-Law efficiency, η_{ORC} or η_{DE} and the unit exergy, ε_E or ε_H of the power generation by ORC equipment or thermal output of the district energy system at a well-head temperature, T_K , respectively.

$$AV_E = \eta_{ORC} \times \varepsilon_E \approx \eta_{ORC} \quad , \text{or} \quad (2-a)$$

$$AV_H = \eta_{DE} \times \varepsilon_H = \eta_{DE} \times \left(1 - \frac{283}{273 + T_K}\right) \quad (2-b)$$

Here η_{ORC} is the First-Law efficiency of ORC in electric power generation ($\varepsilon_E \sim 1$ kW/kW) for a given well head temperature of the geofluid, T_K (See Fig. 3):

$$\eta_{ORC} = aT_K + b \quad (2-c)$$

Here, 283 K is the selected reference temperature, T_{ref} for the ideal Carnot Cycle. Equations 2-a, 2-b, and 2-c may be simultaneously solved for a critical T_{KCR} value, namely T_{KCR} . Such a solution is the positive root of the quadratic equation:

$$T_{KCR} = \frac{\left(1 - \frac{273a}{\eta_{DE}}\right) \pm \sqrt{\left(1 - \frac{273a}{\eta_{DE}}\right)^2 + 4 \times 273 \left(\frac{a}{\eta_{DE}}\right) \times \left(1 + \frac{b}{\eta_{DE}}\right)}}{2 \left(\frac{a}{\eta_{DE}}\right)} \quad (3)$$

In this Example, T_{KCR} is around 100°C. Below this critical temperature ORC system is not feasible. Above the critical temperature ORC is a better option. An even better option is to utilize the waste heat from ORC in a low-exergy district heating system at around for example 40°C.

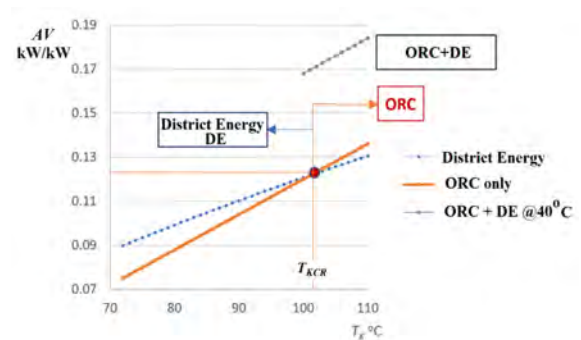


Figure 1. Exergy Rationality of Utilizing Low-Enthalpy Geothermal Energy for R123 Working Fluid [7]

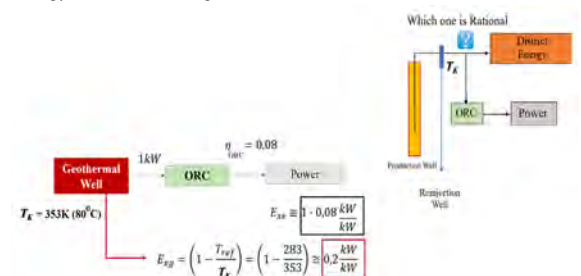


Figure 2. ORC and District Energy Dilemma [7]

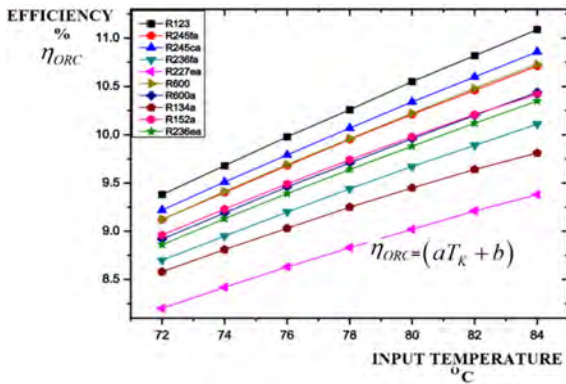


Figure 3. ORC Efficiencies for different working Fluids [8]

In this research, a new evaluation metric, which relates the thermal exergy and power exergy outputs of a geothermal system, named E_{XR} has been derived from the new exergetic approach. The argument of this approach is that the thermal output exergy (Numerator of Equation 4 must be at least 25% more than ORC output exergy):

$$E_{XR} = \frac{\left(1 - \frac{283}{(273 + T_K)}\right) \times \eta_H}{(aT_K + b) \times 1} > 2 \quad (4)$$

Low-enthalpy geothermal energy has about 30% share among different heat sources that drive ORC systems for electricity generation [9]. ORC market is rapidly increasing but their expansion mainly depends upon economic incentives, tariffs, and several subsidies [9].

Even today ORC market is relying on the economic benefits of selling the electrical energy based on tariffs and incentives [10]. There are few studies however, which look into their actual benefits, risks, and potential disadvantages from sustainability view at large. One such recent study has revealed that ORC units may not be ecologically sound if used in a stand-alone format and just generate electric power [11]. The same study has shown that ORC systems need to be bundled with other renewable energy resources, systems, and energy storage units in order to be environmentally acceptable from the exergy point of view [11]. In fact, there are few exergy analyses available in the literature that mainly focus on the operation of the ORC units and design without having a holistic approach, that is to say, its connection between the energy source and the demand in the built environment. In fact, without the Second-Law of Thermodynamics, it is not possible to identify and quantify the advantages and disadvantages of using stand-alone ORC units against different bundling alternatives with renewable energy systems.

Fig. 1 at the same time indicates that above a certain well-head temperature, ORC may indeed be a feasible solution, but a better solution is to utilize the so-called waste

heat. This is nothing but cogeneration and provides the first signals of hybrid energy systems, moving away from power-only solutions in order to reduce u . Such an application will definitely reduce the above mentioned unit CO_2 emission values. The remaining problem is how to incorporate the thermal output into the power-based equation above, because heat, cold, and power have quite different exergy. At this point the Second Law comes to the rescue such that the denominator of Equation 1 is modified in terms of exergy rather than energy:

$$u_x = \frac{\sum CO_2}{\sum E_{xE} + \sum E_{xH}} = \frac{\sum CO_2}{\sum E + \sum E_{xH}} \quad (5)$$

The sum of thermal exergy E_{xH} includes geothermal heat converted to cold by absorption or adsorption machines. The last term in Equation 5 is based on the widely accepted assumption that electric power has a unit exergy of 1 kW/kW (Actually 0.95 kW/kW at a reference temperature of 283K). Therefore, E_{xE} (Electrical Exergy of a given electrical energy) is replaced by E (Electrical Energy). Thanks to the exergy concept, this equation eliminates the exergy differences between heat and power, because itself is based on exergy and lets large heat and or cold energy potential (if utilized instead of wasted) to be recognized and incorporated in the same domain of exergy with electric power. By this new metric, firstly introduced in this article, namely u_x , high CO_2 emissions from low-enthalpy geothermal energy sources are automatically reduced below other conventional power plants, while these power plants generally do not utilize their waste heat. This new metric is an important incentive towards utilizing the waste heat in useful forms of many different types of applications-not only for geothermal power plants but also for all types of power plants. This is large scale cogeneration according to EU Directive 2004/8/EC [12]. This directive defines the efficiency requirements according to the First Law of Thermodynamics and calculates the primary fuel savings. Although heat and power are discriminated in this equation, it does not recognize the exergy differences in terms of the temperature of the heat provided. In order to resolve this issue Kilkis, S. and Kilkis B. have upgraded the fuel savings equation of the directive in terms of the Rational Exergy Management Efficiency (See Equation 9) [13].

Another important point is the fact that, geothermal potential in terms of thermal quantity, Q that contributes to the added value potential of the associated systems need to be recognized and adjusted according to the quality of geothermal energy potential in terms of exergy, which is defined in terms of the average enthalpy represented by the average reservoir well-head temperature. A new metric, J was defined:

$$J = \frac{E_{XH}}{A} = \frac{\left(1 - \frac{T_{ref}}{\bar{T}_K}\right) \times Q}{A} \quad (6)$$

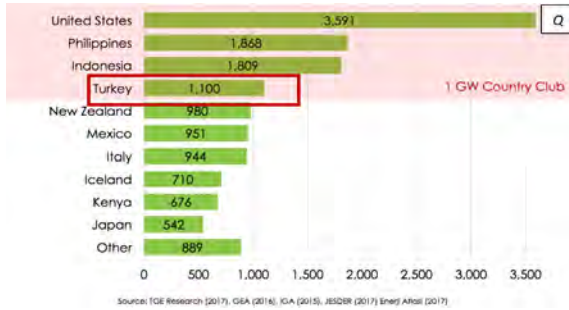


Figure 4. 1 GW Country Club Ratings Based on Reservoir Potential, Q [14]

Fig. 4 lists several countries with 1 GW installed capacity and above. This listing is according to the First Law ranking in terms of Q . In this list, Turkey ranks fifth in the World. However, if for example the estimated average \bar{T}_K value is 107°C (380K) and the geographic area of Turkey is $780,000 \text{ km}^2$, then the J value for Turkey is 0.36 kW/km^2 . If Equation 6 is applied to all countries given in the Table, then the ranking will definitely shift and the position of Turkey will be quite different.

$$J = \frac{E_X}{A} = \frac{(1,100 \text{ MW} \times 1000 \text{ kW/MW}) \times \left(1 - \frac{283}{380}\right)}{780000} = 0.36 \text{ kW/km}^2$$

Fig. 5 exemplifies the fact that Turkey is one of the countries in the list, which has a majority of geothermal reservoirs with low enthalpy. According to Fig. 5, the well-head temperatures in the province of Ankara ranges between 37°C (310K) and 56°C (329K). This means that the exergy of the geothermal reservoirs range between $(1-283\text{K}/310\text{K})Q$ and $(1-283\text{K}/329\text{K})Q$, namely $0.087Q$ and $0.14Q$. This means that the geothermal reservoirs in the province of Ankara the added value of useful work potential ranges only between 8.7% and 14% of the thermal reservoir, Q . This is an important step of evaluating of geothermal reservoirs in acknowledging the true quality of geothermal reservoirs instead of the quantity of the reservoirs.

Another metric is related to the investment cost, which is broken to electric power, heat, and cold power services In Equation 7, i is the unit investment cost in terms of Turkish Lira, TL investment per unit design power, unit exergy, heating degree hours (HDC), and cooling degree hours, CDH (If included in the project). In Equation 7, i is the investment index. I_E , I_H , and I_C are the original investments in Turkish Lira, which are attributable to electric power, heating, and cooling services, respectively to be delivered to human po-

pulations receiving power, heat, and cold services N_E , N_H , and N_C , respectively in the district energy system.

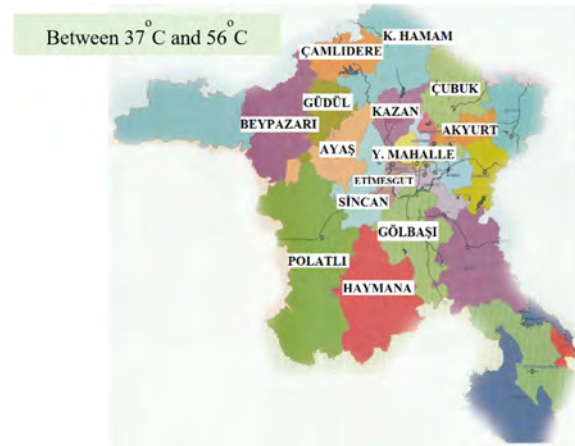


Figure 5. Low Enthalpy Geothermal Energy in the Province of Ankara [15]

$$i = \frac{I_E}{\left[N_E \times P_E \times 1 \times (HDH + CDH) \right]} + \frac{I_H}{\left[N_E \times P_H \times \left(1 - \frac{T_{OH}}{T_K}\right) \times HDH \right]} + \frac{I_C}{\left[N_C \times P_C \times \left(1 - \frac{T_{OC}}{T_K}\right) \times CDH \right]} \quad (7)$$

Here, P stands for the design capacities of power, heat, and cold services. HDH and CDH are the heating and cooling degree-hour values, respectively. Lower the i value is, better the economical investment is. The last term drops if any cooling service is not provided in the district energy system. Investment, I is rated also for the quality of the services provided in terms of the ideal Carnot Cycle. T_{OH} and T_{OC} are the design outdoor temperatures for winter and summer seasons, respectively. The unit exergy of electricity is taken 1 kW/kW .

LITERATURE SURVEY

Current trend is to isolate any unit from the entirety of the applied system and evaluate it alone. For example, ORC units are sold based on the simple condition of economy to the customer or the power company in terms of electricity prices and subsidies if available and applicable to that particular system. The same also holds true for heat pumps [16]. Investment pay backs and bank loans etc. are always calculated in terms of the simple economy of the customer or the power company. These approaches do not reveal the real performance of the unit and real potential contributions and added value to the energy eco-

nomy at large and the environment, when coupled to the energy input side and the energy supply side (application).

Another current advancement is the development of geothermal heat pumps in smart cities and communities [17]. However, this project focuses on shallow geothermal heat pumps driven by grid electricity. Therefore, this project needs to be upgraded by novel, integrated solutions, like the ones presented earlier by the Authors [18,19].

Reza Rowshanzadeh [20] has shown that ORC technology has a very wide field of applications and gave a case design for one of the clients of the KTH University in Sweden and pointed out the need for an exergy analysis. Sun, W., Yue, X., and Wang, Y. have investigated the suitable application conditions of ORC-ARC (Absorption Refrigeration Cycle) and ORC-ERC (Ejector-Refrigeration Cycle) and reported comparative results in terms of their exergy analyses [21]. In their paper, Marini, A., Alexandru, D., Grosu, L. and Gheorghian, A. [22] have analyzed an ORC system driven by solar energy with vacuum-tube collectors, which provides electrical power for a building. They simulated the performance for different working fluids based on the objective of minimizing the exergy destructions in the system. They concluded that such an ORC system may be exergetically feasible if a careful optimization is carried out. A recent study by Kilkis, B. and Kilkis Siir [15] have complemented the idea that the First Law of thermodynamics is not sufficient to evaluate ORC systems for best performance and environmental sustainability, especially when different renewable energy systems and systems are bundled to form a hybrid system. For example, the electric power input to GSHP is utilized to supply heat with a given First-Law *COP* at given operating conditions. But the input side and the supply side have different exergy.

THEORY

Review of the Rational Exergy Management Model

Referring to the *Rational Exergy Management Method* (REMM), developed by Şiir Kilkis [15, 21], it is possible to quantify the exergetic advantages that may also be directly translated to avoidable CO₂ emission calculations one may compare direct geothermal heating versus geothermal ORC power generation also. Fig. 6 and 7 show the so-called *Exergy Flow Bars*, respectively [23].

In Fig. 6, exergy destruction (ϵ_{des}) takes place both in upstream and downstream. Because exergy is also destroyed upstream, based on ideal Carnot Cycle, the following equation is used to calculate the *REMM Efficiency*, ψ_R [23, 24]:

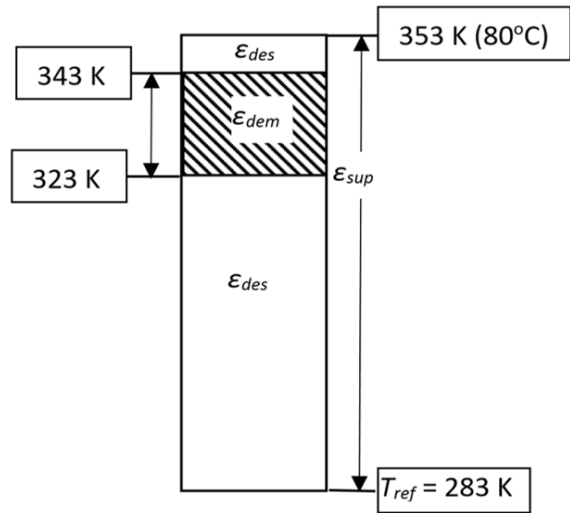


Figure 6. Geothermal District Heating

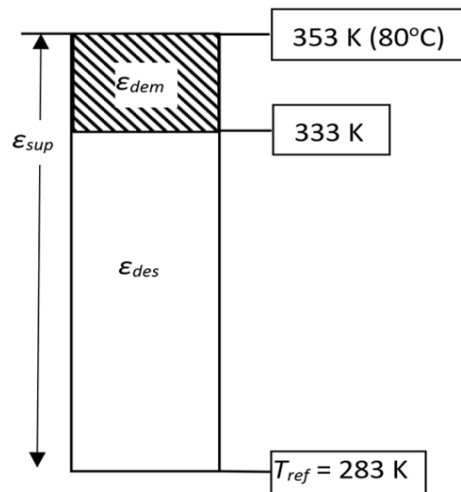


Figure 7. Power Generation with ORC [23]

$$\psi_R = \frac{\epsilon_{dem}}{\epsilon_{sup}} = \frac{\left(1 - \frac{323}{343}\right)}{\left(1 - \frac{283}{353}\right)} = 0.294 \quad (8)$$

Here, ϵ_{dem} represents the demand exergy of the district heating system between 60°C and 40°C for Low-Exergy buildings connected to the system. Another feature of REMM is the ability of identifying the exergetic effect of the final application. The final application in this case is comfort heating say for example at 20°C indoor air temperature in buildings. Then the ϵ_{dem} term is replaced by $(1-283/293)$. In this case ψ_R reduces to 0.172.

Fig. 7 shows the Exergy Flow Bar for ORC case for power generation. The un-utilized ORC outlet heat is taken to be at about 60°C (333 K). Because practically no exergy destruction takes place upstream, the following equation is used this time [23]:

$$\psi_R = 1 - \frac{\varepsilon_{des}}{\varepsilon_{sup}} = 1 - \frac{\left(1 - \frac{283}{333}\right)}{\left(1 - \frac{283}{353}\right)} = 0.243 \quad (9)$$

REMM shows that direct geothermal heating is more exergy-rational than just power generation with ORC without other *Geotherm* model applications, which are shown in Fig. 8 and 10.

Optimization Model of Hybrid Thermo Electric Systems- Exergetic Dilemma

The objective of this study was to develop a compound optimization model with a single operational variable, namely the heat supply temperature, T_{out} to a heat demanding building, which is shown in Fig. 8. According to this study, T_{out} must be collectively optimized for a given building heat load, Q_H for a required indoor air comfort temperature, T_a , which is expressed by Equation 10 (See also Fig. 8). Here, the heating demand is satisfied by a certain set of heating equipment installed into the building. The equipment performance is characterized s and n . The equipment heat output is dependent on T_{out} . Because Q_H is a given input parameter in this model, it is an inequality constraint of optimization. The objective of this new optimization problem is to maximize the total exergy output of the geothermal reservoir at a well head temperature, T_K . Total exergy output is the sum of the electric power exergy, E_{XE} delivered by the ORC unit operating at a First-Law Efficiency of $\eta_{ORC}(T_K)$ and the thermal exergy supplied to the building, E_{XH} . This objective comprises the following

- ψ_R is to be maximized (Equation 10).
- Compound CO_2 emissions is to minimized (Equation 12),
- COP and COP_{EX} are to be maximized (Equations 11 and 13)
- Split of the geothermal energy between an ORC unit (X) to produce electric power at a conversion efficiency, η_{ORC} and $(1-X)$ to supply heat to the building via the GSHP.

These individual objectives may be combined to a grand objective functions with weighing functions to be determined by the designer.

$$Q_H = s(T_{out} - T_a)^n \quad (10)$$

$$COP = a - b(T_{out} - T_K) - s' \left(1 - \frac{T_K}{T_{out}}\right) \quad (11)$$

$$CO_2 = \left[\frac{c_f}{\eta_I \eta_T} \left(\frac{Q}{COP} + E \right) \right] (2 - \psi_R) \quad (12)$$

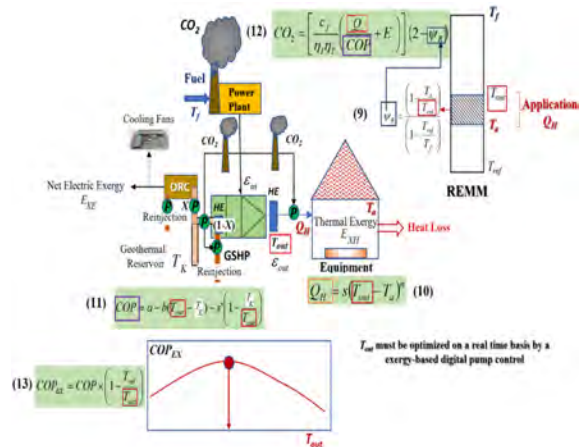


Figure 8. Second Law Model for Low Enthalpy Geothermal Source and a Temperature-Peaking Ground-Source Heat Pump [25]

Heat Pump Performance

According to Fig. 8, all performance variables are related to T_{out} . For example, Q_H of a given indoor comfort equipment is directly proportional to T_{out} , while the Rational Exergy Management Exergy, ψ_R is inversely proportional to T_{out} . Furthermore, CO_2 emissions responsibility of the geothermal system, which runs on grid power to drive the circulation pumps has a more complex dependence on T_{out} . For example, in order to decrease the difference between the inlet and outlet temperatures of the heat pump volumetric flow rate needs to be higher. This increases the power need for the circulation pumps and consequently CO_2 emissions responsibility increases. But at the same time COP of the heat pump increases resulting on less power demand for the compressor of the heat pump. On the other hand, if the temperature difference becomes too small the exergy of the output heat at a very low T_{out} decreases. This whole complexity and the conflicting relations show that T_{out} needs to be optimized.

In this study, the performance of the heat pump is expressed in terms of COP_{EX} :

$$COP_{EX} = COP \times \frac{\varepsilon_{out}}{\varepsilon_{in}} = COP \times \frac{\left(1 - \frac{T_{ref}}{T_{out}}\right)}{\varepsilon_{in}} \quad (13)$$

In Equation 13, ε_{in} is the unit exergy of electricity supplied to the heat pump by the power plants through the grid (1kW/kW). It seems that heat pumps play an important role in such clustered, hybrid renewable energy systems and equipment. Furthermore, Fig. 8 shows that an exergy base is crucial.

For a fixed (given) temperature, T_K at the well head of the geothermal reservoir, when T_{out} increases the temperature difference, ΔT between the heat pump inlet temperatu-

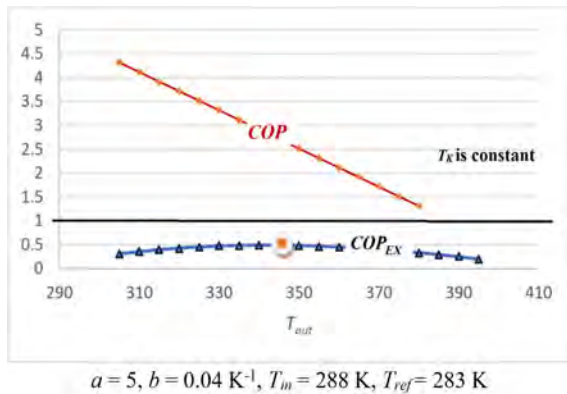


Figure 9. A Sample Variation of COP and COP_{EX} with T_{out} [25]

re (T_K) and the outlet temperature (T_{out}) increases. Consequently, the COP of the heat pump decreases. But at the same time, the output unit exergy increases while T_{out} increases (See Fig. 8 and Equations 11 and 13). These equations may be used to determine the maximum COP_{EX} for an optimum T_{out} . According to Fig. 9, although there is a slight maximum for COP_{EX} , its value is below 1. This means that COP of commercial heat pumps available today need to be higher, in terms of higher a values and smaller b values. Fig. 9 shows a sample variation of T_{out} [25].

Distance Constraint

Another constraint for district energy systems, DE is the maximum allowable distance between the geothermal source and the district location, namely L_{max} [26]. Height of the buildings in a settlement for a given population determines the L_{max} . In District Energy (DE) systems, the hydronic piping, namely the circuit length has an exergetic and financial limit. Exergetic limit is the requirement that the exergy demand (electric) associated with the pumping energy consumption must be only a small portion of the thermal exergy delivered to the district. Water distribution requires substantial pumping power and piping network is energy/exergy intensive both in embedded and operational forms. Depending upon the amount of thermal power of different forms to be distributed, there are limits on the maximum piping length. Equation 5-a was developed for heating.

$$L_{max} = a_o + \left(\frac{Q}{1000}\right)^m \times \left(\frac{\Delta T}{20}\right)^{1.3} \quad \left\{ \begin{array}{l} Q > 1000 \text{ kW}_H \\ \Delta T \leq 30^\circ\text{C} \end{array} \right. \quad (14)$$

Q_H is the useful thermal power to be transmitted (kW), ΔT is the supply return temperature difference, L_{max} is the farthest point that a closed thermal circuit may feasibly reach (km), a_o is an empirical constant, which is generally taken 0.6 km. The power m depends on the temperature, thus exergy of the heat supplied. T_{ref} is 283.15 K. 333.15 K is the traditional supply temperature.

$$m = 0.6 \times \left(\frac{\left(1 - \frac{T_{ref}}{T_K}\right)}{\left(1 - \frac{T_{ref}}{333.15}\right)} \right)^{0.33} \quad \{\text{For heating}\} \quad (15)$$

If cold water is circulated for a cooling demand then:

$$L_{max} = a_o + \left(\frac{Q}{1000}\right)^m \times \left(\frac{\Delta T}{10}\right)^{1.3} \quad \left\{ \begin{array}{l} Q > 1000 \text{ kW}_H \\ \Delta T \leq 30^\circ\text{C} \end{array} \right. \quad (16)$$

$$m = 0.6 \times \left(\frac{\left(1 - \frac{T_{ref}}{T_f}\right)}{\left(1 - \frac{T_{ref}}{282.65}\right)} \right)^{-1.23} \quad \{\text{For cooling}\} \quad (17)$$

CIRCULAR GEOTHERMAL SYSTEM MODEL, GEOTHERM

In order to improve the sustainability awareness in geothermal and ORC industry, a new concept was developed. This concept comprises the idea of combining ground heat and geothermal energy in a circular exergy flow. The concept in heating mode is shown in Fig. 10.

Ground Heat, Geothermal Energy, and Sustainable Systems

Following from the production well to the re-injection well, each unit in the circular exergy flow was analyzed in terms of their expected performance values. Then the following overall performance results (Total output) were obtained:

$$\begin{aligned} \text{Total Output} &= (0.62 \text{ kW}_H @ 55^\circ\text{C} + 0.34 \text{ kW}_H @ 90^\circ\text{C} \\ &\quad + 0.04 \text{ kW}_H @ 35^\circ\text{C} \text{ (for preheating of DHW)}) \\ &= 1 \text{ kW}_H \text{ thermal} \\ &\quad + 0.348 \text{ kW}_E \text{ electric} \end{aligned}$$

If the saved natural gas from district heat, which is later consumed in the poly-generation unit is not considered, then the gross COP of the circular geothermal loop is 1.348 kW/1 kW of geothermal power input. First-Law COP is greater than one, because ground heat is utilized in the GSHP in addition to the geothermal energy. $COP = 1.348$.

In other words, starting from a unit geothermal power at 80°C , the circular geotherm provides 0.348 kW of electric power and 1 kW of thermal power at different supply temperatures. This output favorably compares with 0.08 kW of electric power supplied by the ORC unit without reject heat recovery and 1 kW of thermal power at 80°C supply, if the geothermal power is utilized in the district in the form of heating only (Table 2). For electricity, ϵ_m in may be taken 1 kW/kW. T_{ref} is the environment reference temperature, in this case the average ground temperature (283K).

$$COP_{EX} = \frac{0.62 \times \left(1 - \frac{283}{328}\right) + 0.34 \times \left(1 - \frac{283}{363}\right) + 0.04 \times \left(1 - \frac{283}{308}\right) + 0.348 \times (1)}{1 \times \left(1 - \frac{283}{353}\right) + (0.62 / 0.8) \times \left(1 - \frac{283}{2000}\right)}$$

$$= 0.59$$

If only a simple ORC unit would be used, then COP_{EX} would be 0.092.

This Circular Geotherm Model comprises the following units:

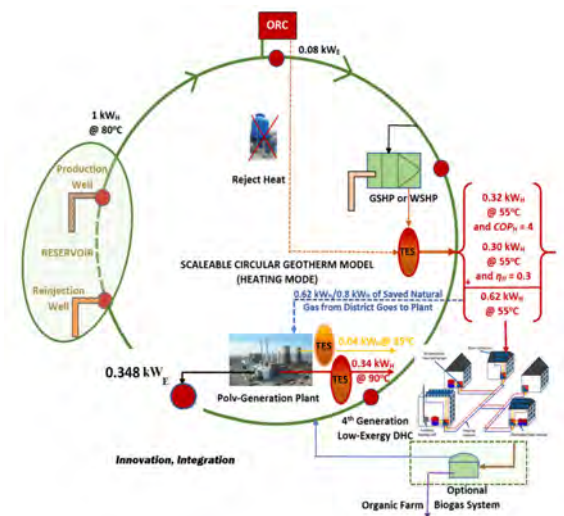


Figure 10. Combined Heat and Power in Circular Geotherm System: Heating Mode

- Geothermal Well(s),
- ORC,
- GSHP,
- District Energy Distribution and Collection System,
- Poly-Generation System,
- Biogas System (Optional), and
- Re-injection well(s).

Geothermal heat drives the ORC system. The electric power generated by the ORC drives the Ground-Source Heat Pumps (GSHP). Heat generated by the GSHP is utilized in the district. This heat is supplemented by the reclaimed reject heat from the ORC system. Buildings in the district are low-exergy type, which permit low temperature heating and high temperature cooling (Cooling Mode is not shown above). For the modeling purposes, the natural gas saved by replacing the heat provided by the ORC system and the GSHP, which otherwise would be spent in conventional boilers for heating purposes, is assumed to be utilized in a local poly-generation system, which generates both heat and electric power. Heat generated is of higher exergy at 90°C and is utilized in the district energy system while the domestic hot water, preheated by the waste heat from

the poly-generation system is temperature peaked. Table 1 shows a summary of the performance and compares with other systems.

These results further emphasize that, if a composite index that combines the quantity and quality features of the systems is used. This composite index being developed herein is *Composite Rationality Index*, C_R . This index gives

Table 1. Comparison of the Circular Geotherm with Natural Gas and ORC only Case.

System	Output			
	Electricity	Heat at 90°C	Heat at 55°C	Heat at 35°C
Circular Geotherm	0.348 kW _E	0.34 kW _H	0.62 kW _H	0.04 kW _H
DH with NG			0.775 kW _H	
ORC only	0.08 kW _E			

equal importance to the First and Second Laws of Thermodynamics, namely the First-Law Efficiency and REMM Efficiency. The same expression may also be repeated for applications involving COP .

$$C_R = \eta_I \times \psi_R \quad \text{or,} \quad (18)$$

$$C_R = COP \times \psi_R \quad (19)$$

Practical values of C_R in geothermal district energy applications may vary between 0.15 and 0.60. One finds the C_R value from Equation (18) for geothermal district heating and ORC power-only options to be 0.19 and 0.019, respectively. Here, η_I for district heating is taken 0.65 (net after parasitic losses) and for ORC is taken 0.08, respectively. This further shows that power-only ORC system may not be preferable in today's practical conditions and available equipment. This methodology, when applied to the Geotherm Model, further reveals its advantages. In Fig. 10, minor exergy destruction in the Circular Geotherm model in heating are neglected. Then:

$$\psi_R = 1 - \frac{\varepsilon_{des}}{\varepsilon_{sup}} = 1 - \frac{\left(1 - \frac{283}{293}\right)}{\left(1 - \frac{283}{353}\right)} = 0.827$$

and from Equation 19:

$$C_R = COP \times \psi_R = 1.348 \times 0.827 = 1.114$$

After comparing this result with geothermal district heating only case with $C_R = 0.19$, the CO_2 reduction potential ratio R from the carbon stock may also be compared according to REMM:

$$R = \frac{(2 - C_R)_{\text{district heating}}}{(2 - C_R)_{\text{geotherm}}} = \frac{2 - 0.19}{2 - 1.114} = 2.04 \quad (20)$$

This calculation shows a double advantage of potential CO_2 reduction from the carbon stock in the built environment.

The major parameter in this achievement is due to the high C_R value obtained in circular geotherm model. The same comparison with power-only ORC case with $C_R = 0.09$ shows that Geotherm Model has about 2.15 times higher potential.

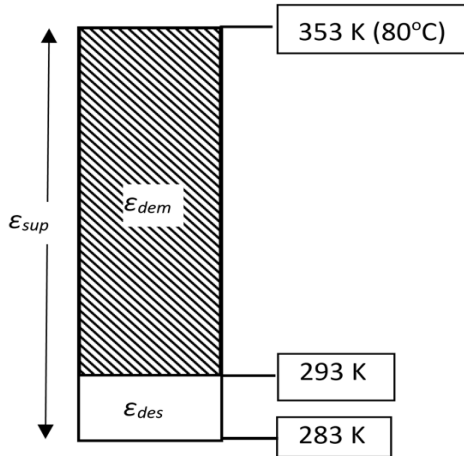


Figure 11. GEOTHERM Case

In Fig. 11, each kW_H of geothermal power and each 0.775 kW_H of the replaced natural gas from original boilers of the district returns to the energy stock by 1 kW_H of thermal power and 0.348 kW_E of electric power. If the geothermal heat is used just in an ORC system, only 0.08 kW_E will be generated and according to the above equation, with a COP_{EX} of 0.092. The *Circular Geotherm* shown above makes use of the ground heat through the GSHP and a complete energy and exergy cycle is obtained, while all types of waste heat are also utilized. Cycle starts at geothermal production well head and ends at the reinjection well. Thermal storage systems suited to two sets of exergy is used to match the loads and shave off the peak loads. A biogas system is an option using municipal wastes.

Biogas is mixed with natural gas saved from the boilers. Electric power generated by the poly-generation system is fed to the district. Optional solar and wind energy systems in the district contribute to peak loads with thermal storage. The entire collection of systems operates in a cascaded form, like a large heat pump. This system couples and mobilizes ground thermal energy with geothermal energy. In small applications, the evaporator side of the heat pumps may be coupled to PV systems (if this option is used in district buildings) to absorb the heat collected by PVs, which further improve the COP of the GSHP units. However, the flow rate needs to be dynamically optimized according to instantaneous solar insolation, heat demand, and other operating conditions, in order to maximize the total exergy output (Power and heat) of the PVT system [27, 28]. If there are more

than one system with multiple exergy connections, then Equation 21 is used [23].

$$\bar{\psi}_R = \frac{\sum_{i=1}^u \sum_{j=1}^v \psi_{Ri-j} E_{xi-j} / \eta_{i-j}}{\sum_{i=1}^u \sum_{j=1}^v E_{xi-j} / \eta_{i-j}} \quad (21)$$

For thermal links between two nodes $i-j$, E_{xi-j} is the simple product of Q_{i-j} and $(1-T_{ref}/T_i)$ by definition. For power links if electricity is used in electrical applications (electric to electric), ψ_{Ri-j} may be assumed to be approximately 1.

Other Features

- The same circular model may be applied to other sources of continuous heat, like waste heat from an industrial plant, provided that the supply temperature is equal to or higher than 80°C ,
- It is suitable to 4th generation district energy systems (4DE),
- This model represents an integrated, compound power and heat system at large,
- The model may be applied to a single building and scaled up to large district energy systems.
- May be combined with hydrogen economy cycle,
- In terms of exergy, the district may be and in fact should be equipped with exergy meters in order to establish a fair distribution of costs to individual customers
- The Model is equally applicable to district cooling. In this case, cold storage and absorption/adsorption units are also used. See Fig. 12 for a simplified explanation.

EVALUATION AND RATING METRICS

New Metrics

Table 2 lists the new metrics, which were especially developed in this study for rating low-enthalpy geothermal applications. In this table there are thirteen metrics, which rate different aspects of the geothermal system from a holistic point of view.

$$E_{XD} = \frac{E_{XTOT}}{n_D} = \frac{E_{XE} + E_{XH}}{n_D} = \frac{E + E_H \left(1 - \frac{T_{ref}}{T_{out}}\right)}{n_D} \quad (22)$$

The number of equivalent dwellings in the district, n_D , is based on hypothetical 100m^2 flats.

In addition to the above metrics, the following pay-back periods may also be calculated and used for additional evaluation:

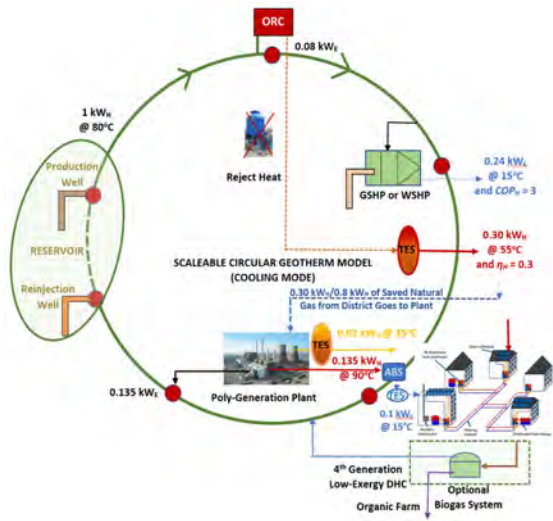


Figure 12. Combined Heat and Power in Circular Geotherm System: Cooling Mode

Table 2. Metrics for Evaluating Hybrid Geothermal Systems with Low-Enthalpy Sources.

Metric	Explanation (Equation Number)	Comments and Criteria
AV	Equations 2-a and 2-b, Added Value Index	>0.3
E_{XR}	Equation 4	>2
u_x	Equation 5	< 0.1kg CO ₂ /kW-h
J	Equation 6	Higher is better
i	Equation 7	Minimize
C_R	Equations 18 and 19 Composite Rationality Index	>1
$\bar{\Psi}R$	Equations 8 and 9, Rational Exergy Management Efficiency	Maximize
R	Equation 20, CO ₂ Reduction Potential Ratio	>1.5
E_{XD}	Equation 22, kW/kW/number of residences	Minimize
T_{KCR}	Equation 3	Minimize
nZED	Nearly-zero Energy District	$\psi_R \geq 0.80$
nZEXD	Nearly-zero Exergy District	$\psi_R \geq 0.70$

- CO₂ payback according to embedded CO₂ of material and construction,
- Exergy payback according to embedded exergy of material and construction,
- Energy payback according to embedded energy of material and construction,
- Investment payback according to the tariffs subjected to the service subscribers in the district.

All pay-back periods are important, yet in low-enthalpy geothermal systems CO₂ payback especially in Turkish geothermal fields with high CaCO₃ content is critical and must be prioritized in the rating process. Investment returns are also a crucial, because most of the equipment like ORC units get larger and costlier due to lower efficiencies. However, these statements should not mean that exergy and energy paybacks are less important. They influence CO₂ payback and a sustainable economy and grow they are

also very important. In essence all these payback definitions must be considered together.

Earlier Metrics

For general geothermal systems, without any distinction between low or high-enthalpy geothermal systems certain rating parameters were defined. For referencing purposes, they are listed in Table 3.

SAMPLE DESIGN STUDY

A new settlement of 20000 inhabitants in the suburbs of Ankara has low-enthalpy geothermal sources at 80°C well-head temperature. The reservoir has sufficient potential to meet the loads. In order to explain the algo-

Table 3. Earlier Metrics Defined by the Authors [29, 30].

Metric	Explanation (Equation Number)	Definition
GE	U/M , U is the thermal energy claimed in unit time at maximum sustainable geothermal fluid flow rate. M is the mass of geofluid spent in unit time at maximum sustainable geothermal fluid flow rate.	Geofluid Effectiveness
RDR	f (heat extraction rate-natural recharge rate-re-injection rate).	Reservoir Decline Rate
OF	Amount of equipment oversizing in order to match supply and demand unit exergies.	Equipment Oversizing Factor
GSE	Ratio of the district capacity (C_d) in terms of the number of equivalent residences without temperature peaking or equipment oversizing to the district capacity with both temperature peaking and equipment oversizing.	Geothermal System Effectiveness
CBUC	Capital Cost/ C_o	Common-base Unit Capital Cost

rithm of the new model, biogas system, wind and solar energy systems, and thermal storage are excluded in this simplistic conceptual design example. Geothermal wells supply heat to the ORC system. The ORC system delivers electricity to the ground-source heat pumps, which generate heat at 55°C to the buildings. In order to bring the design to a common base of comparing the district with a natural gas-based central DE system, the natural gas saved from the district heating system by replacing it with heat supplied by the heat pumps, CHP system is included to the calculations. Power and heat at 90°C is supplied by the CHP system. Power is directly delivered to the district. Part of the heat is delivered to the absorption cooling machines (ABS) first in order to satisfy the coincident cooling loads in the district. Reject heat at 35°C is mixed with the CHP output in order to deliver the heat to the district at the same temperature with the GSHP output. This is not the most feasible solution indeed. The Rational Exergy Management Efficiency would be better if additional useful work was obtained in a process like agricultural or industrial drying in the vicinity of the district for reducing the supply temperature for the

thermal grid in the district and utilizing the reject heat separately in a low-temperature application like greenhouse heating. Inputs for coincident design loads of the district with estimated respective diversity applications, are given in Table 4. Fig. 13 gives the sample design that meets the design loads.

RESULTS AND DISCUSSION

Performance Predictions

$\bar{\psi}_R$ is calculated from Equation 21 and the corresponding variables are tabulated in Table 5. Results show that this sample design has a $\bar{\psi}_R$ value of 0.86. Comparing this application with a conventional district heating system with natural gas boilers, with $\bar{\psi}_R$ value of 0.11,

Table 3. Earlier Metrics Defined by the Authors [29, 30].

Load	Capacities
Electrical Load	21000 kW _E
Heating Load	52000 kW _E
Cooling load (Sensible)	8000 kW _C

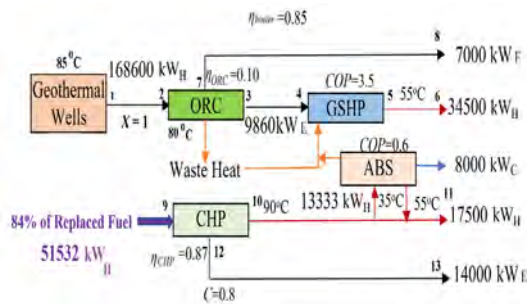


Figure 13. Conceptual System for the new settlement (X=1)

Table 5. Results for the Sample Design Study. COP=3.5, Q_{s,e}/η_{s,e}=34500 kW.

Node	T _i	T _j	ψ _{Rij}	Q _i /η _{ij}	E _{xij}	Numerator of Equation 21	Notes
i-j	(K)	(K)		(kW)	(kW)	(kW)	T _{ref} = 283 K
1-2	358	353	0.95	168600	35321.23	33433.43	
2-3	na	na	0.90		9860	8913.44	T _E = 313 K
3-4	na	na	1.00		9860	9860.00	
4-5	na	328	0.48	9860	1352.744	649.56	
5-6	328	323	0.90	34500	4733.232	4269.38	Demand at 50°C
6-6	dummy				0	0.00	
7-8	na	na	1.00	na	7000	7000.00	
9-10	2200	363	0.26	51532	11356.91	2907.37	
10-11	363	328	0.62	24907	3417.12	2125.45	
12-13	na	na	1.00		14000.00	14000.00	
13-14	363		0.92	13333	2938.40	2703.33	T _C is 15°C
14-14	dummy					0.00	
					99839.64	85861.96	
					Σ	Σ	
						0.86	ΣEq. 21/ ΣE _{xij}

which is calculated from the exergy flow bar shown in Fig. 14. The return water temperature in the district is 343K.

Then, referring to the last term in Equation 20, it is understood that the sample design has a potential of reducing CO₂ emission responsibility by 65.8%:

$$[(2-0.11)/(2-0.86)-1] \times 100 = 65.8\%$$

Sensitivity Analysis

The effect of the COP value of the GSHP on the overall performance was analyzed, while the efficiency of the ORC unit and the capacity and characteristics of the

CHP and ABS units were kept fixed. Fig. 15 shows an

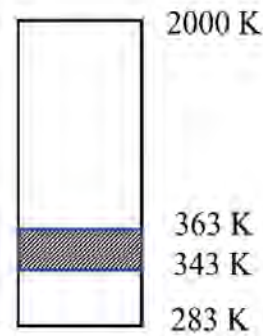


Figure 14. Exergy Flow Bar for District Heating with Central Natural Gas Boilers

unexpected result that COP increase does not help in increasing the $\bar{\psi}_R$ value. In this figure, COP =1 condition corresponds to 'no-GSHP' case, where the geothermal heat is directly used. This result agrees with the argument shown in Fig. 2. This result actually shows the

strength of the Model such that the optimum result is the no GSHP case, which could not be concluded from the First Law. One main reason for this result is the fact that current ORC technology has very low efficiency. Instead, low enthalpy geothermal resources may be supported by solar and wind energy. In this token, PVT systems indeed cover both CHP and heat pump technology. Therefore, before envisioning rather conventional technologies like ORC and classical heat pumps, one need to try solar and wind technology. This approach will indeed stay in heat pump technology without ORC units, unless their efficiencies are substantially improved.

This conclusion however is not universal and shows that every design, every load, and load distribution as a function of time during operation is important and the results are sensitive to these parameters too. For example, if the de-

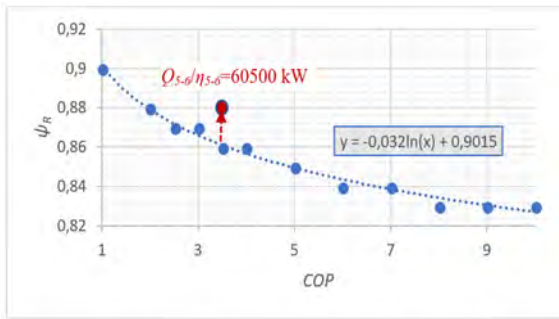


Figure 15. Sensitivity of $\bar{\psi}_R$ on the COP Changes. $Q_{5,6}/\eta_{5,6}=34500$ kW

sign value $Q_{5,6}/\eta_{5,6}$ is increased to 60000 kW (GSHP heat load) instead of 34500 kW, then $\bar{\psi}_R$ value at a COP value of 3.5 becomes 0.88 instead of 0.86 and the trend shown in Figure may also reverse. These results show that both the design, selection, and sizing of the systems and equipment are quite complex and a thorough analysis is essential on an hourly basis of the building loads besides developing and applying an exergy-based load allocation and control software.

CONCLUSION

All the above-mentioned case studies and sample calculations show that ORC, heat pump, district heating and similar energy conversion and distribution systems alone and only based on economic decisions may not be effective in reaching the CO₂ reduction targets of Paris Agreement. Avoidable CO₂ emissions, which are mainly a function of the rational exergy efficiency, namely the ψ_R term must be minimized first of all by maximizing the ψ_R term. Unfortunately, in all CO₂ mitigation strategies, only the First-Law rules are applied. In addition, hybrid system designs are quite handful, which has been shown here that they are a requirement in order to meet the CO₂

emission reduction goals. In order to optimize required hybrid system alternatives, new objectives need to be recognized and new evaluation metrics need to be defined based on exergy. COP term for example, needs to be modified in terms of exergy. COP_{EX} then shows that first of all heat pumps need to be re-designed for higher design COP values.

Using these new objectives and metrics, a careful circular hybridization may be made with rather engineering ease, which is only limited by imagination. In this quest heat pumps also play a major role in the advent of developing smart (or Rational) cities provided that their COP are high enough from exergy point of view. This requirement brings a necessary condition of combining low enthalpy energy resources like geothermal reservoirs and waste heat with low-exergy/low-energy buildings and district energy systems so that the temperature difference between the source and the demand is minimal. This leads to holistic design and analysis approaches like given in Fig. 10 [25].

In conclusion, it seems to be an absolute requirement that in low enthalpy resource utilization, we need to investigate the most rational way of utilizing low-exergy resources coupled with low-exergy demands like nZED and nZEXD (nearly-zero energy and exergy districts, respectively) for future settlements and retrofit districts [31]. In the same token, installation of nZEB and nZEXB (nearly-zero energy and exergy buildings, respectively) in order to improve the COP values of heat pumps. Last but not least, thermal energy storage systems (TES) are also very crucial for shaving off the peak loads, thus reducing the investment costs attributable to power, heat, and cold generation and improving the rational energy management efficiency [32].

NOMENCLATURE

A	Land area of a country, km ²
AV	Added Value,
a_o	Constant term in Equation 14, km
a, b, s'	Performance factors of the heat pump
A_v	Added value
CDH	Cooling Degree Hour, K·h
C	Power-to-heat ratio of CHP
$CBUC$	Capital unit Cost, TL/(kW _H /number of equivalent residences)
c_f	Unit CO ₂ content of the fuel, based on lower heating value, kg CO ₂ /kW·h
C_o	District capacity in terms of the number of equivalent residences without temperature peaking or equipment oversizing, number of residences, kW _H /number of residences
COP	Coefficient of Performance
COP_{EX}	Exergy-Based COP

C_R	Composite Rationality Index
E	Electric power, kW
E_X	Exergy, kW
E_{XD}	Total exergy delivered in the district for each dwelling, kW/dwelling
E_{xh} or E_{XH}	Thermal exergy, kW
E_{xg} or E_{XE}	Power exergy, kW
E_{XR}	Thermal exergy and power exergy output ratio of a geothermal system
GE	Geofluid Effectiveness, kW-h/kg
GSE	Geothermal System Effectiveness
HDH	Heating Degree Hour, K·h
i	Unit investment cost of the geothermal system, TL/(person·K·h)
I	Investment cost, TL
J	Thermal exergy of the geothermal well output per km ² of a country, kW/km ²
N	Population receiving district energy service (in the form of heat, cold, and power individually)
OF	Equipment Oversizing Ratio
P	Installed power capacity, kW
Q	Thermal (in the form of heat or cold) power, kW
R	CO ₂ Reduction Potential Ratio
RDR	Reservoir Decline Rate, kWh-h/h
s	Equipment performance constant (Equation 10)
T	Temperature, K
u	Unit CO ₂ emissions per kW of electrical power generated, E
u_x	Exergy-based unit CO ₂ emissions per kW of electrical power generated, E
X	Split ratio of the geothermal fluid heat between ORC and the heat pump

Greek Symbols

ϵ	Unit exergy, kW/kW
ψ_R	Rational Exergy Management Efficiency
η_I	First-Law Efficiency
ΔT	Temperature difference, K

Subscripts and Superscripts

a	Indoor air design temperature related variable
$boiler$	Boiler
C	Cooling, summer related
\mathcal{D}	District
DE	District energy system
dem	Demand
des	Destroyed

E	Electric
f	Fuel
H	Heat, heating, winter related
in	Inlet to the heat pump
I	First Law
K	Geothermal well head
KCR	Critical well-head temperature for equal power and heat exergy
L_{max}	Maximum allowable distance between the geothermal source and the district location, km
n	Power of the equipment thermal performance equation (Equation 10)
m	Power of Equation 14
in	Inlet to the heat pump
orc	ORC system
out	Outlet from the heat pump
o	Outdoor design condition
ref	Reference
sup	Supply
T	Transmission
TOT	Total
u, v	Summation limits in Equation 21.

Acronyms

ABS	Absorption system
CHP	Combined Heat and Power
DHC	District heating and cooling
DE	District energy system
4DE	Fourth-generation district energy system
GSHP	Ground-source heat pump
nZED	Nearly zero-energy district
nZEB	Nearly zero-energy building
nZEXD	Nearly zero-exergy district
nZEXB	Nearly zero-exergy building
ORC	Organic Rankine Cycle system
REMM	Rational Exergy Management Model
TES	Thermal energy storage
WSHP	Water-source heat pump

References

1. Baba. A. 2017. Hydro-Geochemical Properties of Geothermal Systems and its Effect on the System in Turkey, IGC 2017 Conference, Oral Presentation, 22-24 May, 2017.
2. ESMAP, 2016. Energy Sector Management Assistance Program, Greenhouse Gases from Geothermal Power Production, Technical Report 009/16, The World Bank Group, Washington DC, USA.
3. Niyazi A., Özge S., Halim M., and Gizem K. 2015. CO₂ Emission from Geothermal Power Plant in Turkey, Proceedings World Geothermal Congress 2015, Melbourne, Australia, 19-25 April 2015.
4. Aslan, H. 1996. Kömüre Dayalı Termik Elektrik Santrallerinde Verim ve Kapasite Kullanım Oranı Düşüklüğünün Nedenleri ve Bunların Yükseltimeleri İçin Alınması Gerekli Tedbirler, TMMOB 1. Enerji Sempozyumu, 12-14 Kasım 1996, Ankara.
5. Marta R.K., Olafur P.P., and Halldor P. 2010. Factors for Primary Energy Efficiency and CO₂ Emission of Geothermal Power Production, Proceedings World Geothermal Congress 2010, Bali, Indonesia, 25-29 April 2010.
6. Halldór Á. 20013. CO₂ Emission from Geothermal Plants, S12 Paper 103, pp: 56-62, International Geothermal Conference, Reykjavík, Sept. 2003.
7. Kılış, B. 2017. Jeotermal Enerjimiz, CO₂ Salımları ve Organik Rankin Çevrimli Santraller, Yeni Enerji, 61: 40-44.
8. Shengjun, Z., Huaixin, W. and Tao, G. 2011. Performance Comparison and Parametric Optimization of Subcritical Organic Rankine Cycle (ORC) and Transcritical Power Cycle System for Low- Temperature Geothermal Power Generation, Applied Energy, (88), 2011, 2740-2754.
9. Quoilin, S. and Lemort, V. 2009. Technological and Economical Survey of Organic Rankine Cycle Systems, 5th European Conference Economics and Management of Energy in Industry, 14-17 April 2009, Portugal: http://orbi.ulg.ac.be/bitstream/2268/14609/1/ECMEI_PaperULg_SQVL090916.pdf
10. Mathew A., Brian A. Chris U. 2011. Performance Analysis of the Chena Binary Geothermal Power Plant. Applied Thermal Engineering, Elsevier, 2011.
11. Kilkis B. and Kilkis, San, 2014. Energy and Exergy Based Comparison of Utilizing Waste Heat of a Cogeneration System for Comfort Cooling Using ORC Driven Chillers or Heat Pumps Versus Absorption/Adsorption Cycles, ASME ORC 2013, Conference Proceedings, 7-8 October, De Doelen, Rotterdam, the Netherlands.
12. EU, 2004/8/EC. 2008. Directive 2004/8/EC of The European Parliament and of The Council of 11 February 2004 on the Promotion of Cogeneration Based on a Useful Heat Demand in The Internal Energy Market and Amending Directive 92/42/EEC.
13. Kilkis, B., Kilkis, Ş. 2007. Comparison of Poly-generation Systems for Energy Savings, Exergetic Performance, and Harmful Emissions, Proceedings of ES2007, Energy Sustainability, Paper No: ES 2007-36262, June 27-30, Long Beach, California
14. TGE Research. 2017. Top 10 Geothermal Countries- 1 GW Installed Capacity Country Club.
15. Güven, Ö. 2015, Ankara'nın Jeotermal Potansiyeli ve Ankara'daki Jeotermal Projeleri, Jeotermal Kaynaklar Birliği Ekim Olağan Toplantısı, 2015, Haymana.
16. Kilkis, B., Kilkis, Siir, Kilkis, San. 2017. Optimum Hybridization of Wind Turbines, Heat Pumps, and Thermal Energy Storage Systems for Near Zero-Exergy Buildings (NZEXB) Using Rational Exergy Management Model, Paper No. 2, 12th IEA Heat Pump Conference, 15-18 May, Rotterdam 2017. Papers on line, <https://www.eiseverywhere.com/ehome/index.php?eventid=165152&tabid=558494> Also, abstracted in print, pp: 179-180.
17. EGEÇ. 2015. Developing Geothermal Heat Pumps in Smart Cities and Communities, EU REGEOCITIES, Project Publication, Brussels, June 2015, www.regeocities.eu
18. Kilkis, B. 2017. Analysis of Fourth-Generation District Energy Systems with Renewable Energy Cogeneration by Using Rational Exergy Management Model, World Sustainable Built Environment Conference 2017 WSBE17, Invited Paper, Paper no: 5693, 5-7 June 2017, Hong Kong.
19. Kilkis, B. 2016. Analysis of Fourth-Generation District Energy Systems with Renewable Energy Cogeneration by Using Rational Exergy Management Model, Paper No. 103, Proceedings, pp: 512-522, SBE 16 Smart Metropolises Conference, Istanbul, 13-15 October, 2016.
20. Rowshanzadeh, R. 2010. Performance and Cost Evaluation of Organic Rankine Cycle at Different Technologies, Master Thesis, Department of Energy Technology, KTH, Stockholm, Sweden.
21. Sun, W., Yue, X., and Wang. Y. 2017. Exergy efficiency analysis of ORC (Organic Rankine Cycle) and ORC-based combined cycles driven by low- temperature waste heat, Energy Conversion and Management, Vol. 135, 1 March 2017, Pages 63-73.
22. Marini, A., Alexandru, D., Grosu, L. and Gheorghian, A. 2014. Energy and Exergy Analysis of an Organic Rankine Cycle, U.P.B. Sci. Bull., Series D, Vol. 76, Issue 4, 2014 ISSN 1454-2358.
23. Kılış, B. ve Kılış, Ş. 2015. Yenilenebilir Enerji Kaynakları ile Birleşik Isı ve Güç Üretimi, (Combind Heat and Power With Renewable Energy Resources), TTMD Pub. No: 32, First Ed., ISBN: 978-975-6263-25-9, 371 pages, Doğa Pub. Co., İstanbul, 2015.
24. Kilkis, Ş. and Kilkis, B. 2017. A Simplified Exergy Methodology for Net-Zero Buildings Using Rational Exergy Management Model, Seminar 72 Low Energy Building Design Using Exergy Modeling, ASHRAE Winter Meeting, 27 January-1 February, Las Vegas.
25. Kılış, B., Kılış, Şiir, Kılış, Şan. 2017. Hydrogen Economy Based Net-Zero Exergy Cities of The Future with Water-Energy Nexus, The 12th Conference on Sustainable Development of Energy, Water, and Environment Systems-SDEWES Conference, 4-8 October 2017, Dubrovnik.
26. Kılış, B., Kılış, Ş. 2018. An Urban Planning Algorithm for Optimizing the Height of Buildings To Maximize the Share of PV Electricity Generation in a Nearly-Zero Exergy District, Proceedings of the 1st Latin American Conference on Sustainable Development of Energy, Water, and Environment Systems, LA. SDEWES 2018.0340, pp. 1-28.
27. Kilkis, B., Kilkis, Şiir, Kilkis, Şan. 2016. Next- Generation PVT System with PCM Layer and Heat Distributing Sheet, Solar TR2016 Conference and Exhibition, 6-9 December, 2016, Paper No: 0006, Proceedings, pp. 20-28, Istanbul.
28. Kilkis, B. 2016. Optimum Operation of Solar PVT Systems: An Exergetic Approach, Solar TR2016, Paper No: 0025, Proceedings, pp. 72-79, Istanbul Conference and Exhibition, 6-9 December, 2016.

29. Kilkis, I. B. 1996. Closed Loop Versus an Open Loop District System: A Techno-Economical Assessment, Geothermal Resources Council, Transactions, Vol. 20. pp: 95-102.
30. Kilkis I. B., Evaluation of the Proposed Geothermal District Energy System for the City of Aydin with New Rating Parameters, ASHRAE Transactions, Vol. 108, Part 2, pp.595-600, 2002.
31. Kilkis, B, Kilkis, Ş. 2017. New Exergy Metrics for Energy, Environment, and Economy Nexus and Optimum Design Model for Nearly-Zero Airport (nZEXAP) Systems, Energy Journal, 140 (2017) 1329-1349, Advanced Technologies in Aviation, Special Issue.
32. Kilkis, B. 2017. Exergetic Comparison of wind energy storage with ice making cycle versus mini-hydrogen economy cycle in off-grid district cooling, International Journal of Hydrogen Energy 42 (2017) 17571-17582.